elektronisches
dokument
ULB Sachsen-Anhalt

Martin Luther University (MLU)

Characterization of Control Mesoporous Glasses (CPGs) Using Positron Annihilation Lifetime Spectroscopy (PALS)

Dissertation

Submitted to the Faculty of Natural Sciences II
Martin Luther University Halle-Wittenberg

In Partial Fulfillment of the Requirements For the
award of the Degree of Doctor of Natural Sciences

(Physics)

BY

Essmat Mahmoud Hassan 'Sayed Ahmed'

MSc. in Physics (2001)

Born in: Suhag, Egypt 1974

Approvals:

1- Prof. Dr. R. Krause-Rehberg

2- Prof. Dr. Helmut Föll

3- Dr. habil Dirk Enke

Halle/Saale, 5 October 2007
Verteidigungsdatum: 30.01.2008

urn:nbn:de:gbv:3-000013180
[http://nbn-resolving.de/urn/resolver.pl?urn=nbn%3Ade%3Agbv%3A3-000013180]

Subject

Chapter 4: Experimental Details 50

Chapter 5: Results and Discussions. 62

Positron is the antiparticle of electron and in molecular materials such as polymers, porous glasses and zeolites, it may annihilate with an electron from its unbound or ‘free’ state, or may form a ‘hydrogen like’ bound state, with an electron from the material, called positronium (Ps). Ps may either self annihilate, or undergo further interactions with the material such as pick-off annihilation with an electron of the material. When Ps is localized at regions of low electron density such as holes in polymers or pores in porous glass, its lifetime changes in a way depending strongly on the size of the free volume. By measuring the resulting lifetime using γ-rays emitted from the annihilation of the Ps, the average size of the free volumes may be determined employing some calibration curves.

Positron techniques provide a non-destructive method to study open volumes, surface area and porosity inside molecular media. The techniques are also considered from the rare insitu tools which can probe the changes of the material properties in the time of measurements. Positron annihilation lifetime spectroscopy (PALS) may be uniquely capable of deducing a pore size, pore size distribution and the degree of filling of the pores in closed pore systems (not interconnected). In this particular case, the gas adsorption techniques are not applicable.

This thesis has two main goals. Firstly and for the first time, the positron annihilation lifetime technique is used to characterize the control porous glasses (CPGs) media. All the positron annihilation spectroscopy (PAS) investigations have been interested in the commercial Vycor glass (PVG) media of pores size $\leq$ 4 nm. Therefore, the PALS is used to establish basic correlations between the important physical properties of the CPG (pore size, surface area, and porosity) and the *o*-Ps lifetime. These correlations can be used as calibration curves in characterization of mesoporous glasses by the interested research groups. Hence, the PAL technique will be more precise and more time saving than the other tools such as gas adsorption-desorption and Hg mercury intrusion porosimetry. The second goal is to use these correlations to verify the validity of some suggested models and theories to discover possible deviations from the expected behaviour and to discuss the physical point of view for these deviations.

Chapter 1 presents an overview of positron, positronium and their interaction with solid materials. This chapter discusses various positron sources, the implantation and thermalization of positrons, positronium formation, modes of positron/positronium annihilation and the measurable quantities, and finally the different positron annihilation techniques, such as PALS and Doppler-Broadening spectroscopy (DBS).

Chapter 2 of this thesis is concerned with characterization of porous glass materials. This chapter discusses in detail the preparation methods of porous glasses specially control porous glass (CPG) and Vycor glass (PVG). The gas adsorption phenomenon in porous glass and the related definitions are discussed. Moreover, a provoking information has been given in the most frequently found types of gas physisorption isotherms according to the IUPAC system. The most important terms of the porous glass such as pore size, shape, volume, pore size distribution, surface area, and porosity are discussed. Finally, a brief overview has been given of the nitrogen gas adsorption-desorption and mercury intrusion tools as the most frequently used methods to determine the porous glass terms.

Chapter 3 presents in detail the well known models and the derived equations which correlate between the lifetime of the *o*-Ps long-lived component and the pore size, pore shape and the temperature dependence of the porous media. The equations to these models were simplified, moreover, results from these equations agree with findings from current literature.

Chapter 4 presents an overview of the main experimental techniques used in this thesis, namely positron annihilation lifetime spectroscopy (PALS). For this, the spectrometer equipments are discussed in details with the advantages and limitations. Moreover, I have already demonstrated the modifications and improvements which had been done to improve the vacuum pressure for two vacuum systems.

Chapter 5 explains the sample preparation for the measurements. The determination of the resolution function (FWHM) of the lifetime spectrometer and subtraction of the source background have been shown from the analysis of Si reference spectra by using the LT analysis program. The chapter represents also the experimental data for the correlation between the *o*-Ps lifetime and pore sizes for a system of CPG media (from 1 nm to 64 nm) as I compare this experimental data with two of the most recommended models for our mesoporous glass system; They are named the rectangular Tao-Eldrup model (RTE-model) extended TE-model (ETE-model). Moreover, the theoretical calculations for the correlation between the *o*-Ps lifetime and pore sizes (from 1 nm to 100 nm) for different pore geometries and overlapping parameter values ΔR (0.18 nm, 0.19 nm and 0.20 nm) have been estimated by using the new routine EELViS developed recently by R. Zaleski from the University of Lublin. The routine is based on the extended TE-model (ETE-model). I also studied the temperature dependence of the *o*-Ps long-lived component in different pore sizes to verify the validity of the ETE-model. In this study I present for the first time the experimental results of the behavior of the *o*-Ps lifetime in pore sizes larger than 10 nm and I give our suggested explanations to their deviation from the ETE model. For the first time, the PALS is deeply used to check the capillary condensation effect in CPG media. Finally, the experimental correlation between the *o*-Ps intensity from one side and the surface area and porosity from the other side are discussed. Conclusions are summarised in a single section at the end of the thesis.

1.1. Introduction

The phenomenon of positron annihilation spectroscopy (PAS) has been utilized as nuclear method to probe a variety of material properties as well as to research problems in solid state physics. The field of solid state investigation with positrons started in the early fifties, when it was recognized that information could be obtained about the properties of solids by studying the annihilation of a positron and an electron as given by Dumond et al. [1] and Bendetti and Roichings [2]. In particular, the discovery of the interaction of positrons with defects in crystal solids by Mckenize et al. [3] has given a strong impetus to a further elaboration of the PAS. Currently, PAS is amongst the best nuclear methods, and its most recent developments are documented in the proceedings of the latest positron annihilation conferences [4-8].

PAS is successfully applied for the investigation of electron characteristics and defect structures present in materials, magnetic structures of solids, plastic deformation at low and high temperature, and phase transformations in alloys, semiconductors, polymers, porous material, etc. Its applications extend from advanced problems of solid state physics and materials science to industrial use. It is also widely used in chemistry, biology, and medicine (e.g. locating tumors). As the process of measurement does not mostly influence the properties of the investigated sample, PAS is a non-destructive testing approach that allows the subsequent study of a sample by other methods. As experimental equipment for many applications, PAS is commercially produced and is relatively cheap, thus, increasingly more research laboratories are using PAS for basic research, diagnostics of machine parts working in hard conditions, and for characterization of high-tech materials.

1.1.2. Positron and Positronium Physics

All subatomic particles have antiparticles, which are often referred to as antimatter. The antiparticle of the normal-matter electron is called the positron. Positron has the same mass (m_o) and spin (1/2) as an electron, but with the opposite charge. As predicted by Dirac in 1928 [9], positron was the first antiparticle in physics. The first experimental evidence of the positron existence was verified by Anderson [10] in his studies of cosmic radiation and termed "positive electron."

When a positron and an electron interact through a head-on collision, they annihilate, converting all of their mass into energy (as per Einstein's equation $E = m_oc^2$). The total amount of energy released when a positron and an electron annihilate is 1.022 MeV, corresponding to the combined rest mass energies of the positron and electron. The energy is released in the form of photons. The number of photons depends on exactly how the positron and electron annihilate. Positrons usually have a very short life in a material for the following reasons:

(1) They can either freely annihilate with electrons directly, like a head-on collision in the medium, resulting in the annihilation process. Two photons are then emitted with an energy of 0.511 MeV, or,

(2) In some materials, they form a stable state with an electron which is similar to the hydrogen atom with a binding energy ~ 6.8 eV. This is termed positronium (Ps) which also annihilates.

Ps is generally not found in metals, but is found in molecular materials, metals oxides, molecular liquids and gasses and its annihilation parameters reflects the properties of the containing host medium.

1.1.3. Annihilation Process

The mass transformation into photons, if the particles have low energy, is called the annihilation process. In most cases, two γ-quanta arise according to the equations

$$e^{+} + e^{-} \rightarrow \gamma - quanta \qquad (2.1)$$

$$E_{2\gamma} = 2\, m_o c^2 + E_{e^+} + E_{e^-} \qquad (2.2)$$

$$m_o c^2 = 0.511 \text{ MeV} \qquad (2.3)$$

where $E_{2\gamma}$, E_{e+} and E_{e-} are the energies of the resulting γ-ray pair and of electron and positron, respectively, m_o is the rest mass of the electron (and also of the positron) and c is the velocity of light. The annihilation process follows certain general laws of conservation, such as the conservation of total energy, total angular momentum, total linear momentum, and parity. Hence, the study of the radiation produced by the annihilation of a positron with an electron is important for understanding the fundamental properties of the positron and for investigating the properties of the local environment of the annihilation site.

Annihilation may occur between free positrons and electrons or between particles in a bound state (Ps);

(I) Free positron annihilation; in this type of decay (Fig.1.1), a positron after thermalization, annihilates with an electron in the medium either through a singlet collision (spins antiparallel (s=0)) or through a triplet collision (spins parallel (s=1)). Selection rules governing the annihilation show that a singlet collision results in emission of two photons (2γ-ray) in exactly opposite direction according to the center of mass system, each are having an energy of about 0.511 MeV (= m_oc^2) [11]. On the other hand a triplet collision gives rise to annihilation into 3γ-rays. In this case the rest energy (= $2m_oc^2$) of the electron-positron pair is shared between the three photons which are emitted in one plane and in various directions relative to each other. The energy of the γ-rays can vary from zero to m_oc^2. In this type of decay, the annihilation cross section (probability) of the emission of 3γ-rays is reduced approximately by the fine structure factor α (α=1/137) of the cross section. Although very rare from a theoretical point of view, the non-photon and one-photon annihilation are also possible but only if a third body is close enough to absorb the recoil momentum such as an electron or nuclei.

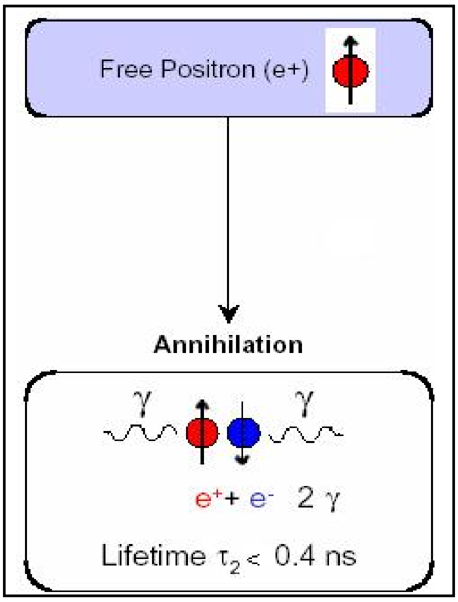

Fig. 1.1. Schematic representation of the free annihilation process.

The rate of free annihilations by the two photon process from the singlet state (^1S), depends on σ_s and the positron electron overlap in this state this leads to the expression;

$$\lambda = \sigma v n_e = r_o^2 c n_e \qquad (1.4)$$

It is independent of the positron velocity v and simply proportional to the density of electrons n_e. Thus the probability of the two photon annihilation is considerably larger than that for one or three photons. The ratio of the cross-sections for the respective process being

$$\sigma(3)/\sigma(2) \approx \alpha \qquad \sigma(1)/\sigma(2) \approx \alpha^4 \qquad (1.5)$$

The annihilation cross-section was calculated by Dirac in 1930. Using his result in the non-relativistic limit, one finds that for low positron energies, the cross-section for the two photon annihilation is inversely proportional to the positron velocity v and electron at rest is

$$\sigma(2) = \pi r_o^2 c/v \qquad v \ll c \qquad (1.6)$$

where r_o= the classical electron radius, c= the velocity of the light, and v = the velocity of the positron

(II) Positronium formation; in this type of decay (see Fig. 1.2), as previously referred, when positron is slowed down in a medium to energies < 10 eV, it can form Ps. This was theoretically predicted in 1934 by Mohorovicic [12] using classical mechanics, also in 1945 by Ruark [13] with a quantum approach, and experimentally detected in 1951 by Deutsch [14]. The *p*-Ps state decays through 2γ with a lifetime of about 125 ps in vacuum. While the *o*-Ps state lives much longer (~142 ns in vacuum) because its self annihilation (intrinsic annihilation) it is through 3γ-photons by which all have energies less than 0.511 MeV. The ratio probabilities of 3γ and 2γ process for normal positron annihilation are 1/137 [15].

The lifetime of the *o*-Ps state may be substantially reduced if the Ps formed in the vicinity of atoms. This reduction may be due to the so called "pick-off" process in which the positron of the *o*-Ps annihilates with an electron from the material with opposite spin and then annihilates via 2γ decay, or as a result of a transition from *o*- to *p*-Ps, a "quenching process," which then quickly annihilates.

The lifetime of Ps in materials with large open volume, such as polymers, is in the order of 1-2 ns or more. The relative amount of *p*-Ps: *o*-Ps states are 1:3 in the absence of external electric and magnetic fields.

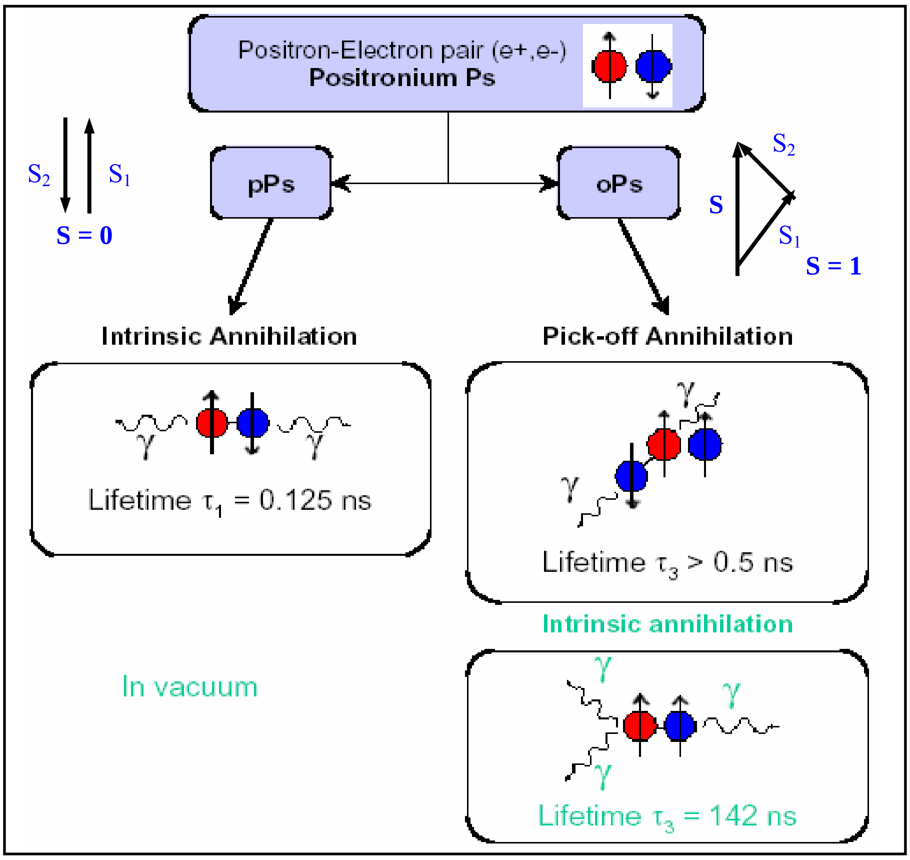

Fig. 1.2. Schematic representation of different types of the Ps annihilation processes. In this process, the spin angular momenta S_1 and S_2 for the electron and positron can combine to form the total angular momentum $S=S_1+S_2$ that correspond to S=0 (a singlet state) and S=1 (a triplet state).

1.2. Possible Sources of Positron

There are several possible ways in which positrons can be produced. One of these ways is through the beta (β^+)-decay of radioactive isotopes. A large majority of investigations on solids by positrons have been done with ^{22}Na, ^{58}Co and ^{86}Sr positron sources, mainly because of their low production costs, simplicity of their manufacture in laboratory and relatively convenient half-life.

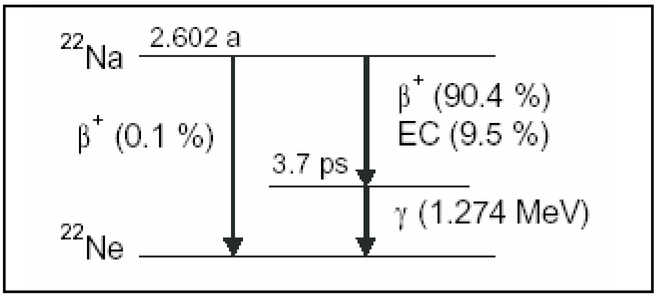

Fig. 1.3. Schematic illustration of the decay of the radioactive source ^{22}Na by emission of a positron and neutrino to the excited state of ^{22}Ne.

In our experiments, the radioactive isotope ^{22}Na is used as a positron source. ^{22}Na has a number of main advantages. It emits a prompt 1.274 MeV γ-ray simultaneously with the positron birth, which allows the positron lifetime to be recorded by a coincidence γ-spectrometer. Moreover, it has a relatively long half-life of 2.61 years, and it is available in a dilute ^{22}NaCl solution, which is easy to handle and chemically stable.

Positrons emitted by nuclear radioactive sources have an energy distribution range from 0 to a few 100 keV. The radioactive source ^{22}Na decays according to the following reaction:

$$^{22}\mathrm{Na} \rightarrow {}^{22}\mathrm{Ne} + \beta^+ + \nu_e + \gamma,$$

where ^{22}Na isotope gives a relatively high positron yield of 90.4%, The decay scheme of ^{22}Na is shown in Fig. 1.3. It is observed that ^{22}Na decays by positron emission and electron capture (E. C.) to the first excited state of neon nucleus (^{22}Ne) by the emission of an energetic positron and an electron neutrino. This excited state quickly de-excites to the ground state by the emission of a 1.274 MeV γ-ray with half-life $T_{1/2}$ of 3 ps. 10 % of the time ^{22}Na will decay by electron capture.^{22}Na may also decay (0.05 %) directly to the ground state of Ne via the emission of a more energetic positron. Thus positron emission is almost simultaneous with the emission of the 1.274 MeV γ-ray while the positron annihilation is accompanied by two 0.511 MeV γ-rays

The positrons generated in the γ-decay reaction mentioned above (in case of ^{22}Na) exhibit a broad energy distribution up to energy of 0.540 MeV and can penetrate deep into a sample. In order to obtain depth profiling information, studying thin layers for example, monoenergetic "slow" positron beams are required. The "fast" positrons can be slowed down using a moderation step. Positrons can be expelled from a surface that possesses a negative work function [16]. The positrons rejected from the metallic moderator surface have a very narrow energy distribution of the order of a few eV. After moderation, the positrons are transported and accelerated to the desired implantation energy. Using PAS together with positron beams to study matter is referred in literature as Positron Beam Analysis [17].

Another possible source of positrons is a process called pair-production. This occurs when high-energy γ-rays spontaneously create a positron and an electron.

1.3. Positron States in Matter

A study of the behavior of positrons in condensed matter guides us to those situations in which the characteristics of the annihilation process are likely to provide useful information regarding electronic and other properties of the system. The behavior of the positron, prior to annihilation is strongly reflected in the form of the characteristic lifetime spectra [18]. For the purpose of the present discussion, it is suitable to classify the materials of interest according to the following scheme:

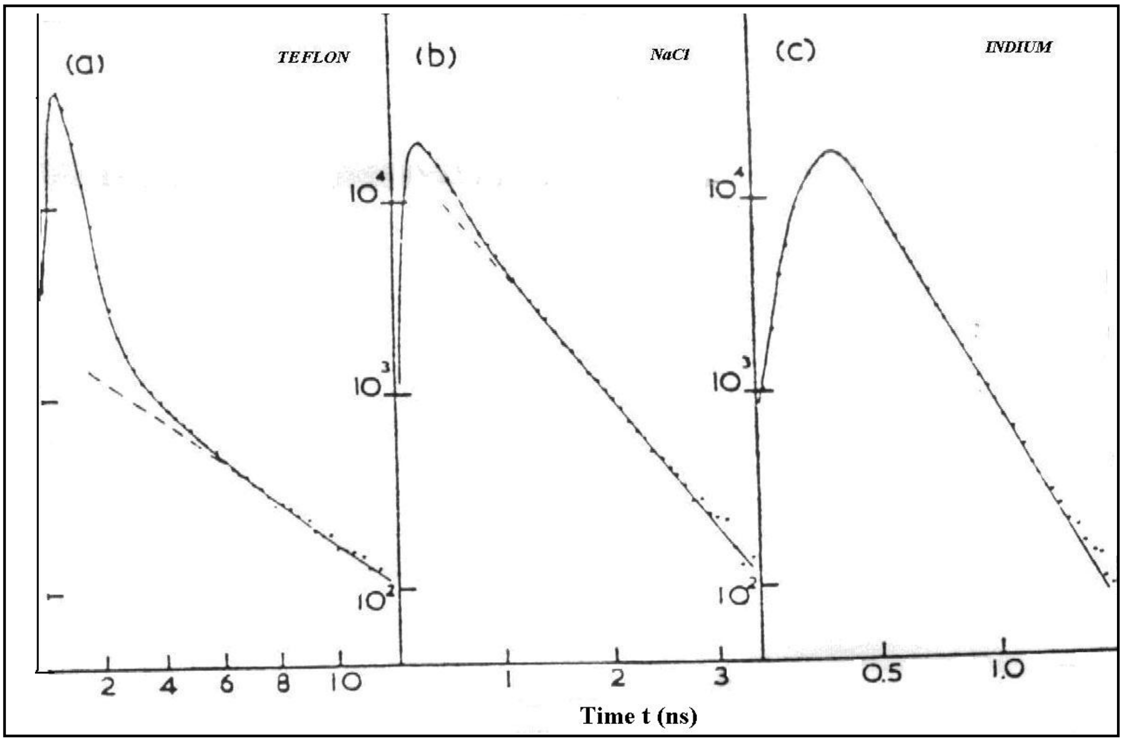

Fig. 1.4. The three types of spectra according to classify the materials of interest. (a) Molecular materials, (b) Ionic crystals, (c) Metals.

In Fig.1.4 condensed gases, organic solids and glassy or amorphous insulators are included. These materials usually exhibit lifetime spectra that can be resolved into two or three components, lifetimes ranging from 0.1 to 10 ns. Ionic crystals such as metals halides, hydrides and oxides also show several components. Here the individual spectra are very similar and are only resolved with difficulty by the lifetime, Doppler broadening, or Angular correlation techniques. The lifetimes of defect- free metals are normally characterized by a single component and lie in the range 100-300 ps [19]. The occurrence of multi-component spectra in types (a) and (b) materials suggests that the positron can annihilate from a variety of distinct states. However, the three lifetime components that are generally observed in the spectra of condensed gases may be tentatively attributed to *p*-Ps decay, annihilation of free positrons in the bulk and pick-off annihilation of *o*-Ps in voids inside the gas.

An early calculation done by Lee-Whiting [20] demonstrates that the time required for a positron in a metal to reach thermal energies KT (≈ 0.027eV) was estimated to be approximately 3 ps. We may thus conclude that most of the positrons in metals cannot annihilate when they have high energies. They must be thermalized before annihilation. On the other hand, in insulators, where energy loss to electrons is inhibited by broad energy gaps, the final stages of thermalization can only proceed by excitation of lattice vibrations. De Benedetti et al. [21] deduced the thermalization time of the order 300 ps for this process. It follows that the thermalization of free positrons may not be completed before annihilation in some materials. The final stages of the slowing down process may be further complicated by the formation of a Positronium atom, which decelerates slower than a free positron by virtue of comparatively weaker interactions with the surrounding medium.

1.4. Kinetics of Ps Formation and Lifetime Spectrum

Several authors published Ps formation and trapping models including various reaction between positrons, electrons and various kinds of traps (polar groups, radiation induced traps, various types of free volume holes) [22, 23]. These models explain the features of the lifetime spectrum.

Let us assume that at time $t = 0$ all positrons are thermalized in the bulk of a sample and have not yet formed Ps. This corresponds to the boundary conditions $n_{\mathrm{p}}(t = 0) = 1$ and $n_{\mathrm{pPs}}(t = 0) = n_{\mathrm{oPs}}(t = 0) = 0$. Further, as the most simple case, we assume that the free positrons disappear from the bulk by annihilation with a rate λ_{p} and by formation of Ps with the rate κ_{Ps}. If there are several ways of Ps formation (for example, with free electrons and with electrons trapped at shallow centres) κ_{Ps} must be replaced by the sum of these rates. The formed *p*-Ps and *o*-Ps annihilate with the rates λ_{pPs} and λ_{oPs}. The changes of the relative number of annihilating particles in time are then given by

$$\begin{aligned} &dn_p/dt = -(\lambda_p + \kappa_{Ps})\, n_p && n_p(0) = 1 \\ &dn_{pPs}/dt = (1/4)\, \kappa_{Ps} n_p - \lambda_{pPs} n_{pPs} && n_{pPs}(0) = 0 \qquad (1.7) \\ &dn_{oPs}/dt = (3/4)\, \kappa_{Ps} n_p - \lambda_{oPs} n_{oPs} && n_{oPs}(0) = 0 \end{aligned}$$

The equations include that ¼ of Ps is formed as *p*-Ps and ¾ as *o*-Ps. This system of equations is solved with the general expression $n_i = C_i \exp(-\lambda_i t)$ where the constants C_i are determined from the initial conditions for the $n_i(t = 0)$. The solution of this system of differential equations with constant coefficients gives

$$n_p(t) = \exp\left[-(\lambda_p + \kappa_{Ps})\, t\right] \qquad (1.8)$$

$$n_{pPs} = (\tfrac{1}{4}) \left[\kappa_{Ps} \big/ \left(\kappa_{Ps} + \lambda_p - \lambda_{pPs}\right)\right]\left[\exp(-\lambda_{pPs} t) - \exp(-(\lambda_p + \kappa_{Ps})\, t)\right] \qquad (1.9)$$

$$n_{oPs} = (\tfrac{1}{4}) \left[\kappa_{Ps} \big/ \left(\kappa_{Ps} + \lambda_p - \lambda_{oPs}\right)\right]\left[\exp(-\lambda_{oPs} t) - \exp(-(\lambda_p + \kappa_{Ps})\, t)\right] \qquad (1.10)$$

The lifetime spectrum shows the number of annihilations d*n*(*t*) in the channel of the time analyser with the width d*t* a the time *t*,

$$s(t) = -dn(t)/dt = \lambda_p n_p(t) + \lambda_{pPs} n_{pPs}(t) + \lambda_{oPs} n_{oPs}(t) \qquad (1.11)$$

In a lifetime analysis, the spectrum is decomposed with respect to the different lifetimes. It means that three exponential components will appear obtained by rearranging Esq. (1.8)-(1.10) with respect to increasing time constants,

$$s(t) = \Sigma\, (I_i/\tau_i)\exp(-t/\tau_i)$$

$$\tau_1 = 1/\lambda_{pPs} = \tau_{pPs} \qquad (1.12)$$

$$\tau_2 = (\kappa_{Ps} + \lambda_p)^{-1} < \tau_p = 1/\lambda_p \qquad (1.13)$$

$$\tau_3 = 1/\lambda_{oPs} = \tau_{pPs} \qquad (1.14)$$

with the intensities

$$I_1 = (1/4)[\kappa_{Ps}/(\kappa_{Ps} + \lambda_p - \lambda_{pPs})] \qquad (1.15)$$

$$I_2 = 1 - (I_1 + I_3) \qquad (1.16)$$

$$I_3 = (3/4)[\kappa_{Ps}/(\kappa_{Ps} + \lambda_p - \lambda_{oPs}] \qquad (1.17)$$

A finite Ps formation rate κ_{Ps} leads to a delay in the build up of the Ps intensity which is described in Eqs. (1.9) and (1.10) by the term $[-\exp(-(\kappa_{Ps} + \lambda_p)t)]$. Due to the rearrangement of the spectrum components in the lifetime analysis, however, this has no effect on the analysed Ps lifetimes and the values τ_{pPs} and τ_{oPs} are directly measured. Only, $\tau_2 = (\kappa_{Ps} + \lambda_p)^{-1}$ will be shorter than $\tau_p = 1/\lambda_p$. A finite Ps formation rate effects the component intensities I_i which now deviate from the theoretical *p*-Ps and *o*-Ps yield of $I_1/I_3 = 1/3$ by

$$I_1/I_3 = (1/3)(\kappa_{Ps} + \lambda_p - \lambda_{oPs})/(\kappa_{Ps} + \lambda_p - \lambda_{pPs}). \tag{1.18}$$

Moreover, the intensities may have negative values which, however, seems to be never observed. This may suggest that the Ps formation rate κ_{Ps} is rather large in comparison with $(\lambda_{pPs} - \lambda_p)$. Then, the intensity ratio of lifetime components amounts to $I_1/I_3 \approx 1/3$ and $I_2 \approx 0$. This corresponds to an instantaneous formation of Ps. We remark, however, that a disappearing value of I_2 was even never observed. Always when Ps is formed three components were observe to appear in the lifetime spectrum.

This apparent problem can be solved within the blob model of Ps formation developed recently by Stepanov et al. [24-26]. This model is an extension of the traditional spur model [27, 28]. The essential elements of the positron blob model which are illustrated in Fig. 1.5 are the following: a positron of several hundred keV will lose most of its energy within 10^{-11} s through ionizing collisions (the spur, cylindrical column in Fig. 1.5) until its energy drops below the ionization threshold. In the final ionizing regime, with the positron energy between 0.5 keV and the ionization threshold of several eV, $n_0 \approx 30$ electron-ion pairs are generated within a spherical volume of radius $a_{bl} \approx 40$ Å called the blob. The subionizing positron further undergoes positron-phonon scattering and may diffuse out of the blob, until it becomes thermalized in a spherical volume bigger than the blob volume, $a_p > a_{bl}$.

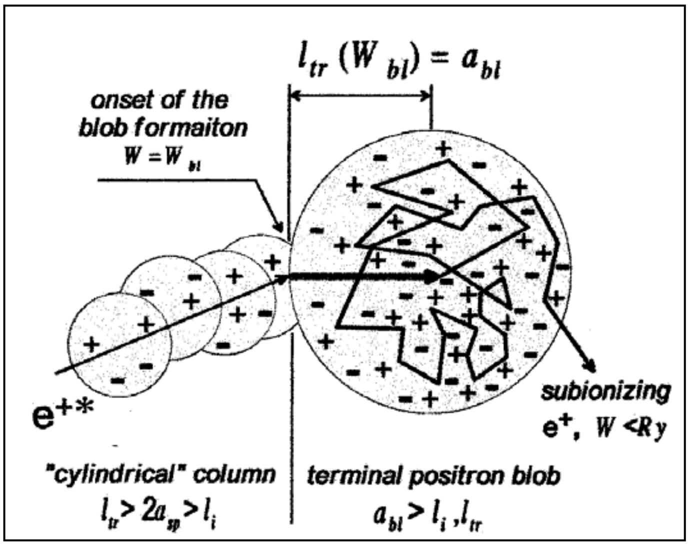

Fig.1.5. Schematic view on the terminal positron blob. Positron motion is simulated as random walks with the energy dependent step $l_{tr}(W)$. For more details see Stepanov et al. [24].

The intrablob electrons are tightly kept by electric fields of the positive ions. Also the positrons thermalized within blob can not escape from the blob, but the faster, subionizing positrons can do so. Thus it is necessary to distinguish between the inside (e^{+}_{in}) and outside (e^{+}_{out}) blob positrons.

Within the blob, the first stage of Ps formation is the encounter of a thermalized positron with one of the thermalized intrablob electrons, followed by formation of weakly bund $e^{+}\cdots e^{-}$ pair. The pair is transformed to quasi-free Ps in the bottom of the lower-energy band, and finally localized at one of the numerous local free volumes. The driving force for localization is the repulsive exchange interaction (due to the Pauli principle) between the electron constituting the Ps atom and electrons of surrounding molecules. Schematically, the consecutive stages of Ps formation may be displayed as follows:

$$e^{+}_{qf} + e^{-}_{blob} \rightarrow (e^{+} \cdots e^{-}) \rightarrow \text{qf-Ps} \rightarrow \text{Ps in the hole or pore} \qquad (1.19)$$

Here, qf denotes the quasi-free states of e^{+} and Ps and $(e^{+} \cdots e^{-})$ a loosely bound e^{+} - e^{-} state as Ps precursor. The process of Ps formation competes with the ion-electron recombination which decreases the number of free electrons available for Ps formation.

One may assume that all intrablob positrons (e^{+}_{in}) form instantaneously Ps in its final state (localized at a pore). The outside blob positrons (e^{+}_{out}) follow their own relation and do not take part in any reaction but annihilate with their characteristic lifetime τ_p. This general assumption seems not unreasonable since there are many free electrons inside the blob available for Ps formation but usually there are no free electrons outside. Under these assumptions the lifetime spectrum will have the lifetimes

$$\tau_1 = \tau_{pPs} \qquad (1.20)$$
$$\tau_2 = \tau_p \qquad (1.21)$$
$$\tau_3 = \tau_{pPs} \qquad (1.22)$$

and the relative intensities

$$I_1 = P/4 \qquad (1.23)$$
$$I_2 = 1 - (I_1 + I_3) \qquad (1.24)$$
$$I_3 = 3P/4 \qquad (1.25)$$

where P is the probability of Ps formation (the Ps yield). Trapped electron and positron states will of course complicate this simple but general picture. But, usually, these processes effect the value of τ_2 and the intensities, but not $\tau_1 = \tau_{pPs}$ and $\tau_3 = \tau_{pPs}$.

Ps may undergo various transformation and annihilation channels such as self-annihilation, pick-off annihilation with an electron other than its own bound partner, chemical quenching by electron acceptors, or spin conversion at unpaired electrons (see a later chapter).

In case that Ps decays via self-annihilation and the pick-off process (see Fig. 1.2) the lifetimes of the first and third components are

$$\tau_1 = \tau_{pPs} = (\eta / \tau_{pPs}{}^0 + \lambda_{po})^{-1},\ \tau_{pPs}{}^0 = 125\text{ ps} \qquad (1.26)$$

$$\tau_3 = \tau_{oPs} = (\eta / \tau_{oPs}{}^0 + \lambda_{po})^{-1},\ \tau_{pPs}{}^0 = 142\text{ ns} \qquad (1.27)$$

where λ_{po} is the pick-off annihilation rate (see chapter 3). $\tau_{pPs}{}^0$ and $\tau_{oPs}{}^0$ are the mean lifetimes of p-Ps and o-Ps which decay via self-annihilation in a vacuum. η is the so-called contact density or relaxation parameter which describes the relaxation of Ps in matter compared with the state in vacuum. The diameter of the Ps atom is $0.106\eta^{-1/3}$ nm [27].

1.5. Principles of Positrons Annihilations in Solid

PAS is a nuclear method that has become nowadays one of the basic tools for the study of the electronic and defect structures of condensed matter [29]. When energetic positrons are injected into a solid from an isotope such as ^{22}Na, they rapidly lose almost all their energy by a succession of ionizing collision with electrons and ions of the medium, they are slowed down to thermal energies (~ 0.27 eV).

During this energy loss process, the positron travels a distance into the solid which is larger the higher its initial energy. Because of multiple scattering events the positron paths are quite tortuous and the ultimate point of thermalization may locate between the surface and a depth defined by the maximum range. At a time δt that is distributed from zero up to some hundreds of picoseconds, the positron will annihilate with an electron yielding.

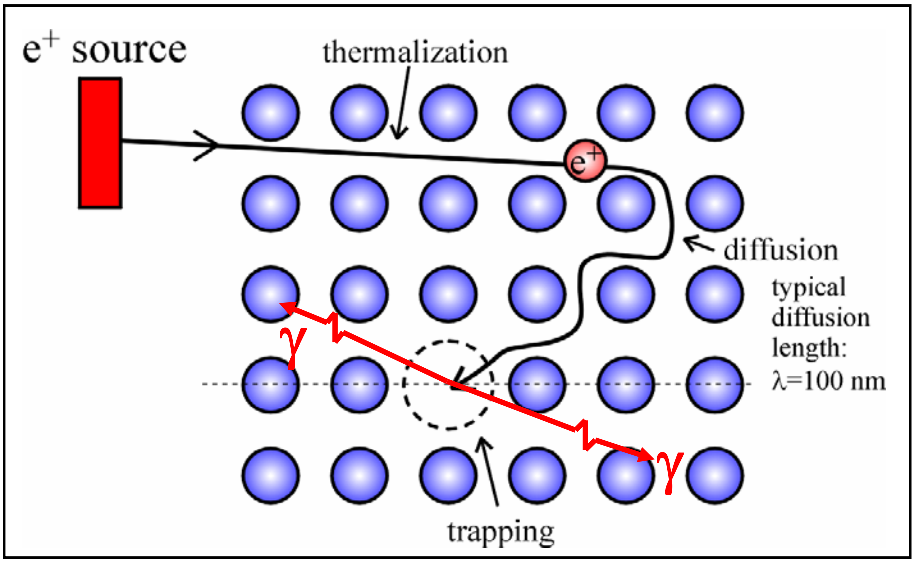

Fig. 1.6. Schematic diagram shows a single positron penetrating through matter undergo various processes influencing the state from which the positron annihilates with an environmental electron.

The total rest mass energy of the annihilated pair, $2mc^2 = 1.022$ MeV appears almost as two γ-rays each of energy of 0.511 MeV in opposite directions. These γ-rays contain the information measured by the different PAS techniques. They give the positron lifetime τ (the birth of the positron can be detected by the 1.274 MeV γ-ray emitted by the radioisotope during its decay), which provides information about the electron densities at the site of the positron. The time it takes for the positron to meet an electron and subsequently annihilates depend on the electron density in the material. In addition, these γ-rays carry also information about the momentum of the annihilating electron-positron pair. The positron lifetime and the momentum density depend on the site where the annihilation takes place. A measurement of the photon's angular and energy distribution reveals information concerning the electron momentum densities.

The trapping of the positron in the open-volume defects sites with sizes in the sub-nanometer range defects is based on the formation of an attractive potential at these sites, such as vacancies, vacancy agglomerates, and dislocations. The main reason for this potential is the lack of repulsive positively charged nucleus in such a defect. PAS sensitivity for the vacancy detection starts at $10^{-7}at^{-1}$. This enormous sensitivity is caused by the fact that the positron diffuses about 100 nm through the lattice and probes a high number of atoms until its annihilation.

When the positron is trapped in an open-volume defect, its lifetime increases from that of a delocalized positron due to the reduced electron density. This causes also the peaking of the momentum density to lower values. The annihilation γ-rays from positrons trapped at such sites have a significant different characteristics from those resulting from annihilations in the perfect lattice. These changes in the positron annihilation characteristics make the PAS powerful to study the electronic and ionic structures and the associated processes of defects in solids.

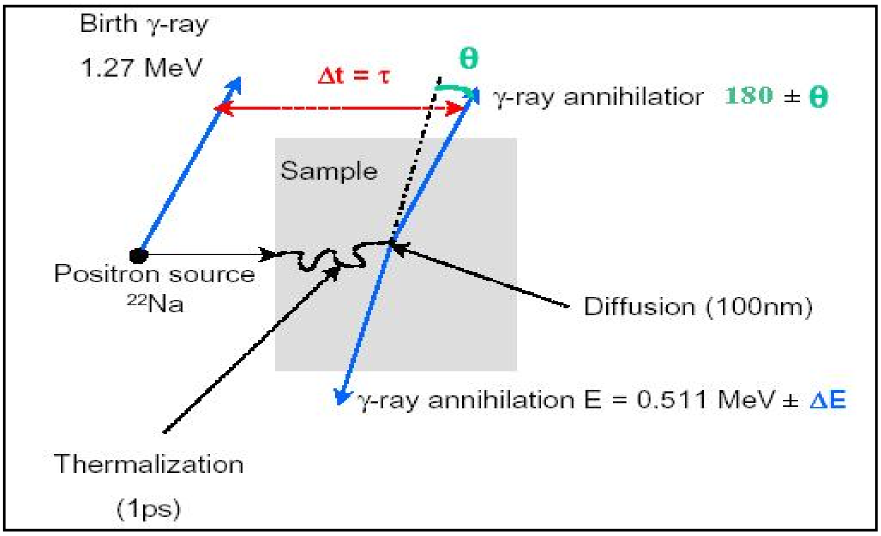

Fig. 1.7. Schematic Diagram for the three PAS experimental techniques.

Figure 1.7 shows a schematic diagram of PAS, which are used with the annihilation radiation: (a) Lifetime technique (measurement the delay time τ between the emission of the positron and annihilation photons), (b) Doppler broadening technique (measurement of the shift in the energy ΔE between the annihilation photon and the energy m_oc^2 the injected and annihilated positron as we will see in the next section), and (c) Angular correlation technique (measurement of angular distribution of the 2 annihilation photons $(180 \pm \Delta\theta)$.

Because energy and momentum are conserved in the annihilation process, the 2γ-rays resulting from the usual electron-positron pair annihilation each have energy equal to the rest-mass energy of an electron or positron (m_oc^2= 511KeV) ± ΔE. The two γ-rays propagate in opposite directions ± $\Delta\theta$ as shown in Fig.1.6. The deviations ΔE and θ arise from the net momentum of the annihilating positron-electron pair. However, since the positron is thermalized the value of ΔE and θ corresponds mainly to the momenta of the annihilating electrons. In the next section I will discuss the Doppler broadening spectroscopy more in details.

Although the positron lifetimes and source intensities are such that no more than one positron usually exists in the sample at a given instant, the PAS techniques integrate over a large number (often~10^6) of annihilation events. The distribution of the δt values for a number of these events measured in PALS experiments yields information regarding the total electron density $\rho^-(r)$ in the region of positron electron annihilation. This is because the rate λ, equals to the reciprocal positron lifetime τ, is given by the overlap integral of the electron and positron densities ρ^- and ρ^+ as

$$\lambda = \pi\, r_o^2\, c \iiint \rho^-(r)\, \rho^+(r)\, d^3r \qquad (1.28)$$

r_o = the classical electron radius, and c = the velocity of light, and $\rho^+(r)$ = the positron density in the material.

1.6. Positron Annihilation Lifetime Spectroscopy

One type of PAS that is a very sensitive probe of defect density and size, is the positron annihilation lifetime technique. PALS measures the time of the positron in the material. In this technique, the lifetimes of a large number of positrons are recorded by detecting the birth of the positron via the 1.274 MeV photon and subsequently detecting the radiation emitted by annihilation. Positrons annihilate from different lattice sites (bulk of sample, located at defects) each of which gives a characteristic lifetime $\tau_i = 1/\lambda_i$. The positron lifetime spectrum is thus the sum of exponential decay components

$$\frac{d\ n\ (t)}{dt} = \sum_i \frac{I_i}{\tau_i}\ \lambda_i\ e^{-\lambda\, t} \qquad (1.29)$$

where the relative intensities I_i, satisfy the summation $\sum I_i = 1$ and n(t) is the probability that a positron is still alive at time t after its emission. Experimentally, the lifetime of the positron is the time delay between the positron emission and annihilation. The lifetime of the positron is decreased as the electron density is increased. As annihilation is a statistical process, many annihilation events have to be measured and arranged in a histogram in order to determine the positron lifetime in the sample. Figure 1.8 shows a positron lifetime spectrum of copper at room temperature (RT). It can be described by an exponential decay function. By fitting this function to the spectrum, the positron lifetime in copper may be determined. Figure 1.8 shows a positron lifetime spectrum of copper at 300 K. It can be described by an exponential decay function. By fitting this function to the spectrum, the positron lifetime in copper may be determined.

The lifetime spectrometer consists of a start and stop detector made by coupling a fast scintillator to a photomultiplier tube (PMT). The timing pulse is obtained by a constant-fraction discriminator (CFD).

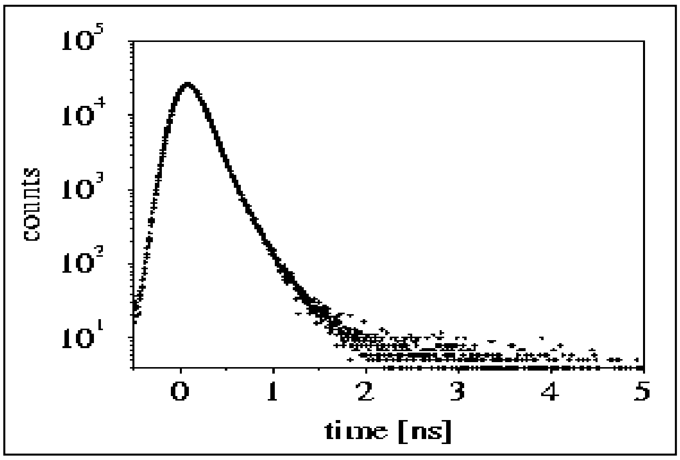

Fig. 1.8. The positron lifetime spectrum of Cu at room temperature.

Due to the finite time resolution, annihilation within the source materials, and random background, there are only 2-3 decades of the exponential part of Eq.(1.29) in an experimental lifetime spectrum. Thus typically only two lifetime components can be used to analyze the spectra in metals or semiconductors.

The average lifetime is given as follows:

$$\tau_{av} = \int dt \left(\frac{d \quad n(t)}{dt} \right) = \sum_i I_i \quad \tau_i \qquad (1.9)$$

It is a good and stable statistically parameter, because it is the centre of mass of the lifetime spectrum. Changes below 1 ps can be reliably observed. Further, the positron long lifetime component in a material is the direct manifestation of positron trapping in defects.

Figure 1.9 represents the number of positron decays as a function of time after entry into a defected material. The figure reveals two distinct decay constants, corresponding to two lifetimes: (a) a short lifetime for positrons that annihilate in the bulk (reduced bulk lifetime), and (b) a longer lifetime for positrons trapped in defects.

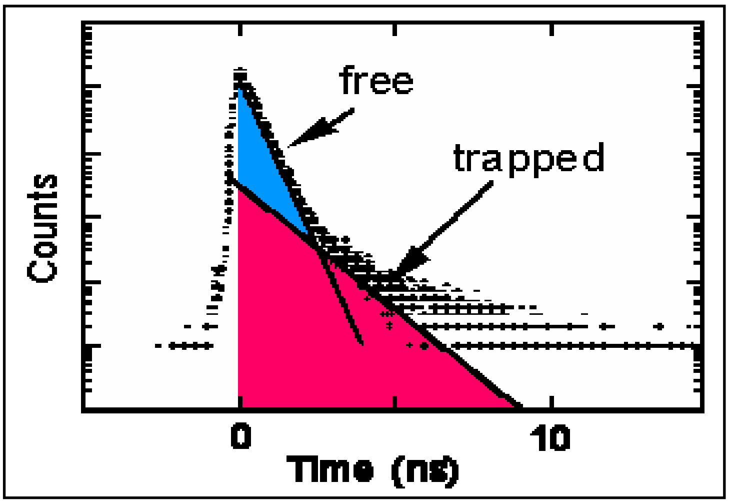

Fig.1.9. Positron annihilation lifetime spectrum reveals two decay constants: one corresponding to the lifetime in the bulk material and another to the lifetime in defects. The relative amplitude of the two signals gives the density of the defects in the material, while the lifetime in the defects gives the defect size.

PALS allows the determination of both the defect density and size. The relative amplitudes of the two decay curves give the defect density, while the lifetime of longer component can be used to determine the defect size and defect distribution. Measured results often coincide with theoretical predictions, thus observations can be clearly interpreted.

2.1. Introduction

The characterisation of amorphous networked materials is problematic because the structure of the materials is enormously complex, and a "complete" characterisation requires no less than the location of every atom in a macroscopic sample. While the periodicity of crystalline materials reduces this problem to locating every atom in a microscopically-sized unit cell, no such symmetry is present in amorphous materials, and determining their structure at this level is impossible. Rather, average properties (or simple property distributions) may be defined which one hopes will still be usable in the application and classification of the materials.

A porous material is simply some kind of solid material that has holes in it. The holes are also called pores. Porous media are generally characterised by a number of simple measures, the most common of which are the porosity, surface area, mean pore size and the more complex pore size distribution (PSD), which is the distribution of a ‘size’ parameter fitted to some experimental data. Generally, values of these measures are obtained by fitting experimental data to one of many models and reporting the corresponding property of the model. The models used may be either explicitly defined (as is the case for most methods of obtaining pore size distributions) or implicit in the data analysis procedure (common in methods for surface area such as alpha-plot analysis). In all cases, there are significant ambiguities in the definition of the quantity being measured and significant approximations in the model being used.

2.2. Preparation Methods of Porous Glasses

Controlled-pore glasses (CPGs) and the related Vycor glasses (PVGs) are highly interconnected mesoporous silica materials, which have excellent mechanical properties of porosities and average pore sizes [1]. Their preparation is based on the near-critical phase separation of a binary liquid mixture, which produces complex networked structures. Although CPGs were developed for use in size exclusion chromatography [1, 2], derivatised glasses can show a high chemical affinity for certain biomolecules and can even be used as catalytic agents and bioreactors [2].

The first preparations and characterizations of CPGs were done by Haller [3, 4] who partially phase-separated a mixture of 75 % SiO_2, 1-10 % Na_2O, and the rest B_2O_3. Then the molten glass is phase separated by cooling to between 500 and 800 ^oC. The time taken for this treatment determines the extent of phase separation and the resulting average pore sizes. The borate phase is leached out by acid solutions at high temperatures. Silica is dissolved in the primary alkali-rich borate phase formed during this procedure. Due to the very low solubility of silica in acid media, finely dispersed silica-gel remains in the cavities of the main silica framework and affects the pore structure of the resulting porous glass. The remaining glass contains colloidal silica particles, which are removed by a treatment with NaOH followed by washing with water. The interconnected structure of the soluble alkali-rich borate phase in the almost pure phase is an important precondition for the preparation of mechanically stable porous glasses. The Final CPGs can have porosity between 50 % and 75 %, an average pore size between 1 nm and 110 nm, and a surface area somewhere between 10 and 350 m^2/g, depending on the pore size [1]. An electron micrograph of a sample of CPG with 300 nm pores is shown in Fig. 2.1.

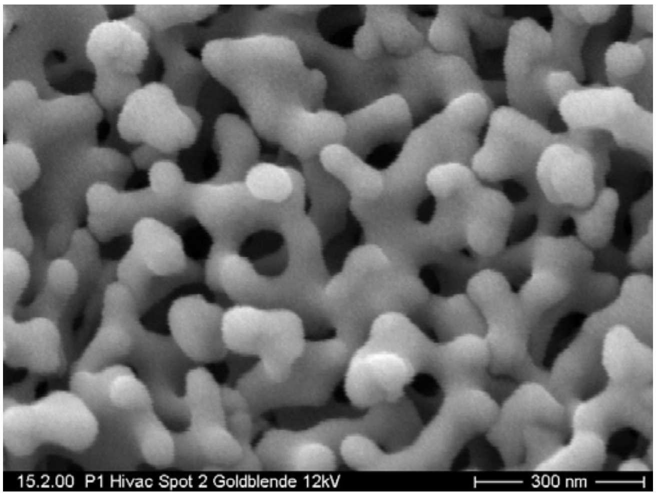

Fig. 2.1 Scanning electron micrograph of CPG of 30 nm mean pore size.

The structure and textural properties of the porous glasses are really determined by (a) the composition of the initial glass (b) the heat treatment conditions (temperature, time) and (c) the etching conditions [5-7]. For example, a heat treatment of the initial glasses in the temperature range between 580 ^{o}C and 700 ^{o}C is used for the preparation of macro porous glasses.

There are two different models describing the phase separation phenomenon. The first according to Haller [4], the phase separation in alkali borosilicate glasses proceeds via a nucleation and growth mechanism. The other one is based on theoretical studies by Cahn et al. [8, 9] that spinodal decomposition is responsible for the phase separation in alkali borosilicate glasses. However, the phase separation process proceeds very rapidly during cooling from the melt state. Quenching with very high cooling rates is necessary to investigate the early stage. Recently, Yazawa et al. [10] investigated that the pore volumes and the surface areas of the resulting porous glasses increased with decreasing cooling rate.

The pore size can be varied between < 2 and 10 nm by the conditions of the acidic leaching procedure. Shorter leaching times result in a micro porous glass. Longer leaching of the initial glass with acidic solution leads to mesoporous materials [7].

The commercial pore glasses VYCOR (PVGs) are prepared by a similar procedure [2, 11] from a glass mixture of typical composition 63 % SiO_2, 27 % B_2O_3, 6.6 % Na_2O, and the rest Al_2O_3. Where the glass is melted and formed into the desired shape and then held at a temperature above the annealing point but below that which would cause deformation. The material phase separates (on a microscopic scale) into two continuous phases, one rich in silica and the other in borosilicate and Alkali. It is then treated with a hot diluted acid solution, which dissolves away the borosilicate phase. Finally PVG is slowly heated to above 1200 ^{o}C. The finished glass is 96 % SiO_2, has a porosity closed to 28 %, an average internal pore diameter between 4 and 7 nm and a surface area of between 90 and 200 m^2/g calculated from Brunauer-Emmett-Teller (BET) analysis of the nitrogen adsorption isotherm [2].

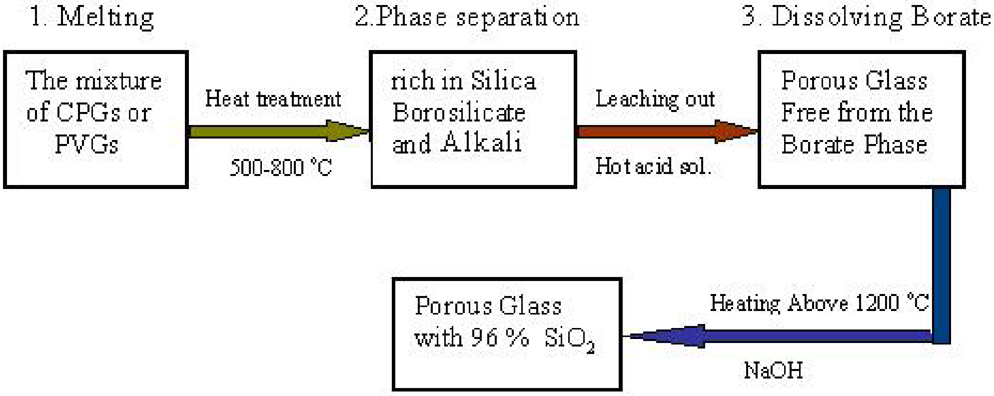

Fig. 2.2. Schematic diagram shows the procedures of control porous glass (CPG) materials.

Recently, ultra thin porous glass membranes with very flexible textural properties have been developed [12-16]. SiO_2-rich sodium borosilicate glass blocks were used as starting material. They were characterized by an identical chemical composition but different stages of decomposition. In the first step, small glass blocks were phase-separated in the temperature range between 530 and 720 ^{o}C. Then, ultra thin flat plates with variable geometry (i.e., 20 mm×20 mm) and thickness (80–500 μm) were prepared by special sawing techniques (Fig 2.3 a). In the last step, the glass plates were leached out by treatment with acid or combined acid and alkaline solution. Mechanically stable porous glass membranes with pore sizes in the range between 1 and 120 nm were obtained [14, 16]. The membrane properties can be adjusted to many applications. Some of the most interesting applications for the nonporous membranes come from the ability of nanoporous of certain size to let some substance pass and others not. Controlling the size of these pores accurately is one of the technological challenges faced in making these materials.

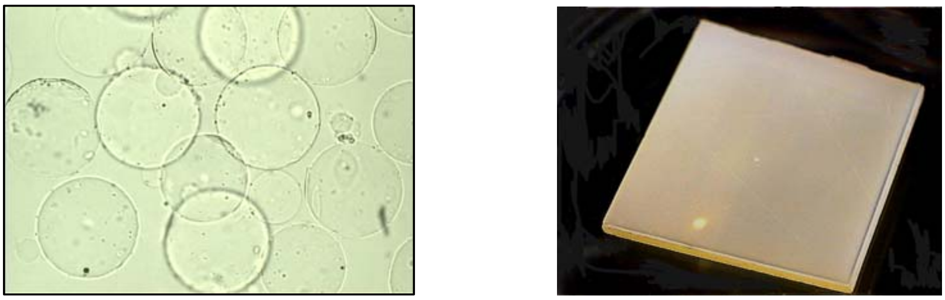

Fig. 2.3. Light microscopic pictures of (a) an ultra thin powder, and (b) a membrane for initial glass material. The pictures show the identical texture of the both types of glass before pores formation.

Several ‘‘new’’ techniques have been applied in recent years to investigate the pore structure of porous glasses. These are differential scanning calorimetry (DSC) [17], positron annihilation [18–23] and small-angle scattering (SAXS) [24–32]. SAXS measurements were used to determine the fractal dimensions [24, 25], to investigate polymer layers deposited on the surface of porous glasses [30, 31] and to study sorption and transport processes in PVG [32].

Resulting from a number of unique properties (very flexible geometric form and pore structure, chemical inertness, optical transparency, high mechanical and thermal stability, very reactive surface), porous glasses recommend themselves for many applications. In contrast to that, the high production costs and the limited number of geometric forms and pore sizes which are commercially available strongly reduce the industrial interest in porous glasses. This class of porous materials possesses a future only in such applications where one or more of the special properties are required. This justifies the high purchasing costs. Porous glasses are applied in biotechnology [33], membrane technology [34], micro-reaction engineering, dental industry [35], in heterogeneous catalysis as model catalyst supports [36,37], as reference materials for characterisation techniques (mercury intrusion), as starting materials for the preparation of new organic/inorganic composites (zeolite/PG) [38], as flexible host materials for the investigation of confinement effects [12,13] or as components for optical chemo sensors [39].

2.3. Gas Adsorption

When a gas or vapour is brought into contact with a solid, part of it is taken up by the solid. The molecules that dissappear from the gas either enter the inside of the solid, or remain on the outside attached to the surface. The former phenomenon is termed **absorption** (or dissolution) and the latter **adsorption**. When the phenomena occur simultaneously, the process is termed **sorption**. Then adsorption can be defined as the concentration of gas molecules near the surface of a solid material. The adsorbed gas is called adsorbate and the solid where adsorption takes place is known as the adsorbent. Adsorption is a physical phenomenon (usually called physisorption) that occurs at any environmental condition (pressure and temperature) but only at very low temperature it becomes measurable. Thus physisorption experiments are performed at very low temperature, usually at the boiling temperature (77 K) of liquid nitrogen (LN_2) at atmospheric pressure.

It is not always easy to tell whether the gas is inside the solid or merely at the surface because most practical' absorbents are very porous bodies with large internal' surfaces. It is not possible to determine the surface areas of such materials by optical or electron microscopy because of the size and complexity of the pores and channels of the material. The gas adsorption itself, however, can be used to determine the accesible surface area of most absorbents.

Adsorption takes place because of the presence of an intrinsic surface energy. When a material is exposed to a gas, an attractive force acts between the exposed surface of the solid and the gas molecules. The result of these forces is characterised as physical (or Van der Waals) adsorption, in contrast to the stronger chemical attractions associated with chemisorption. The surface area of a solid includes both the external surface and the internal surface of the pores.

Due to the weak bonds involved between gas molecules and the surface (less than 15 KJ/mole), adsorption is a reversible phenomenon. Gas physisorption is considered non-selective, thus filling the surface step by step (or layer by layer) depending on the available solid surface and the relative pressure. Filling the first layer enables the measurement of the surface area of the material, because the amount of gas adsorbed when the mono-layer is saturated is proportional to the entire surface area of the sample. The complete adsorption/desorption analysis is called an **adsorption isotherm**.

The pressure range is determined by the size range of the pores to be measured. Isotherms of microporous materials are measured over a pressure range of approximately 1.333×10^{-5} mbar to 0.13×10^{-4} mbar. Isotherms of mesoporous materials are typically measured over a pressure range of 1.33×10^{-4} mbar to approximately 1 mbar. Once details of the isotherm curve are accurately expressed as a series of pressure vs. quantity adsorbed data pairs, a number of different theories or models can be applied to determine the pore size distribution. Available micropore methods include: Density Functional Theory (DFT), MP-Method, Dubinin Plots (Dubinin-Radushkevich D-R, Dubinin-Astakov D-A), and Horvath-Kawazoe (H-K) calculations. Available Mesopore methods include: Barrett, Joyner and Halenda method (BJH), and Density Functional Theory (DFT) [40]. The analysis of t-Plot is also available for total micropore area as well.

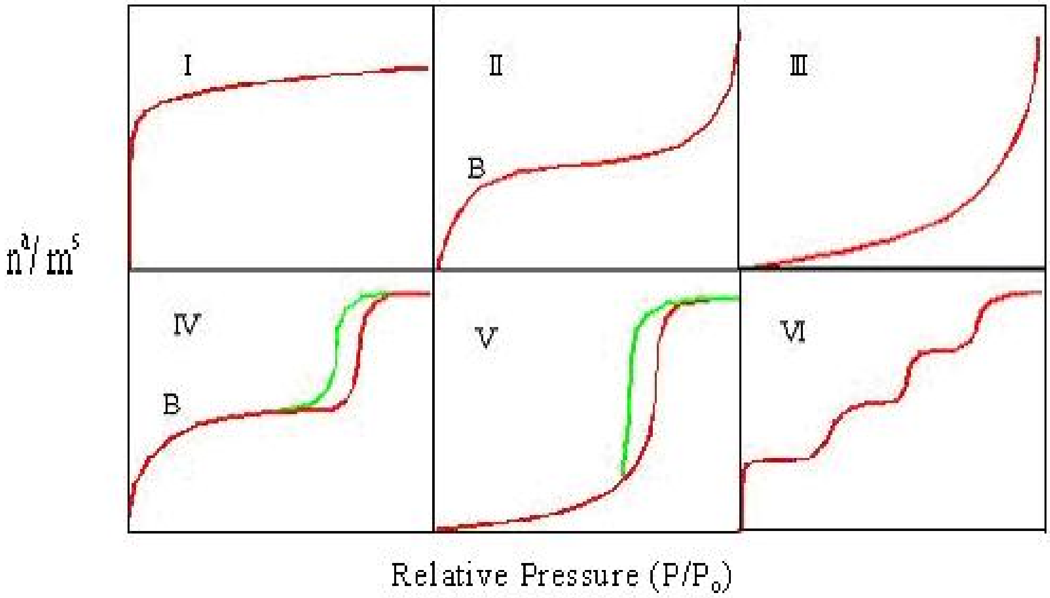

Fig. 2.4. The most frequently found types of gas physisorption isotherms, where n^a is the amount adsorbed and m^s mass of solid adsorbent.

The six IUPAC standard adsorption isotherms are shown in Fig.2.4, they differ because the systems demonstrate different gas/solid interactions. Type I isotherm is typical of microporous solids and chemisorption isotherms. Type II is shown by finely divided non-porous solids. Type III and type V are typical of vapor adsorption (i.e. water vapor on hydrophobic materials). Type VI and V feature a hysteresis loop generated by the capillary condensation of the adsorbate in the mesopores of the solid. Finally, the rare type VI step-like isotherm is shown by nitrogen adsorbed on special carbon.

Gas adsorption is of practical consequence to engineers and chemists in many ways. It can provide a convenient, cheap and reusable method for fluid purification and purification. More significantly, perhaps, the phenomenon of surface adsorption has been used to modify the rates of product yields of chemical reactions through **heterogeneous catalysis**. For a catalyst to be useful, it must have a large surface area, bind the reactants quickly and effectively, stabilize the activated complex, and release the products of the reaction. Thus the attraction of various molecules on the surface, as well as the total surface area of the catalyst, are extremely important properties of potential catalytic materials.

Once the isotherm is obtained, a number of calculation models can be applied to different regions of the adsorption isotherm to evaluate the specific surface area (i.e. BET, Dubinin, Langmuir, etc.) or the micro and mesopore volume and size distributions (i.e. BJH, DH, H&K, S&F, etc.) [40].

2.4. Pore Size, Shape, Volume and Pore Size Distributions

2.4.1. Pore Size, and Pore Shape

The pore systems of solids are of many different kinds. The individual pores may vary greatly both in size and in shape within a given solid, and between one solid and another. A feature of special interest for many purposes is the width w of the pores, e.g. the diameter of cylindrical pore, or the distance between the slit-shaped pore. Pore size defines an ability of the analyte molecules to penetrate inside the particle and interact with its inner surface. This is especially important because the ratio of the outer particle surface to its inner one is about 1:1000. The surface molecular interaction mainly occurs on the inner particle surface.

Pore dimensions cover a very wide range, and according to the International Union of Pure and Applied Chemistry (IUPAC) [41], pores are classified into three main groups depending on the access size: where pores between 0.7 to 2 nm in pores size are termed ***micropore***, those between 2 and 50 nm are termed ***mesopores***, and those greater than 50 nm are termed ***macropores***. Within recent years, the micropores range has therefore been subdivided into the very narrow pores of less than 0.7 nm in pores size which is termed or ***ultramicropore*** [42]. Where the enhancement effect is found, and ***supermicropores*** [43], which fill the gab between the ultramicropore and the mesopore range. Nanoporous materials are all about holes that are less than 100 nm, although there are some interesting microporous materials with holes a little above this size. It is convenient to divide nanoporous materials into bulk materials and membranes.

Pore shape is mainly unknown, but it could be approximated by the model. Three basic pore models exist:

a) cylindrical pores, circular in cross section
b) ink-bottle pores having a narrow neck and wide body
c) slit-shaped pores with parallel plates.

The pore size, whether quoted as a mean or most probable pore size or as part of a pore size distribution, is the least well-defined characterization of a material, but often considered the most useful and the most informative. Defining a pore size (or pore size distribution is generally a matter of selecting both a surface definition and a pore *shape* definition, and fitting some experimentally obtained quantity to a distribution of similar pores. In principle, the shape could be controlled by several independent variables, leading to a distribution of size and shape, but in practice this is never attempted. Practically, the pores are generally assumed to be either slit-shaped or cylindrical, leading to a single variable size parameter (wall spacing or cylinder radius). While these procedures may be fraught with small approximations introduced to make the models tractable, the central question of the meaning of these pore size distributions is difficult to address.

2.4.2. Pore Volume

The specific pore volume, V_p, is the sum of volumes of all pores in one gram of adsorbent. We have to refer that only internal volume inside the adsorbent particles is counted. Pore volume, V_p, specific surface area, A_{sp}, and mean pore diameter D are correlated to each other. Specific surface area is said to be inversely proportional to D. But, for the adsorbent with mean pore diameter of 10 nm and pore volume 0.5 ml/g , the surface area will be ~130 m^2/g. For the adsorbent with the same pore diameter but with the pore volume of 1 ml/g the specific surface area will be ~200 m^2/g. There is no exact relationship between these parameters. The correlation strongly depends on the adsorbent pore type and shape.

2.4.3. Pore Size Distributions (PSDs)

The majority of industrial materials and products consist of powders. Particle size distribution and shape are important physical characteristics that influence the behaviour during storage and processing. Whereas pore size is a measure of the diameter of the largest pore, pore size distribution (PSD) is a measure of the range of pore sizes. Then PSD can be defined as the distribution of pore volume with respect to pore size as shown in Fig. 2.5 (a); alternatively, it may be defined by the related distribution of pore area with respect to pore size as shown in Fig. 2.5 (b). The range of pore sizes can be normally distributed, and the spread can be quite narrow (e.g. the ratio of largest to smallest may be less than 2). On the other hand, pore size distribution can be very heterogeneous.

Pore size distributions (PSDs) are generally interpreted qualitatively, in order to determine how regular a material is (how sharp is its PSD) or whether the PSD is uni-modal or bi-modal. Certainly, increasingly complex material structures result in increasingly complex pore size distributions, but in general these measures cannot be reliably interpreted at a microscopic level without additional information on the morphology of the material.

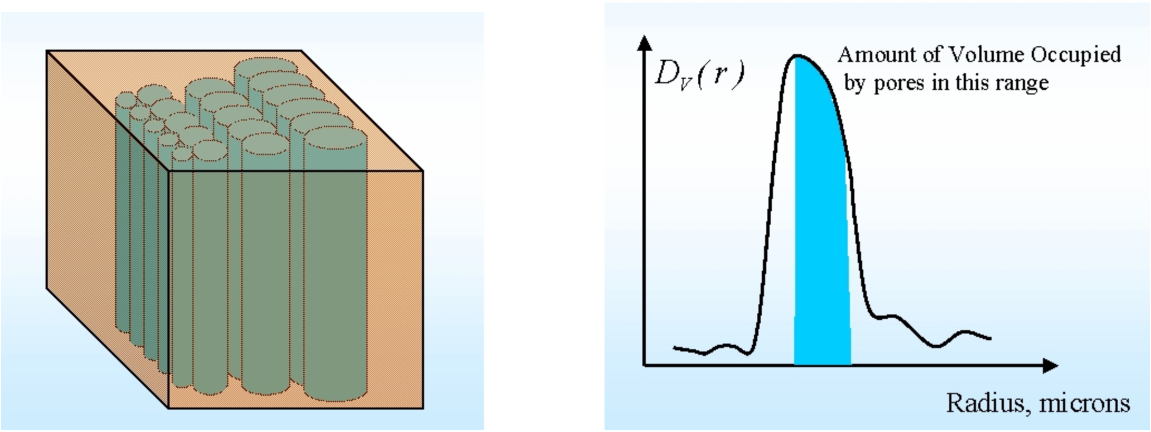

(a) (b)

Fig. 2.5. Schematic diagram of the pore distribution as a function of pore size.

Pore size and pore size distribution of porous materials can be determined by either gas adsorption porosimetry (typically N_2, Ar or CO_2) or Hg intrusion porosimetry. Gas porosimetry measures pores from 1.7 nm to about 400 nm in diameter. Mercury porosimetry is applicable to pores from 0.6 nm up to 900 nm in diameter.

2.5. Porosity and Network Properties

Porosity is the fraction of the pore volume occupied by pore space; or it is just the volume of the pores divided by the volume of the material. Many solid and powder materials both natural (stones, soils, minerals, etc.) and manufactured (catalysts, cement, pharmaceuticals, metal oxides, ceramics, carbons, zeolites, etc.) contain a certain void volume of empty space. This is distributed within the solid mass in the form of pores, cavities, and cracks of various shapes and sizes. The total sum of the void volume is called the porosity. The type and nature of porosity in natural materials depend on their formation (for instance rocks can be of igneous, sedimentary or metamorphic origin) while in man-made materials depend on their manufacturing and generally it can be controlled.

Porosity strongly determines important physical properties of materials such as durability, mechanical strength, permeability, adsorption properties, etc. The knowledge of pore structure is an important step in characterizing materials, predicting their behaviour.

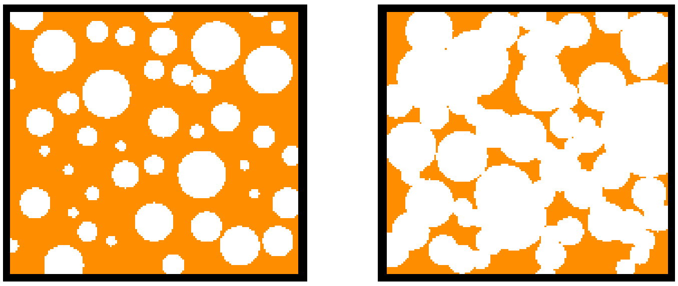

Fig. 2.6. Two-dimensional pictures of a) isolated circular pores, and b) connected pores.

The total porosity can be divided into effective porosity (open pores) and ineffective porosity (closed pores) as illustrated in Fig.2.6, in 2-D, where the pores are random size, non-overlapping circular holes. Closed pores are completely isolated from the external surface, not allowing the access of external fluids in neither liquid nor gaseous phase. Closed pores influence parameters like density, mechanical and thermal properties. Open pores are connected to the external surface and are therefore accessible to fluids, depending on the pore nature/size and the nature of fluid. Open pores can be further divided in dead-end or interconnected pores (catenary pores). Further classification is related to the pore shape, whenever is possible to determine it. For porous glasses, one usually assumes that the material is composed of a collection of cylinder diameters.

If the pores are completely isolated from each other, then it is clear that one can discuss the shape and size of individual pores. In this case, it is clear how to define the pore size distribution, a quantity which gives the number or volume of pores of a given size. If the pores are fully connected to each other, as is shown in the right side of Fig. 2.6, then there is really only one multiply-connected "pore" in the material. The number of pores is not a meaningful quantity anymore, and it is then difficult to talk about the shape and size of the "pores". However, in this case, the idea of "throats" can be important. If the pore space in many areas is shaped like the cartoon shown in Fig. 2.7, then the idea of a throat shape and size may be loosely defined. The size of the "throat" limits the accessibility of the larger "pore," and is then the size of importance for many properties of the material.

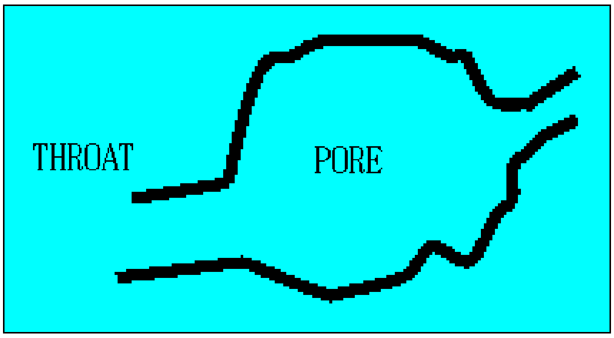

Fig. 2.7. Schematic picture defining a throat and pore in the pore space of a porous material.

The porosity and surface area of porous glasses are usually determined using nitrogen adsorption Brunauer-Emmett-Teller (BET) techniques [44]. Mercury intrusion porosimetry is also frequently used to estimate the pore size throat distribution of these glasses that is convolved with the cross-sectional throat shape and the topology of the pore-throat network. These techniques measure an equivalent circular cross-sectional throat diameter [45, 46]. In practice, pore-throat combinations can only be separated in terms of grossly simplified geometrical models of the pore micro geometry. In most cases, porous materials are random materials, with random pore sizes, shapes, and topology (It means, how the pores are connected, if at all). Because of this fact, most porous materials tend to be isotropic.

Porosity is often measured gravimetrically by filling the material with a gas or liquid and obtaining the volume of the pores from the mass of the adsorbed fluid. This procedure, while certainly accurate for large pore materials, requires assuming a constant adsorbate density throughout the pore system. In microporous and ultra micro porous materials where the ratio of surface area to volume is very high, the influence of the pore walls on the packing of gas or liquid molecules may not be negligible and will lead to systematic errors in these determinations. The characterization of solids in terms of porosity consists in determining the following parameters:

Specific pore volume and porosity: the internal void space in a porous material can be measured. It is generally expressed as a void volume (in ccm or ml) divided by a mass unit (g). **Pore size distribution:** it is generally represented as the relative abundance of the pore volume (as a percentage or a derivative) as a function of the pore size. **Bulk density:** Bulk density (or envelope density) is calculated by the ratio between the dry sample mass and the external sample volume. **Percentage porosity:** it is represented the ratio between the total pore volume and the external (envelope) sample volume multiplied by 100.

Nearly all the porous materials consist of a pore network, rather than a collection of individual "independent" pores. Quantitative (or even qualitative) descriptions of the properties of this network are rare in the literature, despite the (presumed) importance of the network topology to both the thermodynamics of confined fluids and the transport of fluid through a material. Quantities such as the topological connectivity of the network are not directly accessible by experiment. Indeed, the much-discussed phenomenon of adsorption hysteresis is often discussed in terms of "pore-blocking" resulting from particular pore network structures, which themselves are hardly understood.

2.6. Surface Area Measurements

2.6.1. Introduction

Why is surface area so important? Because surface area is the means by which a solid interacts with its surroundings, be it gas, liquid or other solids. The surface area of a solid material is the total surface of the sample that is in contact with the external environment. The surface area results from the contribution of the internal surface area of the pores plus the external surface area of the solid or the particles (in case of powders). It is expressed as square meters per gram of dry sample, or it can also be expressed as the specific surface as a ratio of pore surface per pore volume. Porous materials having a significant volume of very small pores might exhibit a surface area larger than a football field - several thousand square meters per gram. Whenever a significant porosity is present, the fraction of the external surface area to the total surface area is small. Surface area is strongly related to the pore size and the pore volume i.e. the larger the pore volume the larger the surface area and the smaller the pore size the higher the surface area. Furthermore, the generation of porosity, especially when due to small pores, can produce surface area far in excess of that produced by particle size reduction. The surface area of a micro porous material is also a somewhat ambiguous concept, for two reasons. Firstly, the microscopic definition of the molecular surface is arbitrarily defined, and there are several sensible and intuitive definitions available, which can yield significantly different results under certain circumstances. Secondly, once a suitable surface definition has been chosen, the roughness of the surface must be accommodated. All surfaces are highly corrugated at the atomic scale, which can give higher than expected surface areas if microscopic definitions are used; this is a continuing source of difficulty in comparisons of simulated and experimental results on porous materials.

Specific surface area which is surface area per unit mass (usually m^2/g), is often correlated with rates of dissolution and other rate-related phenomena such as catalyst activity, electrostatic properties of powders, light scattering, opacity, sintering properties, glazing, moisture retention, shelf-life and many other properties which can influence the processing and behaviour of powders and porous solids. On very coarse powders the specific surface area can be as low as a few square centimetres per gram, while on finer powders it might be a few square meters per gram.

Therefore, surface area measurement is probably the most widely used means to characterise porous materials. Since the surface area corresponds to the roughness of the particle exterior and its porous interior, gas sorption is the preferred technique. In contrast, particle sizing techniques, for example, calculate assumed area values based on smooth, non porous spheres.

2.6.2. Specific and Total Surface Area

There are different methods used to measure the surface area and each method can yield different results. Experimental surface areas are mostly obtained through the analysis of the isothermal adsorption/desorption of nitrogen at (77 K) and relative pressure (*P*/*P*o) ranging from 0.05- 1.0. The BET equation [44] is commonly used to calculate the surface area for multilayer adsorption:

$$\frac{P/P_o}{V_a\left(1-P/P_o\right)}=\frac{1}{V_m C}+\frac{C-1}{V_m C}\left(P/P_o\right) \qquad (2.1)$$

where P, P_0, V_a, V_m, are the adsorption pressure, the saturation vapour pressure, the volume of gas adsorbed on one square centimetre of the surface at pressure *P*, the volume of gas adsorbed when the entire surface is covered with a complete monomolecular layer respectively, and *C* is a constant indicating the differences of the heat of adsorption of the first layer and heat of liquefaction of the adsorptive. Through the slope and intercept of a plot of $P/[\ V_a(P_O-P)]$ against (P/P_O), V_m can be resolved. Figure 2.8 shows the graphical form of the BET isotherm equation. Thus the values of V_m and *C* may be obtained from a plot of a straight line. The specific surface area of 1 gm of the adsorbent, A_{sp}, can then be determined from:

$$A_{sp(BET)}=\frac{V_M\,\sigma_n\,N_A}{m_s\,V_a} \qquad (2.2)$$

Where m^s, σ_n , N_A are the mass of the sample, the cross-section area of a single nitrogen molecule (16.2 A^2) and the Avogadro's number respectively.

The surface area of a sample can be calculated by using the area which is occupied by a single adsorbate molecule. This area may be expressed under the assumption of a close packing of spherical molecules at the surface by Eq.2.3 [48].

$$\sigma_n = 1.091\left(\frac{M}{N_A\, d_L}\right)^{2/3} \qquad (2.3)$$

where 1.091 is the coefficient related to the spherical shape and hexagonal close packing of molecules, M is the molecular weight, and d_L is the density of the liquid adsorbate (which is obtained experimentally using a reference system of known surface area). The accuracy of this method requires that the monolayer density be transferable; that it is not dependent on the surface curvature or pore structure, and not strongly dependent on the chemistry of the underlying surface. The mono-layer thickness of N_2 at 77 K has a thickness in the order of 0.354 nm. The specific surface area that can be determined by gas sorption ranges from 0.01 to over 2000 m^2/g.

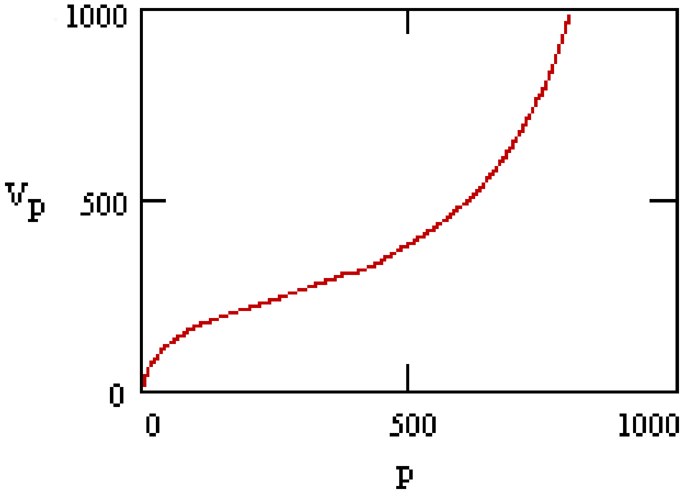

Fig. 2. 8. Theoretically-obtained adsorption BET-model graph for surface area determination.

The data from the multipoint determination are used to calculate the matrix surface area by use of the t-plot method of Lippens and de Boers [48]. They determined the multi-layer adsorption curve for nitrogen at different pressures and constant temperature is identical for a wide variety of adsorbents, provided that no capillary condensation occurs. They referred to this curve as the universal multimolecular adsorption curve or t-curve. The experimental points of this t-curve were found to give good agreement with the isotherm equation of Harkins and Jura [49].

$$t = \left[\frac{13.99}{\log\left(P_o/P\right) + 0.34}\right]^{1/2} \qquad (3.4)$$

Lippens and de Boer proposed plotting the volumes of nitrogen adsorbed (V) at different P/Po values as a function of t value from the above formula (Eq.3.4). For multimolecular adsorption, the experimental points should fall in a straight line and pass through the origin for a non-porous material. The slope (V/t) of this line and the relationship surface area, slope = 15.47 (V/t) gives the specific area of the catalyst in square meters per gram (m^2/g). For a porous material, the line will have a positive intercept indicating micropores, or deviate from linearity suggesting filling of mesopores. For most materials, the linear portion of the curve between t = 0.35 to 6 nm is used for determination of matrix surface area.

2.7. Static Volumetric Gas Adsorption

Static volumetric gas adsorption requires a high vacuum pumping system, able to generate a good vacuum over the sample (at least 1.33×10^{-4} mbar) to assure the correct vacuum degree in the sample holder during the pre-treatment and before the analysis start. The system features stainless steel plumbing with high vacuum fittings to ensure precise results as the experiment is carried out starting from high vacuum and increasing step by step the pressure up to the adsorbate saturation pressure.

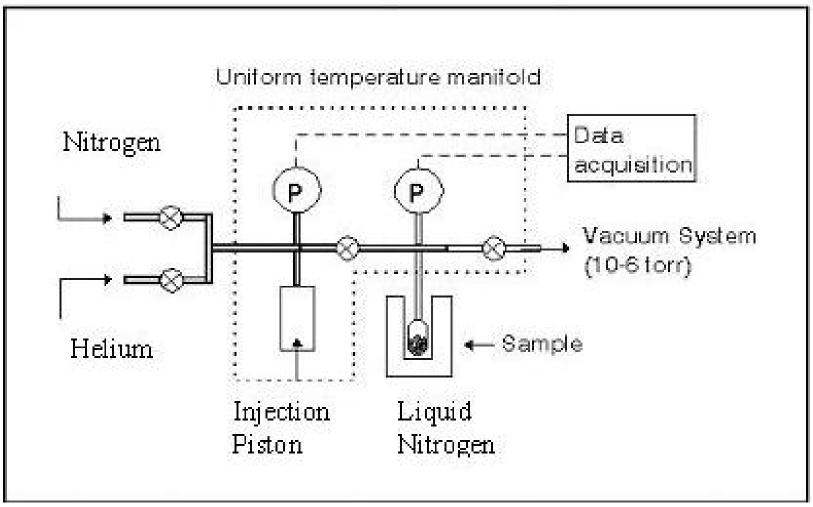

Fig. 2. 9. Schematic diagram of the elements of a volumetric adsorption apparatus.

A schematic of the Sorptomatic 1990 is shown in Fig. 2.9, where it is based on the static volumetric principle to characterize solid samples by the technique of gas adsorption. It is designed to perform both physisorption and chemisorption enabling determination of the total specific surface area, porosity and the specific surface area of metals present and their dispersion over the surface. The principle behind this method consists of introducing consecutive known amounts of adsorbate to the sample holder, which is kept at liquid nitrogen temperature (77 K). Adsorption of the injected gas onto the sample causes the pressure to slowly decrease until an equilibrium pressure is established in the manifold.

The injection system of the Sorptomatic 1990 consists of a calibrated piston, where both the pressure and the injection volume can be automatically varied by the system according to the adsorption rate and the required resolution. The piston method is advantageous over other methods as it does not increasing the manifold dead volume while the system is waiting for pressure equilibration. A small dead volume over the sample makes the instrument very sensitive to the amount of gas adsorbed. The equilibrium pressure is measured by two pressure transducers chosen according to the pressure range where adsorption is established during the experiment. The raw experimental data are the equilibrium pressures and the amount of gas adsorbed for each step. The gas uptake is calculated directly from the equilibrium pressure values but a dead volume calibration has to be performed before or after the measurement by a "blank run" (that is an analysis using an inert gas not adsorbed on the sample in the analytical conditions, most commonly used is helium). The final degassing before the analysis can be performed in a flow of inert gas or under very high vacuum conditions to clean completely the activated sample surface and to perform reliable and reproducible measurements.

The static volumetric method is very precise and is considered as a very accurate technique to evaluate surface area and pore size in the region of micro and mesopores. However, it is not advisable whenever a fast measurement of surface area is required, because this method involves long analysis time that are required to produce highly accurate and reliable results.

2.8. Mercury Intrusion Porosimetry (MIP)

Mercury porosimetry is widely accepted as a standard method to characterize porous solids with respect to their pore volume (porosity) and pore size distribution over a wide range of pore sizes from 0.0036 µm up to ca. 400 µm. Few other techniques exist that are able to measure the same range of pore sizes. In addition, mercury porosimetry data can be interpreted in terms of particle size distributions, surface area, permeability, bulk and absolute densities of solid and powder, fractal dimension and compressibility, as well as to account for pore shapes and network effects in any porous solid. Hence, over the course of several decades, mercury porosimetry has proven to be of substantial value to industries dealing for instance with catalysts, ceramics, minerals, coals, soils, and pharmaceuticals.

Mercury intrusion porosimetry involves placing the sample in a penetrometer, then surrounding the sample with mercury. Mercury is a non-wetting liquid for almost all substances and consequently it has to be forced into the pores of these materials. The pressure at which mercury enters a pore is inversely proportional to the size of the opening to the void. As the applied pressure is increased the mercury is forced to enter pores within the sample material. Thus, the radius of the pores which can be filled with mercury decreases and consequently the total amount of mercury intruded increases. This change in the pore volume is measured in capacitance of capillary of the penetrometer, which is proportional to the intrusion volume. This intrusion volume is recorded with the corresponding pressure or pore size.

Determination of the pore size by mercury penetration is based on the behaviour of non-wetting liquids in capillaries. A liquid cannot spontaneously enter a small pore which has a wetting angle of more than 90 degrees because of the surface tension (capillary depression), however this resistance may be overcome by exerting a certain external pressure. The interpretation of mercury porosimetry data is traditionally based on the use of the Washburn equation [50], that is, $Pr = -2\,\Gamma \cos\theta$, where, P is the pressure that must be applied to nonwetting liquid mercury to penetrate cylindrical pores of radius r and Γ and θ are the mercury surface tension and contact angles, respectively. Accordingly, pore size distributions are simply obtained by monitoring the volume of mercury intruded into pores as a function of applied pressure. A significant feature of all mercury porosimetry curves is the occurrence of hysteresis between the intrusion and extrusion branch. In addition, very often so called entrapment is observed, i.e., mercury remains contained in the porous network. Both phenomena can be seen in Fig 2.10, which shows two experimental mercury intrusion/extrusion cycles. The CPG in the institute for technical and macromolecular chemistry in Halle at MLU utilizes the Passcal-440 Series for our mercury porosimetry measurements.

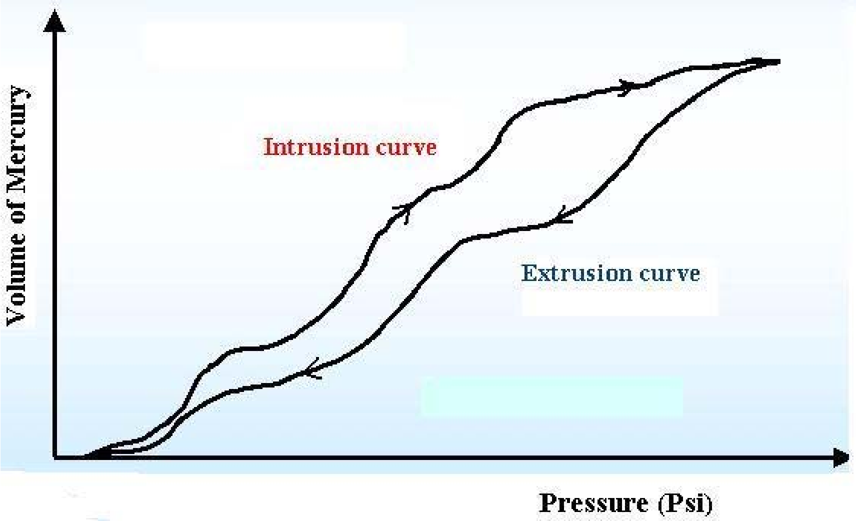

Fig. 2. 10. Schematic diagram of the mercury intrusion/ extrusion cycle.

3. 1. Introduction

In the last three decades, PALS has become a popular tool in determination of the mean size and size distribution of free volumes in solids, particularly in polymers and porous materials [1-23]. However, the interpretation of results gained by PALS in grainy and porous media was and still is ambiguous. The interest in using PAS to probe materials is that understanding the physics of matter-antimatter decay allows one to then extract nano-scale materials information specific to the location at which the localization annihilation takes place. Moreover, PAS does not depend on the pore interconnectivity, which is difficult to probe with standard techniques (such as gas absorption technique)

When energetic positrons (< 0.5 MeV) are implanted into molecular solids such as polymer or other porous glass or zeolites, they rapidly lose their energy due to the ionization of molecules in the medium matrix. The excitation of phonons dominates when the positron energy has degraded below the ionization threshold. Positrons reach thermal equilibrium within the medium, during a few ps, this process is called thermalization. The initial kinetic energy of positrons drops down to thermal energy (0.027 eV at 300 K). After reaching thermal equilibrium with the host medium, the positron state develops as a diffusion process. During diffusion, the thermalized positrons may then annihilate as a free positron with the electrons in the matrix ($\tau \approx 0.4$ ns) and will normally yield 2γ-rays ($2m_ec^2$) in opposite directions or migrate to the pores where a fraction forms Ps prior annihilation.

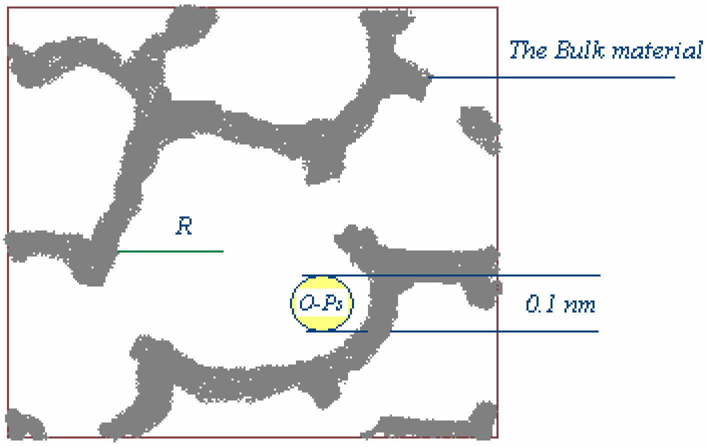

Fig. 3. 1. A cross-sectional view of in situ nature of the Ps as a probe for pores in interconnected porous material. Ps is preferentially localized in pore with a mean radius *R* before the annihilation occurs.

This particle is an analogue of the hydrogen atom with binding energy of order 6.8 eV and its diameter (equal to the distance between e^- and e^+) is 0.1 nm [23]. Ps can exist in two different spin states, either in the singlet state (*p*-Ps, parallel e^--e^+ spins) or triplet state (*o*-Ps, anti-parallel spins). In vacuum the singlet state (*p*-Ps) decays with a short lifetime (~ 0.125 ns) via the emission of 2γ-rays (self-annihilation) which in the electron-positron centre of mass frame each has energy of 0.511 MeV in order to conserve energy, momentum and spin and a narrow energy distribution. The triplet state (*o*-Ps) decays with long lifetime (~ 142 ns) via emission of 3γ-rays (self-annihilation) with a total energy of 1.022 MeV and in various directions relative to each other and the energy distribution extending from 0 to 0.511 MeV. The *o*-Ps trapping in interconnected porous glass with radius *R* is visualized in Fig. 3.1.

In free sites within molecular materials, *o*-Ps will suffer from large number of collisions with the pores walls. This may reduce the *o*-Ps long-lived component through the decay with an electron other than its bound collaborate and of opposite spin via the emission of *2γ*-rays with 0.511 MeV. This is so called "pick-off" annihilation and reduces the *o*-Ps lifetime from 142 ns in vacuum to the low ns range ($\tau > 0.5$ ns).

In small free sites, the *o*-Ps may be subsequent to a transformation to *p*-Ps, which rapidly annihilates via the emission of 2γ- rays, and this process is named ‘‘quenching’’ [20]. Therefore, the size of the free volume hole is reflected in the o-Ps lifetime. As the hole size decreases, the probability of pick off annihilation increases and reducing the mean *o*-Ps lifetime [21].

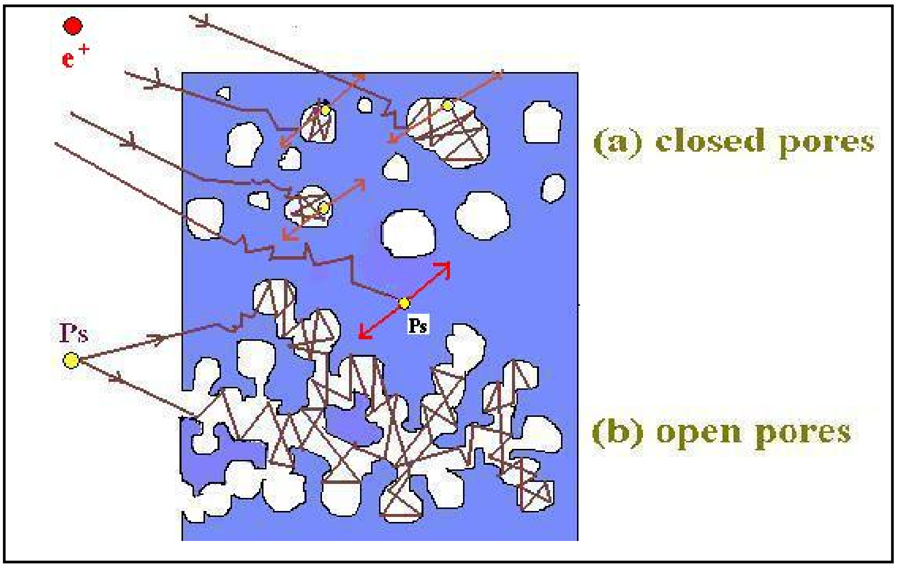

Fig. 3.2. Positronium formation and annihilation in closed and open pores.

As a result of positron or Ps trapping in low electron density sites, such as open-volume defects or free volumes, pores and cavities, additional long lifetime exponential components occur in the measured lifetime spectra. In vacuum and with larger empty voids or pores with vacuum inside these lifetimes up to 142 ns are characteristic for the pore size, as for example porous oxides, silicates, zeolites, activated carbons and resins [1-6, 8-24]. More than three components were found to be necessary to describe the spectra [1, 9, 11-14, 23] depending on the properties of the material under investigation. The Ps decay rate is the sum of its natural (intrinsic) decay rate and the pick-off annihilation rate λ_{po} caused by the penetration of the Ps into the pore walls. Some fraction of Ps may annihilate also from structural defects (micropores) in the higher density region of material. Figure 3.2 illustrates of the Ps formation and collisions in closed and opened porous materials.

As known before, the mean lifetime τ is the reciprocal of the decay rate λ, which corresponds the slope of the number of counts versus the time in half-logarithmic scale (see Eq.3.1 below). Thus, the resulting lifetime of the trapped *o*-Ps can be related to the size of the trapping site and may be used as a size spectroscopy in the sub-nano and nano-meter scale. The exponential decay of the components with time (t) calculates according to

$$N(t) = \sum_{i=1}^{k} \frac{I_i}{\tau_i} \exp\left(-\frac{t}{\tau_i} \right) \tag{3.1}$$

The mean lifetime (τ_i) and intensities (I_i) of the different components are then obtained by applying nonlinear fit routines on the spectra. In half-logarithmic plot of the lifetime spectra, the different lifetime components are noticeable as linear fractions with different slopes. The steeper the slope, the shorter the mean lifetime (τ) of the specific component. The lifetime of the long-lived species may depend not only dependent on the pores sizes but also on the surface parameters as for example active sites on the surfaces and in the pores [6, 9].

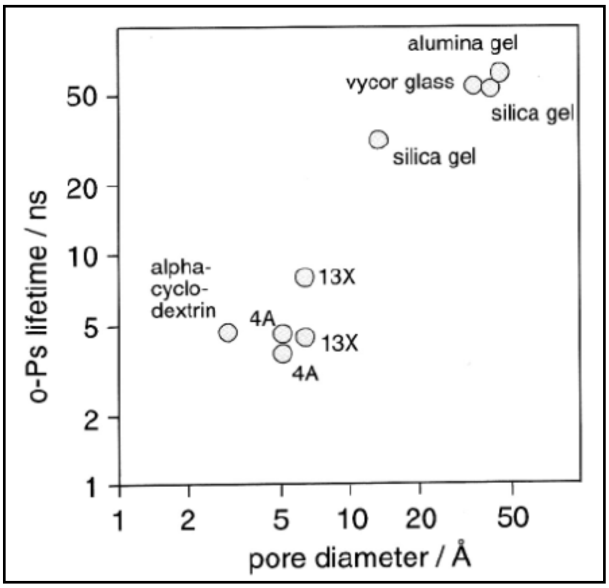

Fig.3.3. The correlation between *o*-Ps lifetime and the pore diameter of various materials [5].

However, Fig.3.3 shows the data points which were collected from the literature [1, 24-26] by Nakanishi and Ujihira, who added own data to the plot. Despite the fact that the data points were determined from very different materials, there is a significant linearity between the actual lifetimes of *o*-Ps with the pore sizes of different materials in the double-logarithmic plot. In the case that no interaction with specific surface species occurs, the lifetime appears to be mainly determined by the size of the pores. Therefore, it is essential that a unique relation should be found between the lifetime of the *o*-Ps and the size of the trapping site, and that this relation can be calibrated numerically to a wide range of experimental data.

3.2. Small Pores ($R \leq 1$ nm)

3.2.1. Spherical Geometry:Tao-Eldrup Model

The relation between the free volume size R and the *o*-Ps lifetime was assumed by Tao [2] and modified by Eldrup [3]. In the Tao-Eldrup model a spherical pore described by a rectangular potential well of the radius R and a finite potential barrier ΔV is substituted by a well with an infinite potential barrier V and a size $R + \Delta R$. By this construction the wave function of the Ps occupying the ground state of the infinite potential well overlaps with bulk (electron layer in the wall of the pore) in the range between R and $R + \Delta R$. ΔR is used as an empirical parameter as shown in Fig. 3.4.

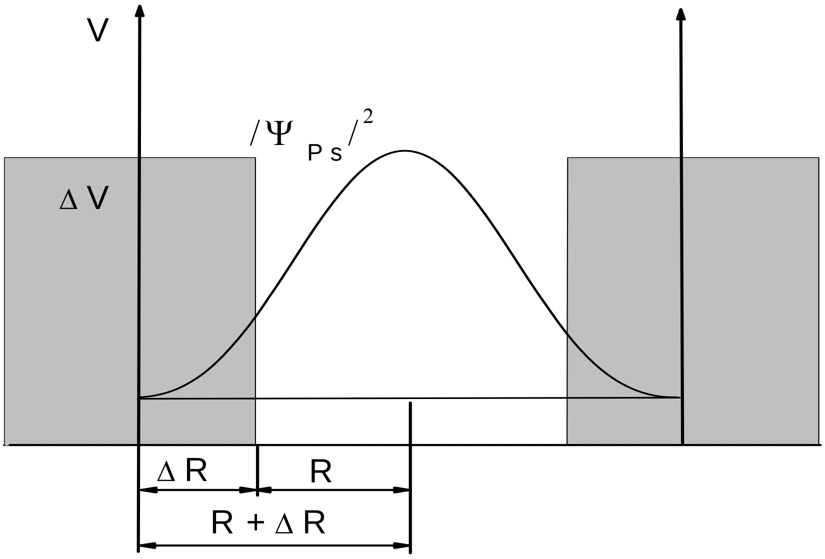

Fig. 3.4. In the Tao-Eldrup model a spherical pore described by a rectangular potential well of the radius R and a finite potential barrier ΔV is substituted by a well with an infinite potential barrier V and a size $R + \Delta R$. By this construction the wave function $\Psi_{Ps}(r) = N \sin[\pi r/(R+\Delta R)]/r$ of the Ps occupying the ground state of the infinite spherical potential well, overlaps with the bulk (electron layer in the wall of the pore) in the range between R and $R + \Delta R$. ΔR is used as an empirical parameter which is, however, the same for all materials.

In its lowest state, the wave-function, Ψ, of the Ps is $(\sin Ar)/r$ if $0 \leq r \leq R$ (inside the potential well) and $\exp(-Kr)/r$ if $r > R$ (outside the well) [20]. The rate of the *o*-Ps pick-off annihilation λ_{po} then is equal to the annihilation rate in the bulk λ_a multiplied with the probability P to find the Ps outside the well. Integration of $|\Psi(r)|^2 * r^2$ starting from R, where the electron density starts to be non-zero (boundary of the finite potential well), up to infinity calculates this probability. In order to substitute these complex calculations by more simple ones, Tao proposed a model based on rectangular potential wells with infinitely high walls.

In an infinite potential well the wave-function has no extension outside the well. In order to realize the penetration of the wavefunction outside the pore, Tao [2] defined a broadening of the well by an empirical parameter ΔR (electron layer thickness), which describes the overlapping of the Ps wave function into the pores wall. The emperical value of ΔR in the literatures used very frequently is $\Delta R = 0.166$ and 0.1656 nm [7, 16].

The overall annihilation rate of *o*-Ps, $\lambda_{\text{o-Ps}}=1/\tau_{\text{o-Ps}}$, is calculated by averaging the annihilation rate over the volume of the pore using the square of the *o*-Ps wave function as a weighting factor. To calculate the overlap of the wave function with the electron layer, integration had been performed from R to $R + \Delta R$.

Inside the electronic layer ($R+\Delta R \geq r \geq R$) the electron density is constant and the annihilation rate of the *o*-Ps is assumed to be $(2\text{ ns})^{-1}$, which is the spin-averaged annihilation rate of the *p*-Ps and *o*-Ps states, $\lambda_a = (\lambda_s + 3\lambda_T)/4$, where λ_s and λ_T are the self-decay rates of the singlet (2γ) and triplet states (3γ) respectively [5,11-18]. The decay rate of the *o*-Ps localized at a hole is given by

$$\lambda_{o-Ps}(R) = 1/\tau_{o-Ps}(R) = \lambda_{po} + \lambda_T \tag{3.1a1}$$

Since usually $P \ll 1$, eq. (3.1a) is frequently used in the form

$$\lambda_{o-Ps}(R) = \lambda_a P + \lambda_T (1-P) \tag{3.1a2}$$

or, with $\lambda_a = (\lambda_s + 3\lambda_T)/4$,

$$\lambda_{o-Ps}(R) = \lambda_a - \left[\left(\tfrac{1}{4}\right)\left(\lambda_s - \lambda_T\right) \right](1-P) \tag{3.1a3}$$

where $\lambda_{\text{po}} = \lambda_a P$, where P is the probability finding *o*-Ps inside the electron layer of thickness ΔR. In small voids or pores the pick-off annihilation will dominate, hence the term λ_T can be neglected. Then, the probability P of finding the Ps inside the electron layer between R and $R+\Delta R$ is given by

$$P(R) = 1 - \left(\int_0^R |\Psi|^2 r^2 \, dr \Big/ \int_0^{R+\Delta R} |\Psi|^2 r^2 \, dr \right) \tag{3.1b}$$

with $\Psi(r)$ = radial part of the wave function.

For particles in a potential well with spherical geometry, the wave-functions are spherical Bessel function $J_l(r)$ and for the lowest state $J_0(r) = (\sin Ar)/r$. The value of A is obtained by considering that the wave function $\Psi(r) = ((\sin Ar)/r)$ of the *o*-Ps does not extend outside the radius $R + \Delta R$, which means it has to be zero at $r = R + \Delta R$. This is fulfilled if $Ar = \pi$, and with $r = R + \Delta R$ that $A = \pi/(R + \Delta R)$. The wave function thus has the form

$$\Psi(r) = N\sin\left(\pi r/(R + \Delta R)\right)/r \tag{3.1c}$$

where N is an normalization factor given as $N = (1/(2\pi(R+\Delta R)))^{0.5}$ and determined so that $4\pi\int |\Psi_{Ps}(r)|^2 r^2\, dr = 1$.

The Pick-off rate is calculated as

$$\lambda_{po} = \lambda_a\left[1 - \left(\int_0^R sin^2\left(\frac{\pi r}{R + \Delta R}\right)dr \Big/ \int_0^{R+\Delta R} sin^2\left(\frac{\pi r}{R + \Delta R}\right)dr\right)\right] \tag{3.1d}$$

The integral calculated according to

$$\int \sin^2(x)\,dx = \frac{1}{2}x - \frac{1}{4}\sin(2x) \tag{3.1e}$$

As the result then one obtains the well known Tao-Eldrup equation [2, 3]

$$\lambda_{TE} = \lambda_{po} = \lambda_a\left(1 - \frac{R}{R + \Delta R} + \frac{1}{2\pi}\sin\frac{2\pi R}{R + \Delta R}\right) \tag{3.2}$$

where $\lambda_a = 2$ ns^{-1}, so from the λ_{po} we can deduce the radius R of the pore. $R + \Delta R$ is the radius of the potential well.

Eq.3.2 is commonly used for determination of the free volumes of molecular crystals and polymers [7]. In spite of all simplifications, the TE-model (Eq. 3.2) describes well the *o*-Ps lifetime in small voids ($R \leq 1$ nm): it was successfully applied to Ps bubbles in the liquids, free volumes in polymers, vacancies in plastic crystals, and cavities in zeolites.

The solid line in Fig.3.5 shows the theoretical *o*-Ps lifetimes according to Tao-Eldrup Eq.3.2, accounting only for the contribution of the Pick-off annihilation. As we can recognize, the agreement between the calculated and experimental data is acceptable for voids of a size less than 1 nm. Hence, the TE-model works successfully in the case of small free volumes. When $R \leq 1$ nm and according to TE-model there is no temperature dependence λ_{po}, where the spacing of the levels in the well is so far (much larger than K_BT), hence only the 1s state is populated.

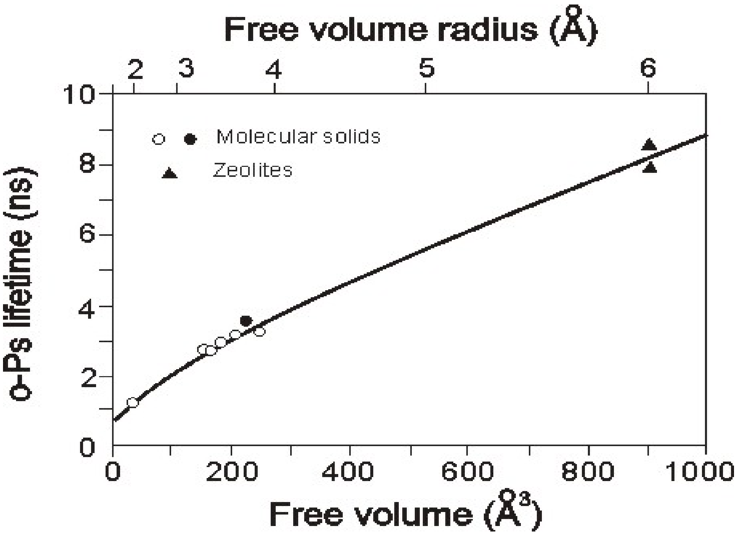

Fig. 3.5. The correlation between the measured *o*-Ps lifetime and the size of free-volume in molecular solids and zeolities [3, 5]. The solid line is the best fit of Eq.3.2 to known cavity volume of molecular systems leading to $\Delta R = 0.166$ nm**.**

3.2.2. Rectangular Geometry

A nonspherical pore model based on cuboids shaped pores (rectangular parallel piped) with side lengths a_i for the calculation of *o*-Ps lifetimes have been proposed by Jasinka et al. [15, 16]. For long channels the side length was assumed to be infinite. In this model the *o*-Ps lifetime follows the formula

$$\lambda_{po} = 1/\tau_{po} = \lambda_a \left\{ 1 - \prod_{i=1}^{3} \left[\frac{a_i}{a_{ih} + 2\Delta R} + \frac{1}{\pi} \sin\left(\frac{\pi a_i}{a_{ih} + 2\Delta R}\right) \right] \right\} \tag{3.3a}$$

where a_{ih} is the pore size with the side length $a_i = a_{ih} + 2\Delta R$ of the potential. Thus, with the rule $\sin(x - y) = \sin x \cos y - \cos x \sin y$, Eq.3.3a transforms to the following formula (Gidley et al. [11, 12]).

$$\lambda_{po} = 1/\tau_{po} = \lambda_a \left\{ 1 - \prod_{i=1}^{3} \left[1 - \frac{2\Delta R}{a_{i0}} + \frac{1}{\pi} \sin\left(\frac{2\pi \Delta R}{a_{i0}}\right) \right] \right\} \tag{3.3b}$$

3.3. Large Pore sizes: Extension of TE-Model

3.3.1. Tokyo-model (semiphenomenological model)

It has become clear that the simple quantum mechanical model of Tao-Eldrup (Eq.3.2), fails to find a good correlation between the lifetimes of the *o*-Ps at the pore size larger than 1 nm. This non-correlation is obviously due to the elimination of the contribution from the self *o*-Ps annihilation process, which becomes increasingly significant as the *o*-Ps lifetime approaches the vacuum value (λ_T=1/142 ns).

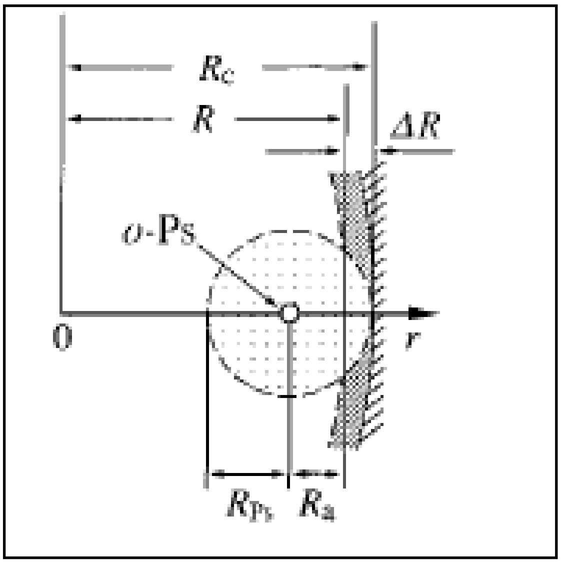

Fig. 3.6. Schematic diagram of the Tokyo- model for the *o*-Ps annihilation in large pore. R_{ps} represents a quantum radius of *o*-Ps [10], where the annihilation process can be described by Eq.3.2.

Semiphenomenological model was assumed by a group from the University of Tokyo [10] to overcome this discrepancy and to calibrate *o*-Ps lifetimes in large pore sizes. In this model the spherical pore geometry has been suggested with an infinite potential well but in most cases it cannot be determined how pore radii were calibrated. Moreover, the *o*-Ps particle is no longer represented by a standing wave function in a potential well but behaves more like a quantum particle, bouncing back and forth between the energy barriers as the potential well becomes large.

Therefore, the *o*-Ps can be described by a Gaussian wave packet as well as two regions were assumed for *o*-Ps annihilation in a large cavity or voids; (i) close to the porous wall ($R \geq R_a$), where o-Ps can annihilate via the pick-off process inside a pore of Radius R_a, weighted by the probability of finding the *o*-Ps atom inside a sphere of radius R_a. (ii) At the centre ($R < R_a$), where *o*-Ps mainly annihilates via self-annihilation 3γ-rays inside a pore of Radius R_a. The addition of this term leads to a better description of the measured average annihilation rate ($\lambda(R) = 1/\tau(R)$). A Parameter R_{ps} is introduced to define the boundary of the Ps particle near the pore wall as shown in Fig.3.6. The term (R-R_a) defines the boundary conditions of the spherical volume, where *o*-Ps wave packets do not interact with the electron cloud at the surface of the pore wall. Thus the *o*-Ps annihilation rate according to the Tokyo model in the large pore is represented as;

$$\lambda_{\text{Tokyo}}(R) = \lambda_{TE}(R) + \lambda_T = (\lambda_{po}\, P(R) + \lambda_T) \tag{3.4a}$$

For simplicity, the probability P(R) of finding the *o*-Ps inside of a sphere of radius (R-R_a) is given by an empirical parameter b as follows;

$$P(R) = \left(\frac{R - R_a}{R + \Delta R} \right)^b \qquad (3.4b)$$

Thus Eq.3.9 can be simplified as

$$\lambda_{o-Ps} = \lambda_{TE}(R)\left[1 - \left(\frac{R - R_a}{R + \Delta R}\right)^b\right] + \lambda_T \qquad R \geq R_a \qquad (3.5a)$$

$$= \lambda_{TE}(R) + \lambda_T \qquad R < R_a \qquad (3.5b)$$

Where the best fitting is obtained at the parameter values $R_a = 0.8$ nm, $b = 0.55$ and $\Delta R = 0.166$ nm [10]. $R_{ps} = R_a + \Delta R$ may be considered as a size of *o*-Ps wave packet or an effective *o*-Ps quantum radius. Therefore, for large voids the term λ_T cannot be neglected and as R approaches to infinity all the lifetimes approach the self-annihilation value (142 ns).

However, as we recognized, this model must be fit to data in order to determine *R*a and *b* and, thus, is heavily dependent upon the quality of the data used in the fit. It also has no explicit temperature dependence, and so it must be refit using data acquired in each temperature range of interest. This is a serious deficiency in predictive power because Ps lifetimes are observed to have very significant temperature dependence in porous media [11,12].

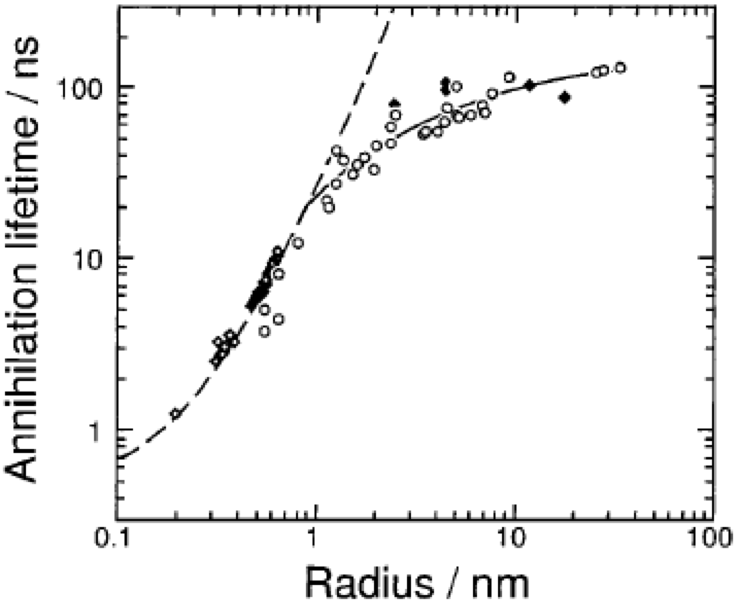

Fig.3.7. The *o*-Ps Lifetimes measured in different porous materials as a function of average pore radius [10]. A solid line shows the correlation curve calculated from the extended Eq. 3.5.

Figure 3.7 shows the average *o*-Ps lifetime measured in various porous materials as a function of the average pore radius. The dashed line is a correlation curve calculated from Eq.3.2 (TE-model). In that case the *o*-Ps lifetimes are clearly overestimated for pore sizes over 1 nm. Whereas the solid line shows the correlation curve calculated according to the extended Eq.3.5 (Tokyo-model), which indicates agreement between the calculated and experimental data for larger pores.

3.3.2. Rectangular Geometry (RTE-Model)

Different attempts have been made to obtain a satisfying description or model for the annihilation lifetime of *o*-Ps trapped in sub-nanometer pores to any average size of the pore and at any temperature [10-18]. Equation 3.2 can not describe the annihilation correctly, because only the 1 s ground state (J_0 = ((sin Ar)/r) of the Ps in the well was considered. At room temperature, this state is basically the only one which is populated in pores (vacancies) with small radii. For larger pores ($R \geq 1.2$ nm)) and or higher temperature excited states have to be considered as well. Therefore, Eq.3.3 cannot lead to correct *o*-Ps decay rates for larger pores at 300 K: Furthermore, larger pores in solids are usually no longer spherical as in Tao-Eldrup model but rather cylindrical, a fact which also has to be considered for the correct calculation of the *o*-Ps decay rates.

In large cylindrical pores with cylindrical radius R and infinite length, cylindrical Bessel function $J_m\ (r)$ have to be used for description of the wave-function of the particle in a cylindrical well. High-order Bessel functions are not very practical in operation due to sever computational difficulties and their use is avoided if possible. In the following, we start our discussion with a simple approach to overcome this problem. In the next chapter we will come back to the more complicated cylindrical or spherical pore model.

A similar model (RTE-model: rectangular extension of the TE-model) to Jasinka et al. [15, 16] was proposed by Gidley et al. [13] to include Ps in pores (wells) of any size at any temperature. Who also assumed rectangular pores to make the calculation of the mean lifetimes (decay rates) of *o*-Ps in these pores more handy compared to the cylindrical model.

The wave-functions of the *o*-Ps in the well are sine functions for that model, which are easy to handle. The wave-functions of particles (*o*-Ps) in a three dimensional rectangular well are calculated as eigenstates of the *x*, *y* and *z* momentum. The solutions of the Schrödinger equation for an infinite rectangular well with side lengths *a*, *b*, and c in *x*, *y*, and *z* direction are given by

$$\Psi_{ijk} = \Phi_i(x).\Phi_j(y).\Phi_k(z)$$

with

$$\Phi_i(x) = \sqrt{\frac{2}{a}}\sin\left(\frac{i\pi x}{a}\right), \quad \Phi_j(y) = \sqrt{\frac{2}{b}}\sin\left(\frac{j\pi y}{b}\right), \quad \Phi_k(y) = \sqrt{\frac{2}{c}}\sin\left(\frac{k\pi z}{c}\right)$$

The energies of these states are given by

$$E_{ijk} = \beta\left(\frac{i^2}{a^2}+\frac{j^2}{b^2}+\frac{k^2}{c^2}\right) \tag{3.6}$$

with $\beta = h^2/16\,\mathrm{m}_e = 0.188\,eV\,\mathrm{nm}^2$ and $m_e =$ mass of the electron (mass of Ps $= 2\,m_e$).

The annihilation rate is assumed to be λ_{T} =1/142 ns in the pore center and λ_a = 2 ns $^{-1}$ within an electron layer of thickness ΔR as in TE-model. The *o*-Ps is assumed to be in thermal equilibrium with the pore such that the states are populated according to a Boltzmann distribution. With this extension of the TE-model, the decay rate of the *o*-Ps in the rectangular pores calculates as follows

$$\lambda(R) = \lambda_a - \frac{\lambda_s - \lambda_T}{4} F(a,\Delta R,T)\,F(b,\Delta R,T)\,F(c,\Delta R,T) \tag{3.7a}$$

$$F(x,\Delta R,T) = 1 - \frac{2\Delta R}{x} + \frac{\sum_{i=1}^{\infty}\frac{1}{i\pi}\sin\left(\frac{2i\pi\Delta R}{x}\right)e^{-\beta i^2/(x^2kT)}}{\sum_{i=1}^{\infty}e^{-\beta i^2/(x^2kT)}} \tag{3.7b}$$

where *T* is the absolute temperature. Gidely et al. [13] renamed the dimensional parameters of the pore and the potential. The potential dimensions are equal to $R + \Delta R$ and extend into the pore walls. For a cubic pore with side a-2 ΔR, the radius $R + \Delta R$ of the spherical model can be related with the cube model by $a = 2\ (R + \Delta R)$. Therefore, Gidley et al. [13] expressed the cubic pore model as a function of the effective pore radius and replaced the cube length *a* by 2 (R+ΔR) to determine ΔR. For that, a value was chosen for ΔR at T = 0 K at which λ (0 K) from the cube model equation (Eq.3.7b, $a = b = c$) was in agreement with $\lambda\,(R)$ from the Tao-Eldrup Eq. 3.2, at a pore radius where the Tao-Eldrup equation is known to be correct (R < 1 nm). By this method ΔR was calculated to be 0.18 nm (for cube) compared with ΔR = 0.166 nm from TE-model(for sphere). It must be remarked again that Gidley et al. denote the dimensions of the infinite potential well with *a*, *b*, and *c*. The pore size is then given by a - $2\Delta R$, b - $2\Delta R$, and c - $2\Delta R$. (unfortunately this denotation differs from the TE-model and also from Eq. 3.9). Figure 3.8 illustrates the Ps density within a pore calculated from the RTE model for a one-dimensional potential well for different quantum numbers $i = n$. The increase in the overlap of the Ps density with electron layer of the pore wall with increasing *n* is clearly seen.

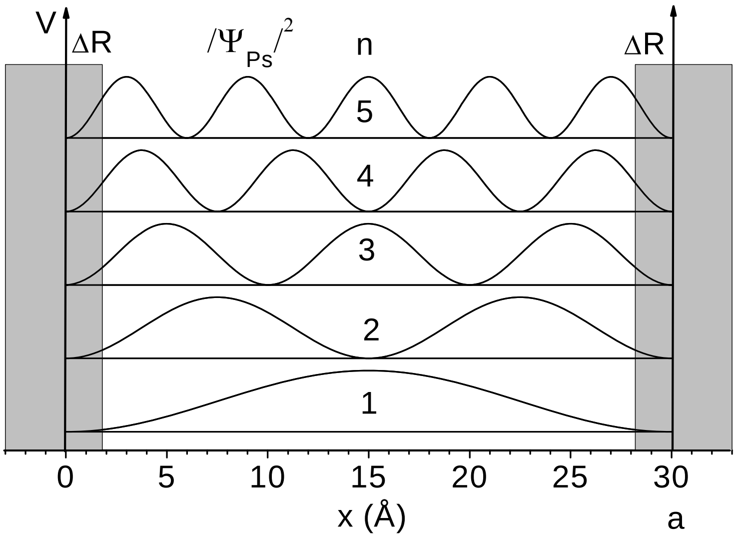

Fig. 3.8. Probability density of Ps, $|\Psi_{Ps}(x)|^2$, localized in an one-dimensional potential well with infinite height and the size a = 30 Å, as example, for the states with the quantum number n = 1…5. $\Psi_{Ps}(x) = (2/a)^{0.5}\sin(n\pi x/a)$ is the Ps wavefunction normalized to $\int|\Psi_{Ps}(x)|^2\,dx = 1$. For clarity, the curves are shifted each to the other. The increasing overlap of $|\Psi_{Ps}(x)|^2$ with the layers $0 \le x \le \Delta R$ and $a - \Delta R \le x \le a$ with increasing quantum number n is clearly seen. The pore size is $a - 2\Delta R$ where ΔR = 0.18 nm.

To demonstrate the relatively weak dependence on detailed pore geometry, the *o*-Ps lifetime calculated with the RTE-model is plotted as a function of the physical pore dimension for 1D sheet, 2D square channels, and 3D cubic pores (sheet spacing, channel width, and cube side length) as shown in Fig. 3.9. As is evident, there is a dependence on the dimensionality of the pores. All the three curves have similar shape but are displaced laterally with respect to each other (As a result of a multiplicative scale factor in pore (potential) length *a*).

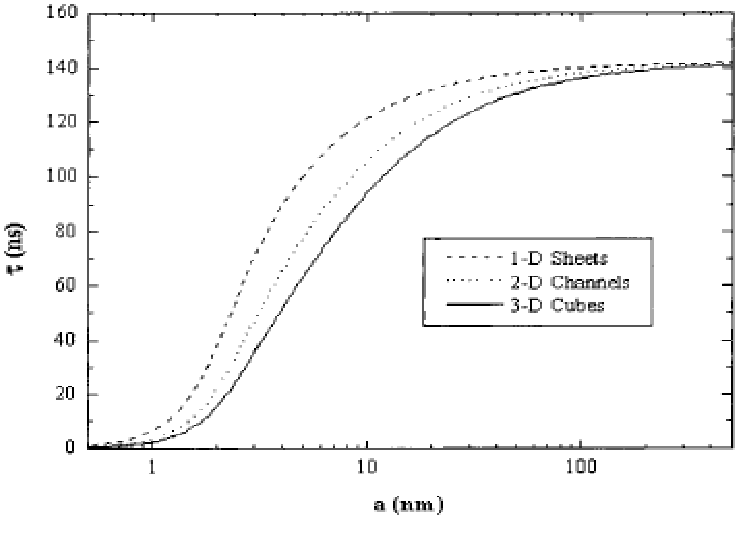

Fig. 3.9. The *o*-Ps lifetimes as a function of pore size for three pore dimensionalities calculated with the RTE-model [13].

The model of Gidley et al. [13] accounts for higher states of the *o*-Ps which are populated according to the temperature and for the pore size dependency of the *o*-Ps decay rate. The RTE-model seems to acceptably fit pores in variety of silica gels data, which were calculated for cubic rectangular well with $a = b = c$ (cubic well) as demonstrated in Fig. 3.10. Adsorbed air in the pores of a sample leads to Ps quenching due to spin conversion. Therefore, some of the data shown in Fig. 3.10 had been corrected by the authors [13]. The sizes of the pores are presented in terms of the mean free path, l, of the *o*-Ps inside the pore wells which accounts for the dependency of the probabilities of a collision of an *o*-Ps with the wall from the number of walls around the *o*-Ps. The mean free path calculated as $l = (2/3)a$ in a cube shaped pore (walls in all three dimensions= closed pore), $l = a$ in a square shaped channel (wells in two dimensions), and $l = 2a$ in a sheet like pores (walls only in one dimensions) [13].

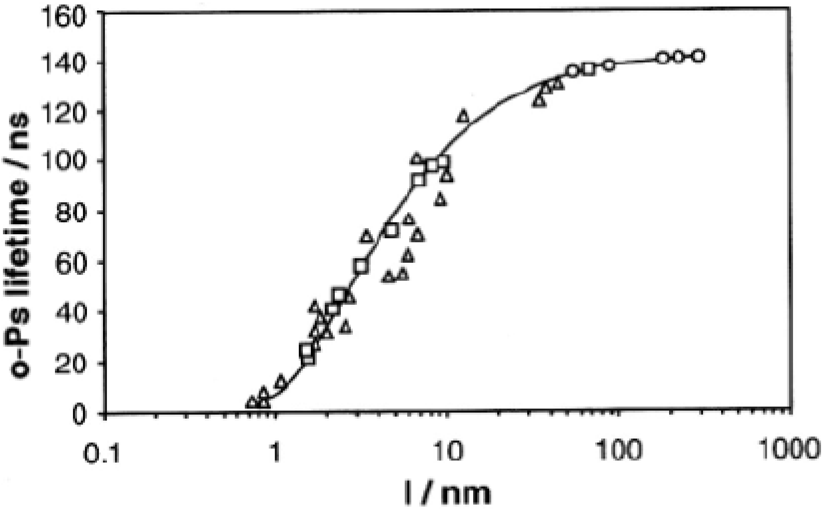

Fig.3.10. Dependency of *o*-Ps lifetimes, measured on different silica gels and calculated for cubic rectangular well with side length a, on the mean free path, l = (2/3) a, of the *o*-Ps (data from [13]).

A similar model but based on cylindrical (or spherical) was proposed by Goworek et al. [16-19] who accounted for higher states of the *o*-Ps by using cylindrical J_m (r) Bessel functions for the calculations. In order to provide a more handy method, they substitute the J_m (r) by linear functions around their node points later on, which is a good a approximation if $\Delta R \leq R$. They found a good correlation between measured and calculated *o*-Ps lifetime on silica-gels, Vycor glass and resins with different pore sizes when accounting also for higher states of the *o*-Ps in a cylindrical well.

3.3.3. Spherical or Cylindrical Geometry

As we referred previously, the TE-model has ignored the possibility of population the excited states in the spherical potential well. This is also reasonable because the energy gap between the ground state and the first excited state, of order 100-200 meV, is large compared to thermal energy kT [13]. Alternatively, one can note that the thermal *o*-Ps de Broglie wavelength, at 300 K is about 6 nm, 1 order of magnitude larger than the subnanometer pore size, and hence, the ground-state zero-point energy is large compared to *kT*.

In the RTE-model, not only the dependency of the *o*-Ps lifetimes on the voids sizes and the shapes were considered, but also the temperature dependency of the lifetime by accounting for higher states of *o*-Ps. As known, with increasing the void size more energy levels appears in the well. Where the spacing of the levels decreases and hence the population of the excited levels cannot be neglected, if the energy of these states is comparable to the thermal equilibrium (*kT*). In such case and for CPGs (or Vycor glass), where the pore sizes distribution is relatively narrow, discrete decay rates have been assumed for each quantum state [18].

Goworek and collaborators extended the TE-model for spherical or cylindrical geometries (called by the authors as ETE– extension of the TE-model). Assuming a Boltzmann population of the Energy states and taking into account the excited states of the *o*-Ps in the potential well, the pick-off rates in spherical or cylindrical pores calculate according to the formula [18,19];

$$\lambda_{po} = \sum_{i=1}^{N} \lambda^{i}_{po}(R)\, g_i \exp\left[-\frac{E_i(R)}{kT}\right] \Big/ \sum_{i=1}^{N} g_i \exp\left[-\frac{E_i(R)}{kT}\right] \tag{3.8}$$

where λ^{i}_{po}, E_i and g_i are the decay rate, the energy of the i-state, the statistical weight of the respective level ($g_i = 2l+1$ for spherical geometry, 2 or 1 for cylindrical geometry) respectively, and N is the number of the levels taken in account. As is observed, the increase of the E_i leads to increasing λ^{i}_{po}, thus the *o*-Ps lifetime will decrease with the rise of temperature. To check the validity of Eq.3.8, it needs a medium with large voids as the porous one. If the pores are of capillary type, the cylindrical potential well should apply, instead of the spherical one as in Eq. 3.2. By the extension of TE-model, the pick-off decay rate λ^{ni}_{po} for *o*-Ps occupying the level *nl* for spherical geometry;

$$\lambda^{nl}_{po} = \lambda_a \int_{x_{nl}R/R_o}^{x_{nl}} J_l^2(r)\, r^2\, dr \Big/ \int_{0}^{x_{nl}} J_l^2(r)\, r^2\, dr \tag{3.9a}$$

While for infinitely cylinders geometry (capillaries)

$$\lambda^{nm}_{po} = \lambda_a \int_{x_{nm}R/R_o}^{x_{nm}} J_m^2(r)\, r^2\, dr \Big/ \int_{0}^{x_{nm}} J_m^2(r)\, r^2\, dr \tag{3.9b}$$

where χ_{nl} is the nodes of the Bessel function J_l for spherical voids and χ_{nm} is for cylindrical ones (J_m) and $R_0 = R + \Delta R$. Calculation of the integrals in Eq. 3.9b then gives

$$\lambda_{po}^{nm} = \lambda_a \left[1 - \left(\frac{R}{R_0} \right) \frac{2J_m^2\left(\frac{\chi_{nm} R}{R_0} \right) - \frac{2nR_0}{\chi_{nm}} J_m\left(\frac{\chi_{nm} R}{R_0} \right) J_{m+1}\left(\frac{\chi_{nm} R}{R_0} \right) + J_{m+1}^2\left(\frac{\chi_{nm} R}{R_0} \right)}{J_{m+1}^2\left(\chi_{nm} \right)} \right] \qquad (3.9c)$$

For cylindrical pore, if $\Delta R \le R$ the J_m Bessel functions in the numerator can be substituted by linear approximations. For $R \ge 2nm$, the deviation between exact and approximated values is less than 5 % [18]. With this approximation the $\lambda_{po}^{(i)}$ for the lowest states $\left(n = 1, m = 0, \pm 1, \pm 2....etc. \right)$ calculate as fellows [18]

$$\lambda_{po}^{(1,0)} = 3.85\,\lambda_a \left(\frac{\Delta R}{R_0} \right)^3 \left(1 - \frac{3\Delta R}{4R_0} \right) \qquad (3.9d)$$

$$\lambda_{po}^{(1,\pm 1)} = 9.75\,\lambda_a \left(\frac{\Delta R}{R_0} \right)^3 \left(1 - \frac{3\Delta R}{4R_0} \right) \qquad (3.9e)$$

$$\lambda_{po}^{(1,\pm 2)} = 17.4\,\lambda_a \left(\frac{\Delta R}{R_0} \right)^3 \left(1 - \frac{3\Delta R}{4R_0} \right) \qquad (3.9f)$$

etc., the energies E_i calculated according to

$$E_{n,l} = \frac{h^2}{8\pi m_{ps}} \frac{X_{nl}^2}{\left(R_0 \right)^2} \text{.................(sperical well)} \qquad (3.10a)$$

$$E_{n,l} = \frac{h^2}{8\pi m_{ps}} \frac{X_{nm}^2}{\left(R_0 \right)^2} + E_{\parallel} \text{.........(infinitely long cylinderical well)} \qquad (3.10b)$$

with h, the Planck constant, and $E_{\parallel}$, the energy related to the motion along the cylindrical, which is not quantized (average energy $E_{\parallel} = kT/2$) [16, 18]. Only the quantized part of the energy for cylindrical pore geometry in Eq. 3.10b has to be considered because $E_{\parallel}$ adds a constant value to exponents in Eq. 3.8, but does not effect the relative population of the states. Goworek et. al. [18] found the best fit with the experimental data (silica gels and Vycor glasses) assuming $\Delta R = 0.19\,nm$ for cylindrical pores, which is slightly larger than the value used by Gidley et. al. of $\Delta R = 0.18\,nm$.

3.3.4. Temperature Dependence in Porous Media

The temperature dependency of the *o*-Ps lifetime can be easily calculated in the RTE model. Figure 3.11 shows the theoretical RTE curves for different temperatures [11, 13]. For clarity, only cubic pore calculations are presented and the mean free path *l* is determined from the cube side-length. In fact, the TE and the RTE curves at T= 0 K are in agreement over the primarily size range (subnanometer regime). That is equivalent to saying that the TE-model involves only the ground state in the potential well (cavity). Although the RTE-model agrees with data in both the TE (subnanometer) and classical large-pore regimes, it is important to test its validity in the intermediate pore-size regime.

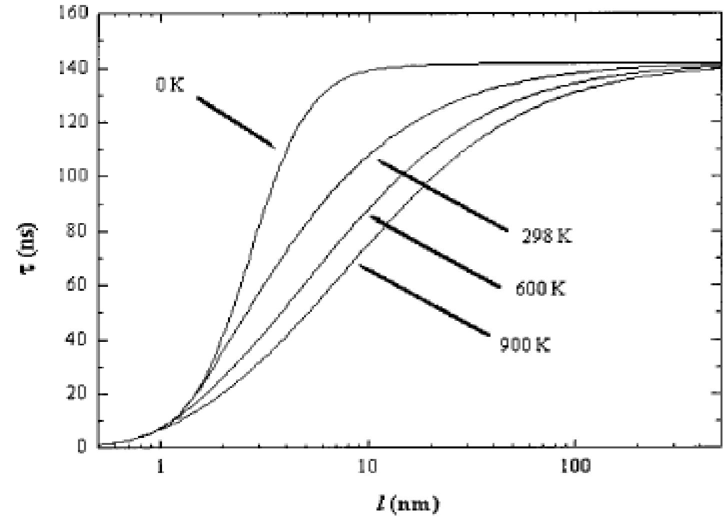

Fig. 3.11. The theoretical *T*-dependence of the Ps lifetime vs the mean free path *l* for cubical pores in the RTE model. The mean free path of Ps, *l*, is related to the cube side length of the potential by $l = 2/3a$ [13].

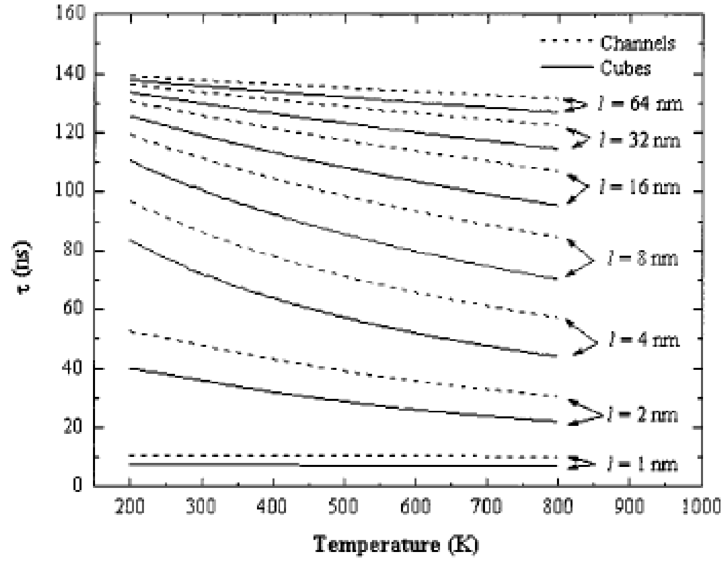

Fig. 3.12. The *o*-Ps lifetime vs temperature for a variety of mean free paths *l* using both 2*D* and 3*D* pores in the calculation [13].

Figure 3.12. represents the calculated *T*-dependence of the *o*-Ps lifetime for a different of pore sizes in the form of channels (2D) and cubic (3D) geometries [13]. These pore sizes were measured in terms of the *o*-Ps mean free path *l*. There is a slight *T*-dependence for small pores as expected from the TE-model, moreover, the 2D and the 3D curves agree quite well for small and large pores. However, there is no significant *T*-dependence on pore geometry for intermediate sized pores. The dependence becomes more significant at higher temperature.

Figure 3.13. shows the *o*-Ps lifetime data collected in a highly interconnected porous silica film (rather than a distribution of closed pores) at various temperatures [13]. Three RTE (cubic) temperature curves are also plotted for comparison. The highly interconnected pores lead to a significant single Ps lifetime, which will correspond to the average mean free path (*l*) of Ps interacting with the total void volume.

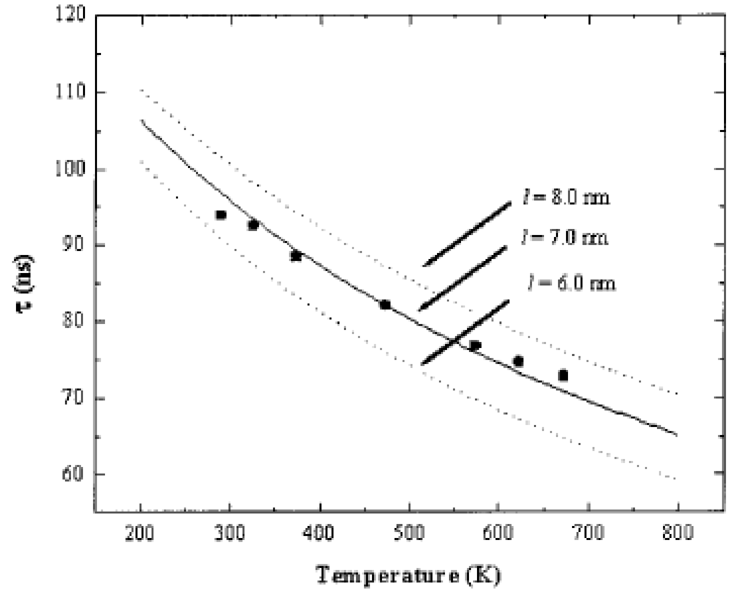

Fig. 3.13. The *o*-Ps lifetimes measured in a low-K porous silica film as a function of temperature and the RTE calculated curves for different *o*-Ps mean free path *l* [13].

To confirm that *o*-Ps has approached thermal equilibrium, this lifetime spectrum is fitted beginning at 50 ns after time zero in the lifetime spectrum. As can be seen, the solid l = 7.0 nm curve fits the data quite well. The two dotted curves are plotted to demonstrate the sensitivity of the technique. Similarly good fits are also obtained using 2D channels for the pore model. Other *T*-dependent results have been observed [12, 18] and they appear to be in agreement with the RTE expectation.

3.4. Determination of Surface Area by PALS

The formation of *o*-Ps within the pores of a solid is limited to the pore surface. Hence the larger the surface area of these pores, the more *o*-Ps may be formed in these pores. The number of *o*-Ps, which is expressed by the intensity of respective component of the lifetime spectrum is thus the function of the surface area of the pores. The fraction of *o*-Ps annihilating in the bulk and on the surface of the material can be calculated by a relation proposed by Brandt and Paulin [27] which was slightly modified by Venkateswaran [28], who proved this equation to be correct with their data;

$$\frac{I_3}{I_3 + I_4} = 1 - (3/2)\beta\left[1 - \beta^2 + (1 + \beta^2)\exp\left(-2/\beta\right)\right] \tag{3.11a}$$

with

$$\beta = \frac{A_{sp}\rho(D\tau_p)^{1/2}}{3.0} \tag{3.11b}$$

Where ρ and τ_p are the density and lifetime of bulk material respectively, D is the diffusion coefficient of *o*-Ps in the media, and A_{sp} is the specific surface area. Porous material spectra consist usually of more than 3 components, therefore, in Eq. 2.12 the intensity of two long lifetime components have been included. The first one I_3 is related to *o*-Ps annihilation in smaller pores in the bulk, and the second I_4 assigned to the longest-lived *o*-Ps component, which is related to annihilation on the surface of large pores.

4.1. The Positron Sources

More than 300 positron-emitting nuclides are known, of which about a dozen can be used as sources in positron annihilation experiments [1]. The relevant properties of a positron emitting nuclide are the positron yield, end point energy, half-life and ease of production with available price. The importance of the positron yield is trivial. The end point energy is important in two respects, the first being the positron penetration in the sample (Eq.4.2) and the second the percentage of positrons annihilating in the source.

$$x = \frac{1}{\mu^{+}} \ln \frac{I(0)}{I(x)} \tag{4.2}$$

where x is the penetration distance in the sample, μ^{+} is the absorption coefficient, I (0) is the initial positron density, and $I(x)$ is the positron density at x after a beam of positron of initial density $I(0)$ traversed a thickness x of a given sample.

One can thus expect, by virtue of both the end-point energies, that the most energetic positron can penetrate the sample to a depth of about 1 mm, although some positrons will stop or return and annihilate at or near the surface of the sample. Half-life of the nuclide should be large enough to be able to perform a series of measurements with the same source. There is, however, no need for a half-life larger than a few years. The energy of the start gamma should be significantly higher than that of the annihilation gamma's to make recognition easy and to prevent spectrum distortion. Tab. 4.1 lists some of the relevant properties for the commonly used isotopes by Brown [2].

Isotope	End-point energy (MeV)	Half-life	Positrons per decay
^{22}Na	0.54	2.6 y	0.90
^{58}Co	0.47	71 d	0.15
^{44}Ti	1.47	47 y	0.94
^{64}Cu	0.66	12.7 h	0.19
^{68}Ge	1.90	257 d	0.86
^{57}Ni	0.85	36 h	0.19
^{90}Nb	1.50	14.6 h	0.54
^{55}Co	1.50	18.2 h	0.81

Tab. 4.1. Commonly used positron-emitting isotopes.

For lifetime or Doppler measurements, the simplest way to guide the positrons into the samples is to use a sandwich configuration as shown in Fig.4.1. The source has to be very thin so that only small fractions of the positrons annihilate in the source. Radioactive material can be deposited directly on the samples or separation foils can be used to allow using the source repeatedly. The source can also consist of a single radioactive metal foil. Figure 4.2 demonstrates the experimental arrangements of the positron source and the samples with respect to the lifetime system.

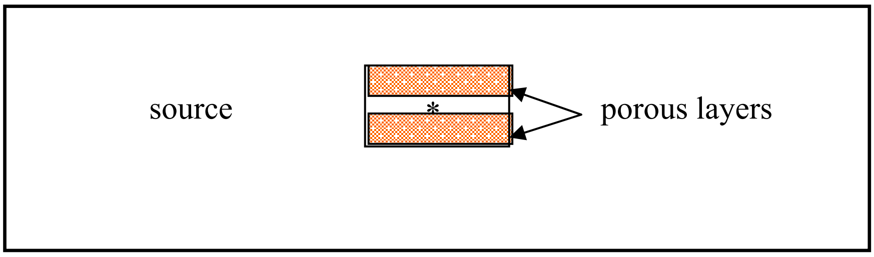

Fig. 4.1 Sandwich configuration of the source together with two layers of the specimen.

In our experiment the radioactive isotope used is ^{22}Na. The decay scheme of ^{22}Na is shown in Fig. 1.3. First of all, the appearance of a 1.27-MeV γ-quantum almost simultaneously with the positron enables positron lifetime measurement by a start–stop coincidence spectrometer.

Sources of different activities (3, 4.5, 5.8, 7, 10, 13 μCi) were used to carry out the measurements according to our MontoCarlo simulation (see chapter 5) for the determination of the suitable source activity (see the results chapter).

4.1.1 Source Corrections

The amount of positrons annihilating in the source (12-17 %) is related to the geometry of the sandwich configuration, the thickness and density of the foil included, and of specific samples which are measured. In some cases, the samples enter into this consideration because the positron may be reflected at the sample-source interface. These annihilations contribute additional lifetime components to the lifetime spectrum (source spectrum). In order to obtain reliable values of lifetimes and their intensities in studied samples, a precise correction (subtraction) of these components is important. Any corrections should be measured using defect-free reference samples with well known spectra. An empirical formula to the foil intensity has been given as [3]:

$$I_{\text{foil}}\,(\%) = 0.324 \times Z^{0.93} \times D^{3.45/Z^{0.41}} \tag{4.3}$$

where Z is the sample atomic number and D is the foil thickness in [mg/cm^2]. At high Z values (> 40) this formula overestimates the foil intensities.

4.2. Experimental Techniques

4.2.1. Fast–Fast Lifetime Spectrometer

As illustrated in Fig.1.3, the lifetime can be measured by measuring the difference in the time between the appearance of γ-ray from the source (1.274 MeV) and one of the annihilation quanta (0.511 MeV). The fast-fast lifetime spectrometer used in this work consists of two branches as shown in Fig.4.2. These branches consist of two plastic detectors, two Hamamatsu photomultiplier tubes (H3378-50), two constant fraction discriminators (CFDs) Ortec (583) and Canbera (729), a time to amplitude converter (TAC) Ortec (566), and multi-channel analyzer (MCA) Ortec (919). One of these branches used to focus the detectors on the 1.274 MeV quanta and the other on the annihilation quanta 0.511 MeV by using the CFDs. Each constant fraction discriminators generates the timing information and determines the energy range of interest simultaneously. The two CFDs provide the start and stop signals for the TAC. Either the birth or the annihilation of γ-ray may be used as a start signal with the other is being used as the corresponding stop. The TAC transforms the time difference between the start signal and the stop signal from the annihilation quantum into amplitude signal (voltage) proportional to the time difference between the 2γ-rays. The signal from the TAC is fed to the MCA for sorting storage.

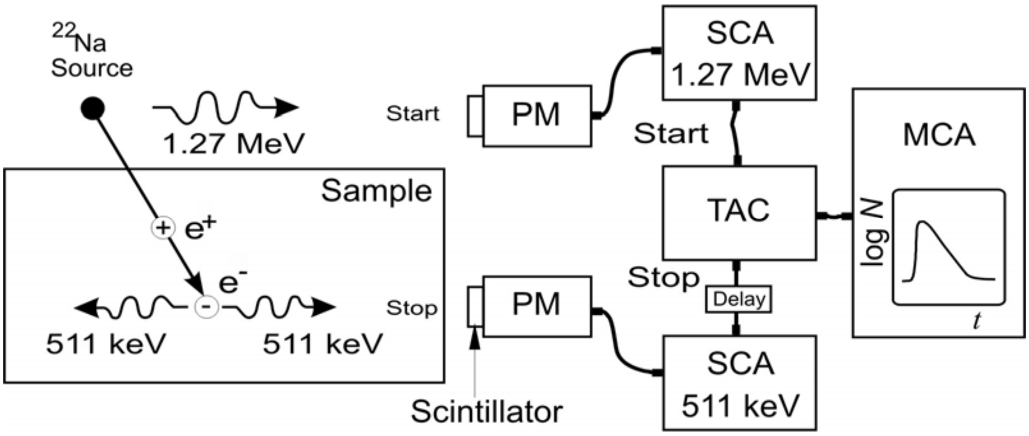

Fig. 4.2. Schematic diagram shows the fast-fast coincidence lifetime spectrometer.

In measurements of positron lifetimes the most frequently three common systematic timing errors, come from:

1. The walk due to the different pulse heights
2. The ambient temperature variation
3. The count rate variation

The first timing error can be reduced by using CFD. The drifts due to the temperature variation are reduced by using a reliable air condition system. The third source of errors, change with count rate variation, can be simply avoided by keeping the count rate sufficiently low or by rejecting pulses which are too close to each other.

4.2.1.1. Details of Time Spectrometers

A- Scintillators:

The use of scintillation capable materials is one of the oldest known methods of detecting and measuring ionising radiation. Despite its age, scintillation is still one of the most useful techniques for carrying out spectroscopy on nearly all types of radiation. These detectors may be either inorganic crystals or organic compounds, which emit light flashes or scintillation's when charged particles, X-ray or γ-rays pass though them. All inorganic scintillators rely on the crystalline nature of the material for light production and most have impurity atoms, with ionization potentials less than the atoms of the crystal, added as activators. The ideal scintillation material should possess the following properties:

1. It should convert the kinetic energy of charged particles into detectable light with a high scintillation efficiency.
2. This conversion should be linear-height yield and proportional to deposited energy over a wide range.
3. The medium should be transparent to the wavelength of its own emission for quality light collection.
4. The decay time of the induced luminescence should be short so that fast signal pulses can be generated.
5. The material should be of good optical quality and subject to manufacture in sizes large enough to be of interest as a practical detector.
6. The index of refraction should be near that of glass (~1.5) to permit efficient coupling of the scintillation light to a photomultiplier tube.

No material simultaneously meets all these criteria, and the choice of a particular scintillator is always a compromise among these and other factors. The intended application has a major influence on scintillator choice.

B- Scintillators and Light Collection

When ionizing radiation or energetic particle enters a scintillation material, some or all of its energy is transferred into the material and is partly re-emitted as electromagnetic energy (photons) within the visible light and may sometimes extend into the UV energy. A scintillator showing such energy levels (optical levels) are responsible of this transformation and can be easy excited by energetic particles or light quanta. The excitation takes place in a few steps. In the energy range of the γ-quanta of interest, energy is transformed from the primary γ-quanta to electrons in the valence band mainly by the Compton Effect. Then electrons are excited from the valence band to the conduction band of the crystal. In the conduction band these energetic electrons excite optical levels of a large number of atoms, while holes left in the valence band may also move and ionize a host atom that it encounters. The impurity ions introduce trapping levels in the energy gap between the valence and conduction bands. In brief, electrons may move into an excited level of the activator ion and then drop to the ground energy state with the emission of light. On decay, optical photons are produced. If the excitation process is short with regard to the decay time, the shape of the light pulse may be given by the function

$$I(t)=\left(\frac{I(0)}{\tau_{sci}}\right)\exp^{-\frac{t}{\tau_{sci}}} \qquad (4.6)$$

where I (0) and τ_{sci} are the light yield and the decay time of the scintillator respectively. Before arrival at the photocathode, the light pulses may have been reflected several times at the surface of the scintillator. Thus the measured values of the decay constant and specially the risetimes of the light pulses depend on the surface conditions and the dimensions of the scintillator. Small scintillators sometimes are painted black on the outside to yield the lowest values for the rise and decay times.

Scintillation detectors for beta radiation are often organic scintillators. Organic scintillators operate at the molecular level, which means that the light emission occurs as a result of fluorescence as a molecule relaxes from an excited level following excitation by energy absorption from ionizing radiation. Most commonly used organic scintillators are plastic and liquid detectors.

There exists a rather large number of inorganic crystalline scintillators; some examples of these include sodium iodide activated with thallium, NaI(Tl), cesium iodide activated with thallium, CsI(Tl), bismuth germinate, $Bi_4Ge_3O_{12}$, and barium fluoride, BaF_2. Most have been used for gamma measurements but some have been prepared with thin windows and have been used for charged particle (e.g., alpha and beta) counting.

C- Plastic and Barium Fluoride (BaF_2) Scintillators

If organic scintillators are dissolved in a solvent, which can be subsequently polymerized, the equivalent of a solid solution can be produced. The most common example is a solvent consisting of styrene monomer in which an appropriate organic scintillator is dissolved. The styrene is then polymerized to form a solid plastic scintillator. Plastic scintillators were first developed in 1950 by Hurlbut [3] to replace the expensive organic crystals, such as anthracence, and to extend liquid scintillator technology to the solid phase. In comparison with NaI, the plastic scintillators have much faster light pulse decay and therefore they can be used in fast timing experiment.

Barium Fluoride is an inorganic scintillator with a high atomic number (Z=56) and a density of 4.88 g/cm^3. This means BaF_2 has high detection efficiency with a fast response time. The scintillation light from BaF_2 has two components, one 'fast' and the other 'slow'. The decay time for the 'fast component' emitted in the short wavelength region of the spectrum (220 nm) is only 0.6-0.8 ns. However the 'slow component' in the longer wavelengths (310 nm) has a much longer decay time of 630ns [4]. The 'fast component' is within the ultraviolet region of the spectrum and is therefore difficult to detect with most PMTs. In order to detect the short wavelength the PMT requires the use of a quartz end window tube or some other non-standard light detector [5]. The purpose of using two BaF2 detectors together in a coincidence arrangement is to allow the measurement of lifetimes down to the sub-nanosecond scale. In order to do this, the BaF2 detector will have to be characterised in terms of its energy resolution and efficiency.

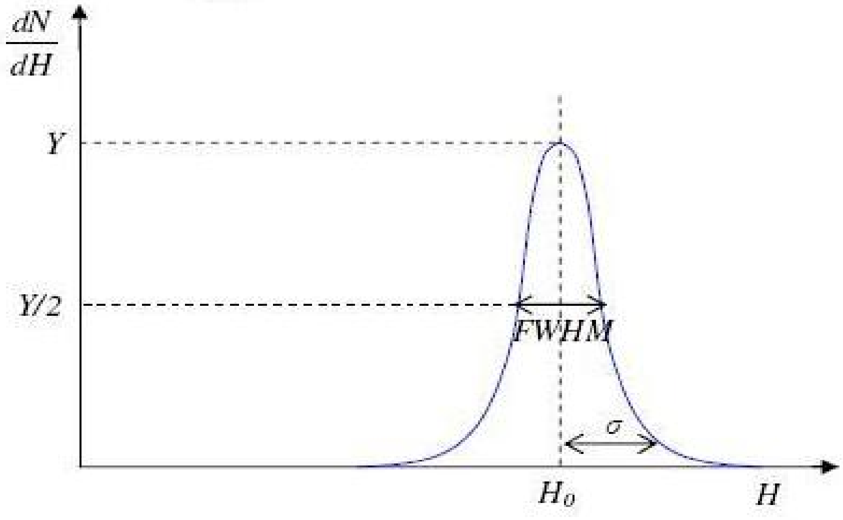

Fig.4.3 Definition of detector resolution function (FWHM).

The three most important properties of a scintillator are efficiency, energy resolution and decay time.

(I) Energy resolution: A detector's ability to resolve the small differences in the energy of incident photons is referred to as its energy resolution (E_R). The smaller the energy resolution the better a detector is able to distinguish between two photons of similar energy. The peaks on a spectrum all have a finite width. From this the full width half maximum (FWHM) can be determined.

Energy resolution as a percentage can therefore be found by

$$E_R = \frac{FWHM}{H_0} \times 100 \tag{4.4}$$

where FWHM and H_0 are both expressed in terms of channel number. It is important to note that energy resolution not only varies for different detectors but also at different incident radiation energies. Energy resolution can also be affected by such things as electrical noise, drift and fluctuations in the baseline voltage supplied to the detector [4].

(II) Detector efficiency: In principle all radiation detectors will produce an output pulse for every quantum of radiation that interacts with the detector's volume. However, uncharged γ-rays can travel a significant distance through a material before interacting. Therefore, due to the large distance between interactions it is normal for γ-ray detectors to be less than 100% efficient. A precise figure for detector efficiency can be calculated in two ways. The first is an absolute value defined as

$$E_{\text{int}} = \frac{\text{number of pulses recorded}}{\text{Number of radiation quanta incident on detector}} \qquad (4.5)$$

(III) Decay time: The decay time characterises the prompt scintillation yield of a material and its time of recovery before the material returns to its unexcited state and can undergo another scintillation event [6].

In a detector the emitted photons of light are most often measured with a photomultiplier tube (PMT) that converts the light to an electronic pulse. Within the PMT a series of cascade reactions occur increasing the intensity of the light pulse, which is then finally converted into an electrical pulse at the anode.

D- Photomultiplier Tube (PMT)

The photomultiplier tube (PMT) is an integral part of a scintillation counter. The photomultiplier is essentially a fast amplifier, which in times of 10^{-9} s amplifies an incident pulse of visible light into primary photoelectrons by a factor of 10^6 or more. A photomultiplier consists of an evacuated glass tube with a photocathode at its entrance and an electron multiplication system as shown in Fig.4.4.

Two types of multiplication system can be distinguished:

1. The first type is the staged multiplication system. It contains a system of positively charged dynodes. The photons produced in the scintillator enter the phototube and hit the photocathode, which is made of material that emits electrons when light strikes it. The electrons emitted by the photocathode are guided, with the help of an electric field, towards the first dynode, which is coated with a substance that emits secondary electrons, if electrons impinge upon it. The secondary electrons from the first dynode are guided towards the second, from there towards the third, and so on by applying a successively increasing positive high voltage to each dynode.

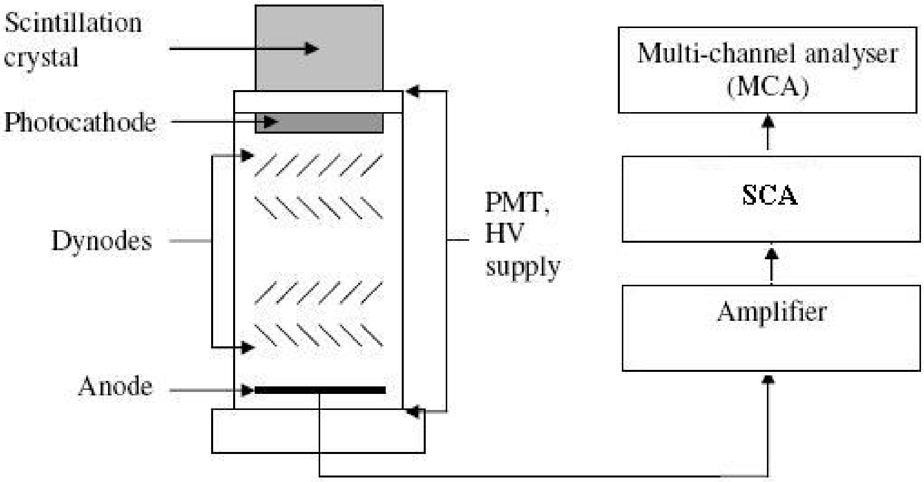

Fig.4.4. Schematic digaram of the scinatillation detector, photomultiplier tube (PMT) and the experimental arrangement of the γ-ray spectroscopy.

2. The second type is the channel plate photomultiplier, that a channel plate contains a huge amount of tiny channels. Electrons diffuse through the channels by means of an almost parallel electric field. The current is amplified because the electrons hit the wall of the channel and cause secondary emission. The amplified electron current is collected at an anode in both types of photomultipliers.

The photocathode material used in most commercial phototube is a compound of cesium and antimony. The material used to coat the dynodes is either Cs-Sb or silver- magnesium. The secondary emissions rate of the dynode depends not only on the type of surface but also on the voltage applied. A very important parameter of every photomultiplier tube is the spectral sensitivity of its photocathode.

4.2.2. Doppler Broadening Spectroscopy (DBS)

The Doppler effect is the apparent change in the observed frequency of a wave as a result of the relative motion between the source and the observer. This effect was suggested by Doppler (1883-1855), an Austrian physicist, as an attempt to explain the coloration of stars. The system which has been used in the present work to determine the Doppler broadening S and W parameters, consists of an Ortec HPGe detector, with an energy resolution of 1.5 keV for the 511 keV line of ^{22}Na, an Ortec 5kV bias supply (659) Ortec amplifier (672), and Ortec MCA model 919. Figure 4.5, shows a block diagram of such an apparatus.

Doppler broadening is caused by the distribution of the velocity of the annihilating electrons in the directions of the gamma ray emission. The signal coming from the detector enters the input of a preamplifier and the output from the preamplifier is fed to amplifier.

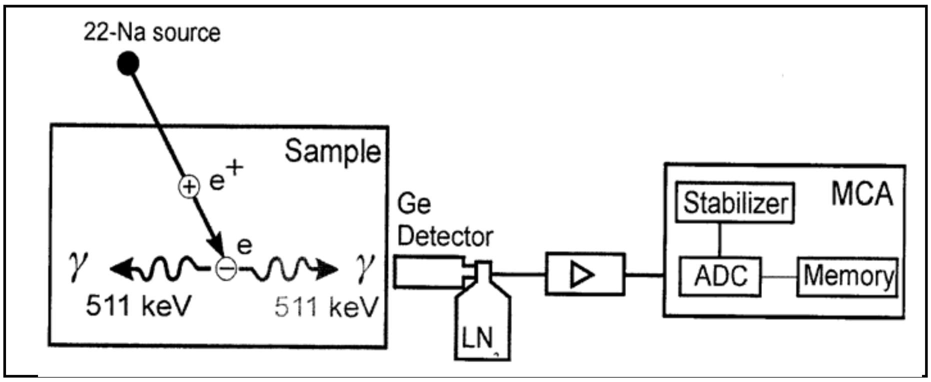

Fig.4.5. Block diagram of HPGe-detector and electronics for Doppler broadening line shape studies.

The input signal is a negative charge. The output signal from the amplifier is fed to the input of an ADC to be digitized. Then the signal passes to the MCA that transfers the data to the computer system.

4.3. Vacuum and Cryo-Condensation System

I did some modifications of one of our vacuum systems and I was redesigning another vacuum system for the characterization and studying the capillary condensation effect in CPG by using PAS. In September 2004, we began improving the vacuum of the system to achieve ultrahigh vacuum (UHV) in order of 10^{-8} mbar, such pressure is important to probing porous glass materials. In April 2005, we began rebuilding a new vacuum system from a stainless steel vacuum chamber body as well we have added another inner gas room for studying the capillary phenomenon. The main body of the vacuum chamber is designed to achieve UHV with a base pressure < 10^{-10} mbar while the inner part is designed to 10^{-5} mbar gas pressure. Both of the two systems are connected to a pre-vacuum pump (10^{-3} mbar) which can manually control the pre-vacuum of system to avoid loosing powdered glass from the sample holder. Several changes were made for the final design of the vacuum system as shown in Fig. 4.6.

In order to understand the design of our system, some basic definitions are given below;

(1) Flange connects the head of the compressor to the vacuum system
(2) Conflate Flange (CF)
(3) First stage cryoarray
(4) Second stage cryoarray
(5) Second stage temperature monitor
(6) Thermal fuse
(7) Sapphire
(8) Heating coil
(9) Sample temperature monitor
(10) Sample holder
(11) Sample cell
(12) The cape of the main chamber
(13) The cape of the inner chamber
(14) Bias of the holder
(15) Inner chamber
(16) Gas tube

(17) Chamber port (18) Turbo pump port

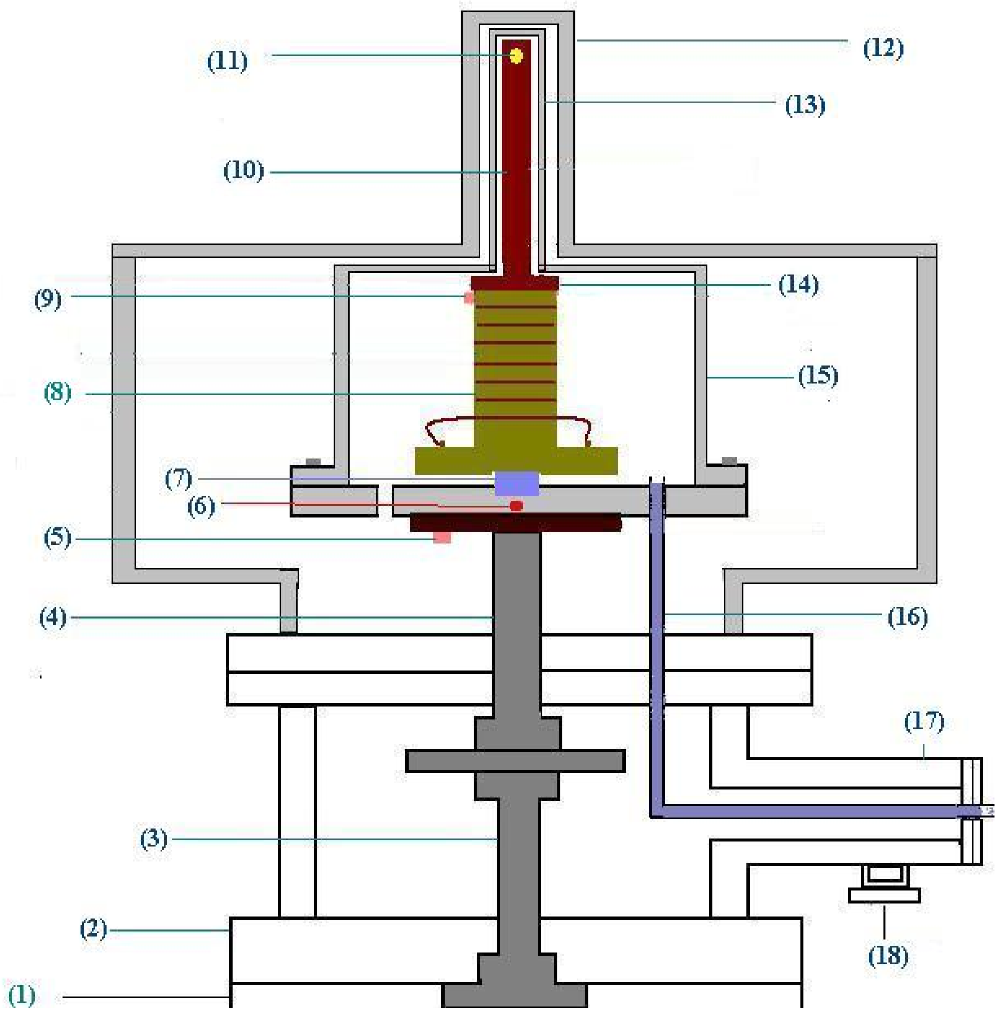

Fig.4.6. Schematic view of shows the different components of our UHV system.

4.3.1 Achieving Ultrahigh Vacuum (UHV)

There is about 3×10^{19} molecules/cm^3 at atmospheric pressure (1.0132 10^{-3} mbar). In UHV this would be reduced by ~12 orders of magnitude or to 3×10^{7} molecules/cm^3. However, to achieve UHV requires much care and planning. The major issues involved with achieving UHV will be listed in this section.

The measurements of CPG in the form of powders were performed inside a cylindrical cupper cell (11) with free access to the external chamber. The bias of the sample holder (14) is fixed on the top of the heating coil (8) which is associated, automated and computer controlled specimen (heating and cooling). To seal the chamber from atmosphere, we are using metal-to-metal seals such as using conflate flanges (2) and copper gaskets because of the UHV tight seal that conflates provide. Any components used inside the UHV part of the vacuum system should be made exclusively of materials (such as aluminium, and stainless steel) with low outgas rates that are safe for vacuum usage. This includes all the metal components such as bolts, nuts, and washers. All surface areas are sources of outgassing. The surface area of all the components should be minimized.

Three types of pumps are used in our chamber- roughing pump, turbo molecular pump, and a cryo-pump. The operation of these pumps rely on two main principles: roughing pump is used to bring the chamber from atmospheric pressure to roughing pressure (1×10^{-3} mbar). The turbo pump then takes the chamber down to UHV pressure, while the cryopump is to use cold traps, by which the material or components inside the chambers are cooled to very low temperatures to attract the gas from the relatively hot chamber. The cryo-pumps of our system go down to liquid nitrogen temperatures (~40 K). The turbo molecular and the cryo-pumps will be described briefly in the next section.

(I) Turbo molecular Pump

Turbo molecular pumps are very clean mechanical compression pumps that can reach pressures of $<1\times10^{-9}$ mbar. They pump by using a high-speed rotating surface to give momentum and direction to gas molecules. The turbo pump is mainly composed of rotating and fixed desks which are called rotors and stators as shown in Fig. 4.7. The rotor desks and are arranged alternately with the stator desks.

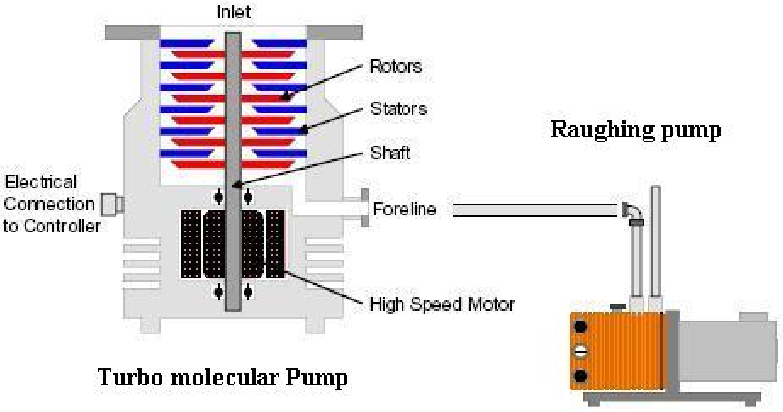

Fig. 4.7. Schematic draw shows the turbo molecular and roughing pumps.

Turbo pumps can not exhaust directly to atmosphere but compressed gases are expelled from the pump by some type of roughing pump. The inner gas chamber is connected to the roughing pump by the gas tube (16) which is also used to let the gas in and out of the chamber. The gas pressure is controlled by a manual valve which is mounted to analogue manometer (1 bar maximum).

(II) Cryopump

The cryopump is unique in that it pumps by getting gases so cold that they freeze out and are stored, or captured, in the pump. The cryopump that is installed in our vacuum system is made by CTI-Cryogenics. The pump consists of the following major components: the expander module, the first stage (3) and second stage cryoarrays (4), the pump body, and the second stage temperature monitor (5). The expander is where refrigeration is produced. High-pressure nitrogen gas is supplied by the compressor unit (model 8200) to the cold head through the flexible pressure lines in a closed cycle. This gas is expanded in two stages to produce cryogenic temperatures.

The actual operation temperatures of the two stages will vary, depending on thermal and gas loads that are imposed. Typically, the first stage operates between 50 and 80 K, and the second stage, or cold head, between 20 and 30 K. The cryo-arrays are the pumping surfaces which are cooled by the expander. It is on these cryo-arrays that gases from the vacuum chamber are condensed or adsorbed. The pump body forms the vacuum tight envelope, which attaches the pump to the vacuum chamber. In cryocondensation most gases will stick to a surface in an ice like condition at less than 30 K is quite high. At this temperature, the combination of partial pressures of most gases is around 10^{11} mbar or lower. Most gases are condensed on the first- and second stage cryoarrays. The first stage array is cold enough to pump water vapour by cryocondensation. The second stage array is cold enough to pump nitrogen, oxygen, argon and most other gases by cryocondensation [8].

4.3.2 Thermocouple Monitoring

Two K-type thermocouple temperature monitors have been mounted on our vacuum chamber. A thermocouple is mounted on the top of the head of the second cooling stage and another one is mounted on the top of the heating coil to probe the sample temperature ((5) and (15) in Fig.4.6 respectively). The thermocouple temperatures have been read by using a computer controlled unit from Eurotherm (model 818). Even after more than a year of designing and building by our group, there remain improvements to our system, as well as additional vacuum components to be installed. However, we have been able to construct a working vacuum system with all the basic and necessary components for in situ capillary condensation measurements. Chamber walls, screws, any parts, and any material inside the chamber are sources of outgassing. In order to facilitate quick degassing of these components, baking out the chamber to temperatures as high as the system can handle.

5.1. The Preparation of the Specimens for Measurements

In our measurements we used CPG in the form of powder and membranes samples with a pore size of 1 to 64 nm. The given pore sizes were determined by adsorption technique and supplied by the institute of technical and macromolecules chemistry in Martin-Luther university at Halle/Saale. The measurements of powder samples were performed inside a cylindrical cupper cell with a volume of 95 mm^3 having free access to the external chamber for evacuation. The bias sample holder is fixed on the top of the heating coil which is an associated, automated and computer controlled specimen (cooling and heating). Two layers of porous powder sandwiched the source in such a fashion each layer is thick enough to contain almost all the positrons. For membrane samples we used a different holder such that the samples are exposed directly to the vacuum process (see the appendix chapter for more information about the samples).

5.2. PALS Experiments and Data Analysis

5.2.1. Window Setting and System Calibration

In the positron laboratory of Martin Luther University at Halle there are three conventional fast-fast positron lifetime spectrometers [1]. The difference between these three spectrometers is based on the types of scintillators and the coupled photomultiplier tubes (PMTs). In one of the spectrometers the γ-quanta are registered by using two plastic scintillation detectors coupled to Philips XP2020 PMTs. The other spectrometers have Hamamatsu H243-50 PMTs either coupled to BaF$_2$ detectors or plastic scintillation detectors.

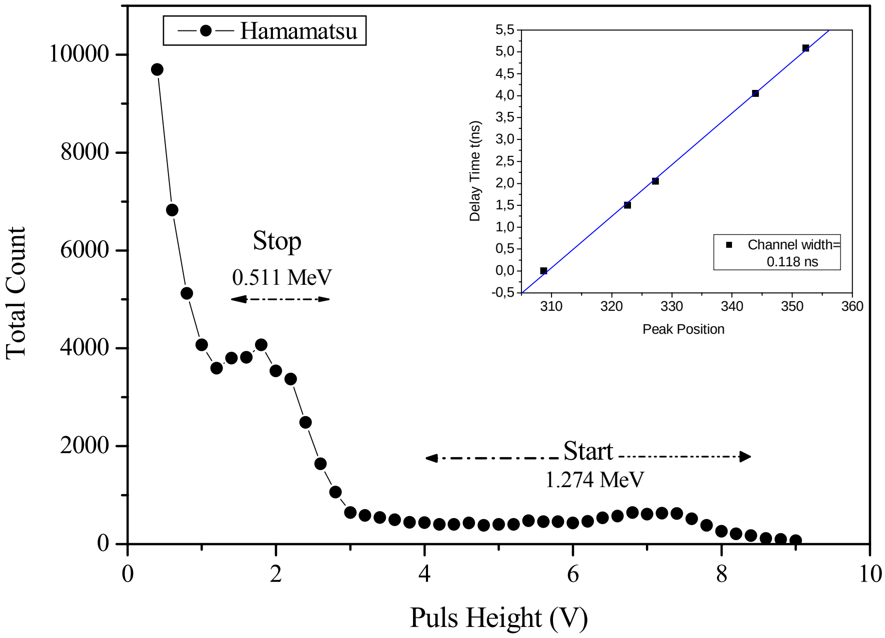

Fig. 5.1. Energy spectrum of ^{22}Na recorded with plastic scintillator and Hamamatsu PMT. The inset figure represents the linear fit for the delay time and the peak position to estimate the time scale of the system

Figure 5.1 represents the part of the spectrum of ^{22}Na recorded with plastic scintillators and Hamamatsu PMT. This energy spectrum is allowed by the constant fraction discriminator (CFD) which provides timing signals and is used to discriminate between the stop (0.511 MeV) and the start (1.274 MeV) signals through the lower and higher levels. In Fig.5.1 we include the relation between the peak position and the delay time of the stop signal (the inset figure) and we found fairly well linear curve fits for the whole experimental data. The slope of the linear fit gives the channel width of the system.

5.2.2. Determination of FWHM and Source Correction

The positron window settings and the channel width were determined by using ^{22}Na source, while the resolution (FWHM) for any lifetime spectrometer was obtained from the analysis of Si reference spectra by using the LT analysis routine [2] version 9.0. The reference spectrum was resolved into three lifetime components with a source contribution between 11-20 % to get the final analysis of the data (as shown in Tab.5.1) and in the fitting routine LT the background was a free parameter. For every measurement at least 4 × 10^6 events were accumulated in each spectrum. An example of determination the FWHM for fast-fast lifetime spectrometer by using the Si as a reference is represented below in Fig.5.2a.

```
Final fit                         Si.Ref3


Analysed between channels   22 and 300.  Calibration = 0.02550 ns/chann.
  Total counts= 4271525                 Bkgr./signal=1.37 %

Fit's variance =1.0940              Date:      16/07/2007     08:11:05

SAMPLE:
intensities [%]        lifetimes [ns]        dispersions [ns]
100.0000              0.21810(0.00023)       0.0000

SOURCE :
contribution           17.7248 [%]
intensities [%]        lifetimes [ns]
47.6702                  0.1600
50.5819                  0.3800
1.7479                   1.9065

ZERO CHAN.     35.92837(0.00015)        BACKGROUND    209.7738    [Counts]

RESOLUTION CURVE :
    ESG fract. (%)     Shift (chnns)         FWHM (ns)     tau(left) (ns)      tau(right) (ns)
         80.0000          0.0000              0.2910          0.0000              0.0000
         20.0000         -1.0000              0.2065          0.0000              0.0000
```

Tab. 5.1. The final analysis of the Si reference spectrum by using the LT routine.

Two source lifetimes appear to come from the Al foil (0.16 ns) and NaCl salt (0.38 ns) while the third which is a very small *o*-Ps lifetime of 2 ns may come from some kind of surfaces. The total source intensity varied from 8-17 %, depending on the source strength. The resolution function was determined as a sum of two Gaussian curves. It is assumed that the second Gaussian has an relative intensity of 18 % and is shifted with respect to the first one by one channel (0.025 ns) to the left side (shorter lifetimes).

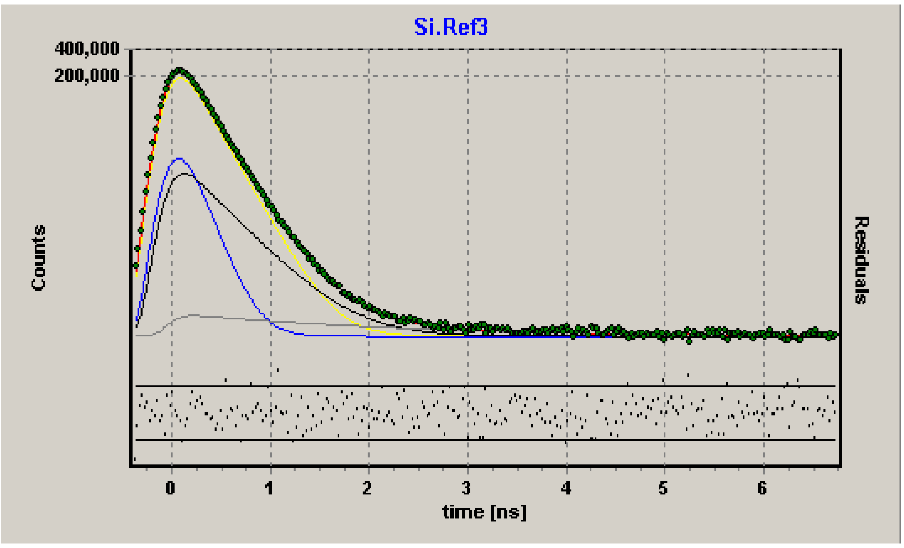

Fig.5.2a. The three lifetime components (yellow, black and blue colours) which have been analysed in the Si as a reference.

In porous glass media, which have rather complex pore structures, the pores show a certain size distribution. Hence, the *o*-Ps decay rate λ shows the same behaviour and can be described by a continuous function λ (R). Thus the long lifetime component in the spectrum can be approximated by Gaussian or continuous log-Gaussian distribution of λ (R).

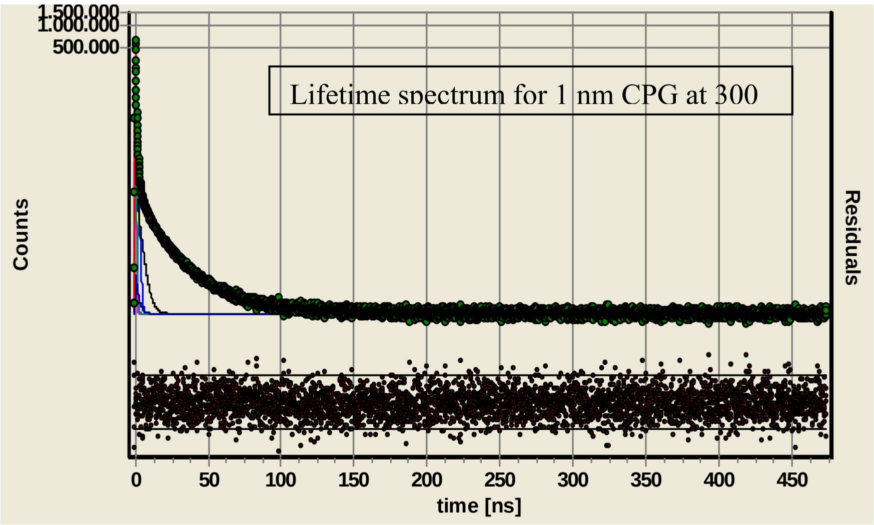

Fig.5.2b. Fitting of lifetime spectrum of 1 nm CPG by using the LT program. The analysis process includes 4 lifetime components.

A best analysis for the spectra of porous glass could be obtained by using four lifetime components [3] as shown in Fig.5.2b; the *p*-Ps ($\tau_1 = 0.125$ ns), the annihilation of free positrons in bulk ($\tau_2 \approx 0.4$ ns), the annihilation of the *o*-Ps inside the matrix of the glass ($\tau_3 \approx$ 1.5 ns) which was usually fixed in the analysis and the annihilation of *o*-Ps in the pores of the glass (τ_4). The spectrum was analysed by the LT program [2] and supposed to be a sum of exponentials and one log-Gaussian distribution of exponential data function:

$$N(t) = \sum_i I_i \lambda_i \exp(-\lambda_i t) + \frac{I_4}{\sigma_i \sqrt{2\pi}} \times \int_0^\infty \exp\left[-\frac{\ln^2\left(\tau_{ip}\lambda\right)}{2\sigma_i^2}\right] \exp\left(-\lambda t\right) d\lambda \qquad (5.1)$$

where λ_i are the decay rates of the discrete components, I_i are the relative intensities, τ_{ip} is the lifetime at the peak of the distribution and σ_i the width of the decay rate distribution. Furthermore, the spectrum of the lifetime is asymmetric, cut at 142 ns, while the LT program fits to log-Gaussian distribution without taking into account this upper limit for the *o*-Ps lifetime.

These measurements were carried out with sources of different activity (1.6, 3, 4.5, 5.8, and 7 μCi). Such weak sources are required to obtain the long lifetime component in a sufficiently precise way [4] because the intensity of τ_4 in our CPG samples is rather weak (5%). Therefore, if we use a strong source, the decomposition of the long lifetime component to an appropriate value will be disturbed. The γ-quanta were reordered by using BaF_2-Hamamatsu system. Further parameters of the measurement are: channel width = 0.121 ns/ch, 8000 channels from the MCA, and the resolution function with the new equipments is 0.220 ns. The shortest lifetime component (*p*-Ps) under these conditions could certainly be resolved from the free annihilation component.

5.3.The First Step in Probing Porous Glass by PAS

The long-lived *o*-Ps component is plotted as a function of temperature for a pore size of about 2 nm as shown in Fig.5.3. The direction of the T-dependence measurements is illustrated by up and down arrows such that the first and the last measurements were at 300 K in cycle.

The hysteresis behaviour of the measured data may be ascribed to the shrinkage of the pores; we observe that as the temperature decreases (down arrow) below 300 K, the *o*-Ps lifetime increases significantly which is a typical *o*-Ps lifetime T-dependence behaviour in that pore size as we will see later. Over the same temperature range but in the opposite direction (up arrow) the *o*-Ps lifetime is significantly reduced with increasing the temperature which may be ascribed to shrinking in the pore size due to the capillary condensation effect.

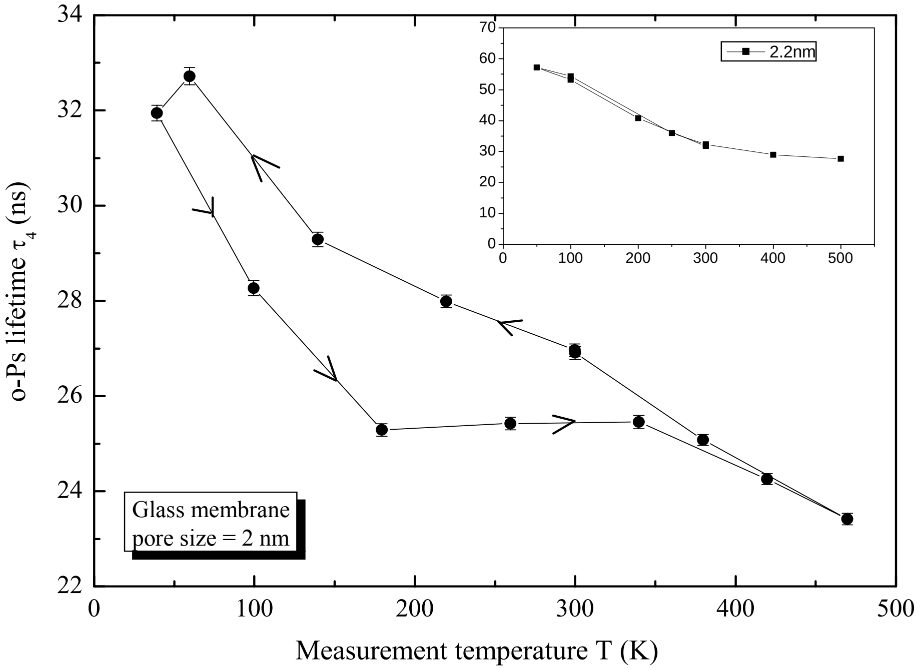

Fig. 5.3. The o-Ps lifetime τ_4 as a function of temperature T for CPG with 2 nm pore size before modification of the vacuum system. The inset figure shows the T-dependence measurments after improving the vacuum.

The inappropriate vacuum pressure ($\approx 10^{-4}$ mbar) of the system in that time contributed obviously in the hysteresis loop (shrinking effect). In such conditions of vacuum pressure *o*-Ps has finite probability of interacting with the surrounding medium, which in that case is the moisture of the air. The consequence of such an interaction is reducing the *o*-Ps lifetime through ''quenching'' process, by producing 2γ-rays during annihilation. These results enforced us to improve the vacuum pressure conditions of our system, through the modification which has been described in detail in chapter 3. In the modified system, the sample can be subjected to an evacuation pressure of an order of 10^{-7} mbar in a few hours, which is improved to 10^{-8} mbar after 24 hours. The inset figure represents the same measurements of a similar porous powder glass with a pore size 2.2 nm measured in the modified system. Moreover, by comparing the two figures we can observe the effect of evacuation pressure on the improvement on the *o*-Ps lifetime value at 300 K.

In the main figure, it is important to refer that the lifetime measurements were carried out with a stronger source which leads to a difficulty in resolving the long lifetime component from the spectrum as of the peak to background ratio becomes small. In the simulation chapter we will see how the source activity is an effective parameter in determination of the long *o*-Ps components.

5.4. Pore Size Determination by PALS (Calibration Curve)

We used PALS as a non-destructive tool to determine the pore size *D* for a system of control porous glass (CPG). The long lifetime component τ_4 which appears in the lifetime spectra as a result of annihilation of the *o*-Ps can be used as a probe to porous glass and supplies information about the pore size. The given pore sizes of our CPG samples were determined with nitrogen adsorption method. One of the disadvantages of this tool is that it strongly depends on model assumption and is not accurate for pore sizes of less than 10 nm. For this reason we decided to calibrate the pore sizes by the sensitive positronium lifetime technique and compare the experimental data with the theoretical data for the verification of the proposed models.

The first calculations I carried out with the calcRTE routine [5] developed in our group which is based on the rectangular extended TE-model (RTE-model) [3]. This routine allows calculating the *o*-Ps lifetime for cubes as a function of the size *D* and the temperature *T,* the *o*-Ps lifetime τ_4 can be converted to the mean pore size *D*. The overlapping parameter *ΔR* (0.18 nm) may be used as a parameter. Usually, up to 1000 energy levels can be included in calculation.

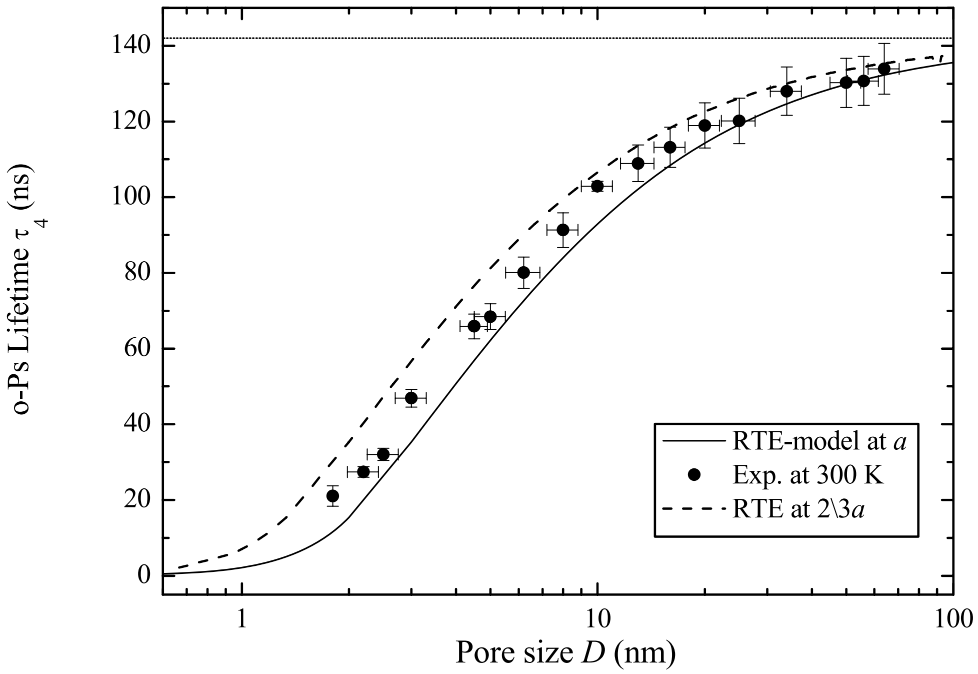

Fig 5.4a. The *o*-Ps lifetime τ_4 as a function of the pore size *D* for CPG. Closed circles (●) are our exprimental data at 300 K: Dashed curve (---) are the theoretical results of RTE-model for the cubed geometry with *ΔR*= 0.18 nm at **(**2/3**)***a* length and the solid curve (-) for *a*.

The experimental measurements of the *o*-Ps lifetime τ_4 as a function of the average pore sizes *D* at T = 300 K are shown in Fig. 5.4a. The experimental data show a general agreement with theoretical calculations of the RTE-model for cubed geometry well with side length *a*, and with side length (2/3)*a* [3].

All these calculations were repeated using the new routine EELViS developed recently by R. Zaleski from the University of Lublin [6]. The routine is based on the extended TE-model (ETE) [8] and has the advantage that the shape and dimensionality of the pore can be selected, since the pores in our samples have an open and irregular structure. The pore size is defined as the mean free path within the pore. It has the general, shape-independent definition given as;

$$D = 4V/A_{sp}$$

where V is the specific volume of all pores and A_{sp} the specific pore surfaces.

As we referred previously, in the ETE-model [8] when the *o*-Ps lifetimes are calculated, the shape of the pore must be assumed. There are two possibilities: three-dimensional pores like spheres or cubes, and two-dimensional pores like (circular) infinite long cylinders and bars (infinite long channel with square cross-section). Infinite long cylinders seem to be the best approximation to model the structure seen by the scanning electron microscope. Either the lifetime can be calculated for a given pore size and temperature, or the pore size (here radius, $r = D/2$) for a given lifetime and temperature. Thus the following relations are valid:

spheres: $D = 2d/3$, cubes: $D = 2a/3$, cylinders: $D = d$,
roads (square cylinders): $D = a$, plates: $D = 2a$,

where d is diameter of the sphere or cylinder and a is the linear dimension of the cube, road, or plate. The overlap value ΔR can be used as a parameter. I must remark that the overlap parameter ΔR obtained by fitting to the data from the porosimetry depends slightly on the assumed structure since the different pore shapes give different theoretical lifetimes for the same mean free path D.

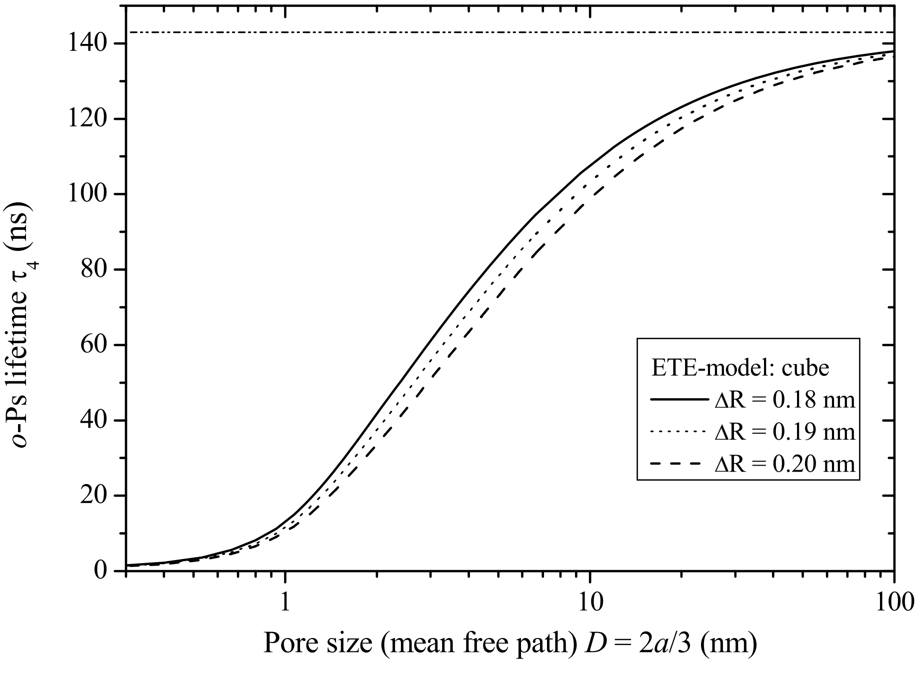

Fig. 5.4b. The *o*-Ps lifetime as a function of the pore size D (mean free path) for cubes with the side length $a = 3D/2$. The solid, dashed, and dotted lines are the theoretical results of the ETE-model with the overlap parameter ΔR as parameter: $\Delta R = 0.18$ nm, 0.19, and 0.20 nm.

Figure 5.4b shows the relative dependence overlap parameter ΔR, the *o*-Ps lifetime calculated with the ETE-model is plotted as a function of the parameter ΔR (0.18 nm, 0.19, and 0.20 nm) for cube pores geometry of side length $D = 2a/3$ nm. All the three curves show almost identical behaviour instead of a minor displacement with respect to each other (As a result of a multiplicative scale factor in pore (potential) length $2a/3$).

Figure 5.4c shows our experimental measurements of the *o*-Ps lifetime τ_4 as a function of the mean pore sizes D at $T = 300$ K. The experimental data show a significant agreement with theoretical calculations of the ETE-model [8] for cylindrical geometry well with overlap parameter ΔR at three different values: ΔR= 0.18 nm, 0.19 nm and 0.20 nm. From comparison of the theoretical calculations and the experimental data I estimated ΔR to be 0.19 ± 0.05 nm which is in agreement of the data of Goworek et. al [9]. Thus this curve can be used as a calibration curve for the correlation of the *o*-Ps lifetime τ_4 to the pore size D.

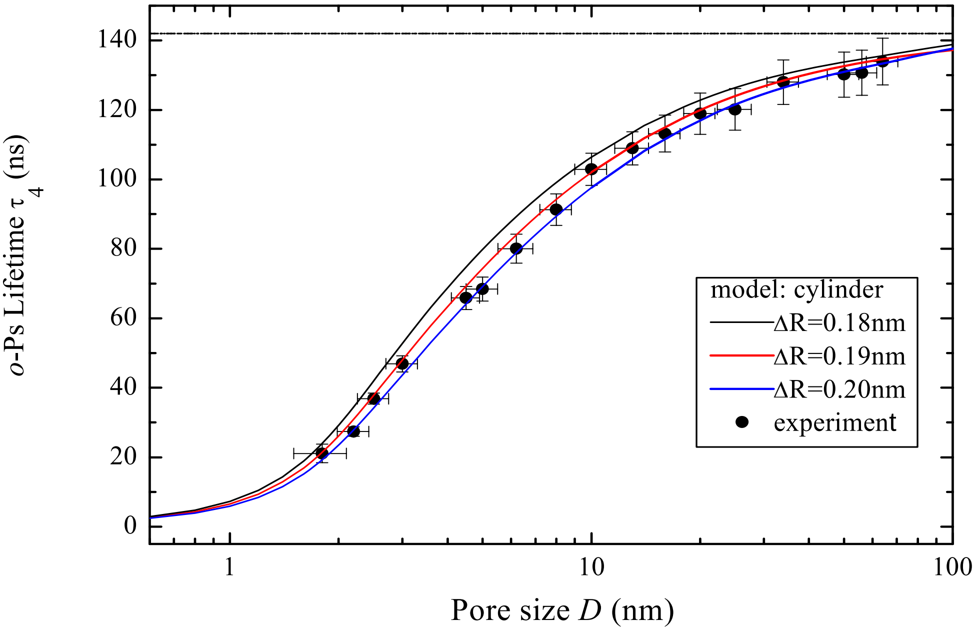

Fig. 5.4c. The *o*-Ps lifetime τ_4 as a function of the pore size D (mean free path) for CPG. The closed circles (●) represents our experimental data at 300 K, the black, red, and blue lines are theoretical results of the ETE-model for (circular) cylinders with ΔR = 0.18 nm, 0.19 nm, and 0.20 nm. From the comparison we estimated ΔR = 0.19 (±0.05) nm in agreement of the data of Goworek et. al.[9]. .

The *o*-Ps lifetime in porous glass is significantly dependent on the pore size in the range of <15 nm, hence the positron annihilation technique can be used as an effective tool for the determination of the pore size. However, both of Fig.5.4a and Fig.5.4c can be used as calibration curves for determining of the pore size of porous media, but it is obvious also that our experimental data is in better agreement with the three dimensions cylindrical pore geometry of the ETE-model calculations (Fig.5.4c) than the cube geometry of the RTE-model (Fig.5.4a).

In Fig. 5.4d we present the theoretical calculations of the *o*-Ps lifetime as a function of the pore size *D* for different physical pore geometries (circular cylinder, square cylinder, sphere and cube) with the ETE-model and ΔR = 0.19 nm. We can observe that all the curves are identical above 10 nm and are relatively shifted below the same value as shown in Fig.5.4d. All the three curves have similar shape but are displaced relatively with respect to each other (As a result of a multiplicative scale factor in pore (potential) length $2a/3$).

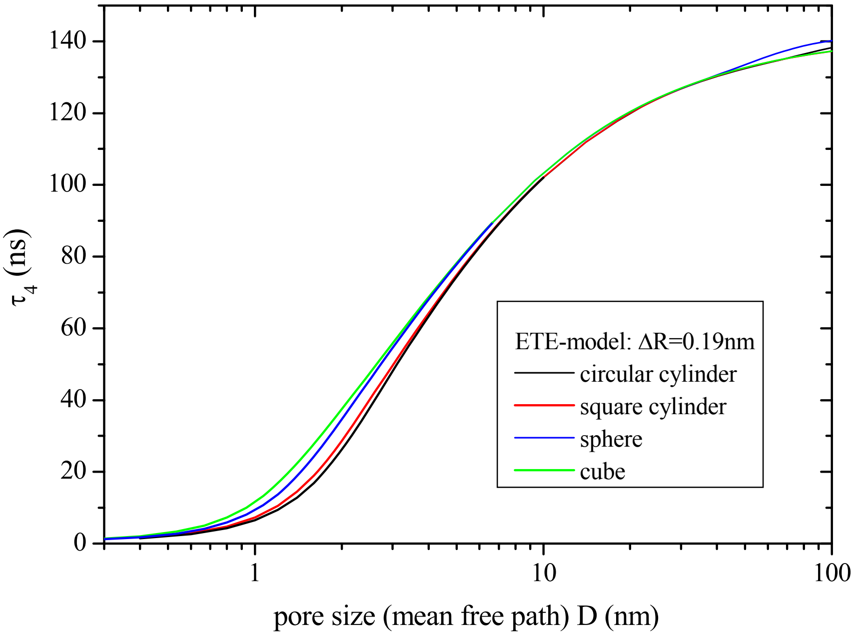

Fig. 5.4d. The *o*-Ps lifetime as a function of the pore size *D* (mean free path) for (circular) cylinders (diameter $d = D$), bars (square cylinders, side length $a = D$), spheres ($d = 3D/2$), and cubes (side length $a = 3D/2$). All for an overlap parameter ΔR = 0.19nm at 300 K.

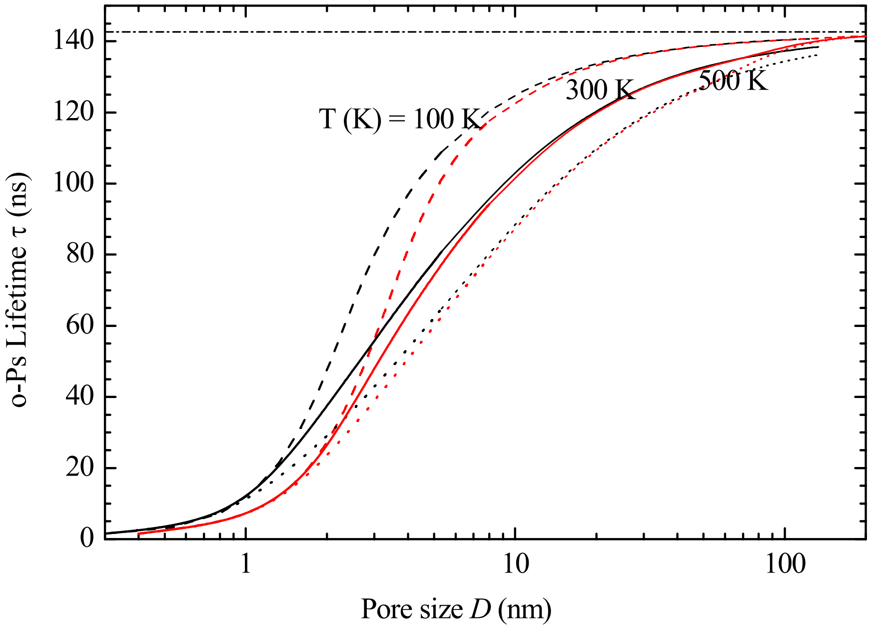

Fig. 5.4e. The *o*-Ps lifetime as a function of the pore size *D* (mean free path) in the ETE-model for cylinders (red curves) and cubes (black curves) at three different temepartures 100, 300 and 500 K.

The theoretical calculations of the *o*-Ps long lived component as a function of the pore size *D* have been done by using the ETE-model for different physical pore shapes (circular cylinder and cube) at three different temperatures (100 K, 300 K and 500 K) and with $\Delta R = 0.19$ nm. The result of calculations is shown in Fig.5.4e and as we observe that the pores shape play a main role below 10 nm especially at low temperatures (≤ 300 K). However, this dependency of the *o*-Ps lifetime on the pore geometry at the same temperature increases with decreasing the pore size *D* below 10 nm.

Figure 5.5 shows the correlation between the pore size *D* which has been calculated from the *o*-Ps lifetime by using the cylindrical ETE-model with $\Delta R = 0.19$ nm and the pore size *D* from smaller than 15 nm. For pore sizes $D < 10$ nm we recognize both of the estimations of the two methods are closed to each other, but for $D > 10$ nm where the division in calculation between the two methods becomes more clear (the standard division of pore sizes from the chemical porosimetry in y-direction becomes more larger). Hence, these results confirm the accuracy and efficiency of the PALS as a tool in probing free volumes and pores in porous materials.

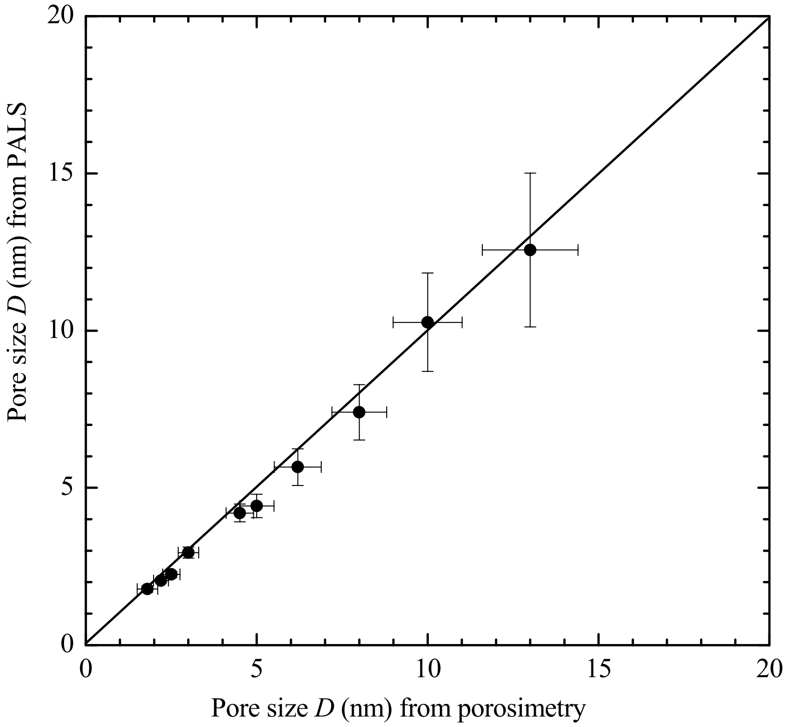

Fig. 5.5. Result of the calibration. The pore size *D* from the *o*-Ps lifetime calculated using the cylindrical ETE-model with $\Delta R = 0.19$ nm is plotted versus the pore size from chemical porosimetry ($D = 4V/A_{sp}$) for pore sizes smaller than $D = 15$ nm.

5.5. The *o*-Ps Lifetime and the Positron Source Activity

To get proper results when measuring porous systems one has to take into account the activity of the positron source because the long lifetime component is comparatively weak in intensity. When using too strong positron sources the long lifetime component is completely overlapped with the background as shown in Fig. 5.6 and a correct analysis of the spectra is not possible.

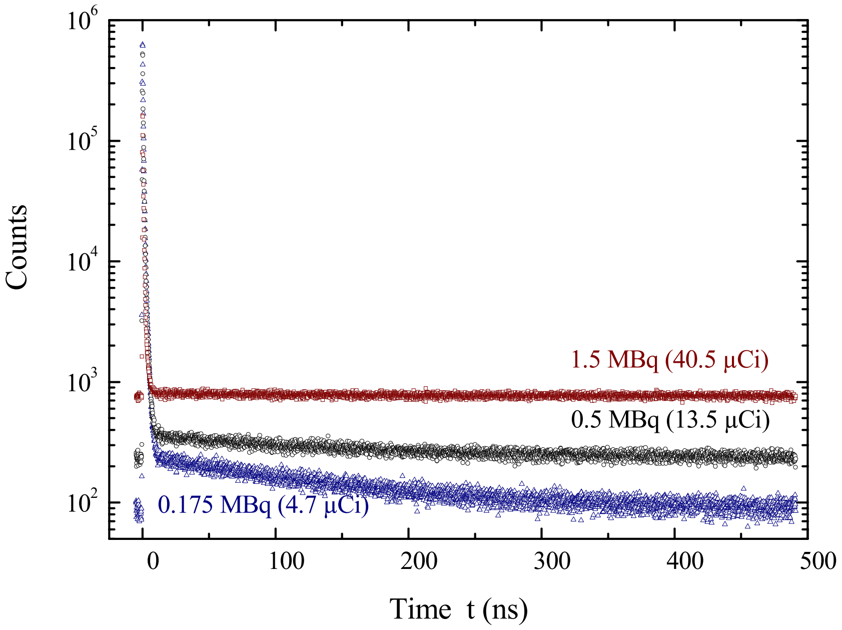

Fig.5.6. Simulated PALS spectra of porous glass using different positron source activities.The lifetime component τ_4 is increasingly overlapped by the background for the stronger sources.

The presented section tries to give a recipe in handling the measurement of the long lifetime component in mesoporous glass. Several simulations were done to get information on the dependence of the analysed positron lifetime of *o*-Ps in porous glass on the activity of the positron source in use.

5.5.1. Parameter of Simulations

The simulation of the PALS spectra were done by using the Monte-Carlo model. A common PALS spectrum of porous glass consists of four different lifetime components as explained above. Similar for our experimental data the intensities and lifetimes were fixed for the simulations as following: τ_1= 0.125 ns with I_1 = 25 %, τ_2 = 0.5 ns with I_2 = 58 %, τ_3 = 1.5 ns with I_3 = 12 % and I_4 = 5 %. τ_4 was varied in the range from 10 ns to 142 ns. By varying the background in the PALS spectrum different source activities were simulated by using the following equation:

$$A = BG / (CW \times Area) \qquad (1)$$

BG is the background, *CW* is the channel width in seconds, Area is the number of total counts and *A* is the source activity in Bq. The background is approximated with a constant value because the positron source activity is comparatively weak. Every individual simulation was done five times and an average lifetime with related standard deviation was calculated for τ_4. For analysis of the spectra the routine LT version 9.0 was used [2, 7]. In the fitting routine the background was a free parameter. Further parameters of the simulation were: channel width = 0.124 ns/ch, number of channels = 4000, time zero channel = 40, FWHM of single Gaussian resolution function = 0.250 ns.

Spectra with different total count numbers from 0.25×10^6 to 16×10^6 were simulated first to find a convenient number of counts for a preferably short but also accurate experimental measurement. The aim is here to achieve a standard deviation of the *o*-Ps lifetime in the pores $\Delta\,\tau_4$ that complies with $\Delta\,\tau_4/\tau_4 = 1\ \%$.

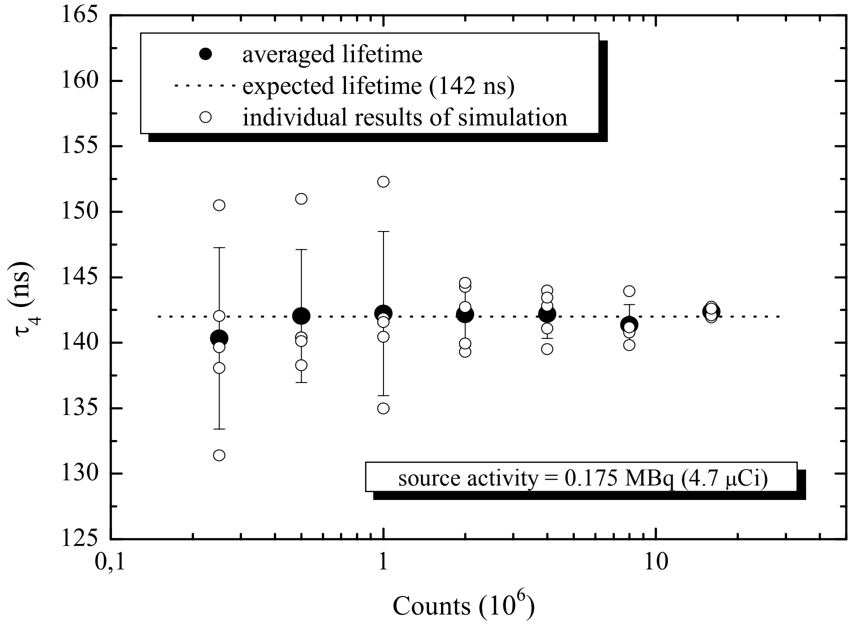

Fig.5.7. Dependence of the analysed lifetime τ_4 on the total area of the spectrum using a source activity of 0.175 MBq. A total count number of 4 x 10^6 is acceptable and used for all further simulations.

In the simulation shown in Fig. 5.7 τ_4 was fixed to 142 ns and the source activity was chosen to 0.175 MBq (~ 5 μCi). It is obvious that the best agreement of expected and fitted lifetime is obtained using a count number of 16×10^6. Measuring such a high number of counts is not applicable in our experimental setup because of the long measurement time. However, a total area of the spectra of 4×10^6 were found to still give a reasonable accuracy with not too long measuring time. Thus, all following simulations were done using a total count number of 4×10^6.

Our second goal was to study the dependence of the analysed lifetime and its statistical accuracy on the positron source activity. For shorter and longer lifetimes (10 ns to 142 ns) spectra with 11 different positron source activities (0.015 to 1.5 MBq, corresponding to 0.5 to 41 μCi) were simulated. An overview of the results of the lifetime component τ_4 of the analysed spectra and its statistical error is shown in Fig. 5.8. Here is shown show the average values of five individual simulations. Indeed, the averaged lifetime τ_4 is always close to the expected one but the statistical uncertainty reaches unacceptable large values for strong positron sources. In this case it is not possible to obtain the expected lifetime τ_4 in a sufficient way from the analysis of a single PALS measurement.

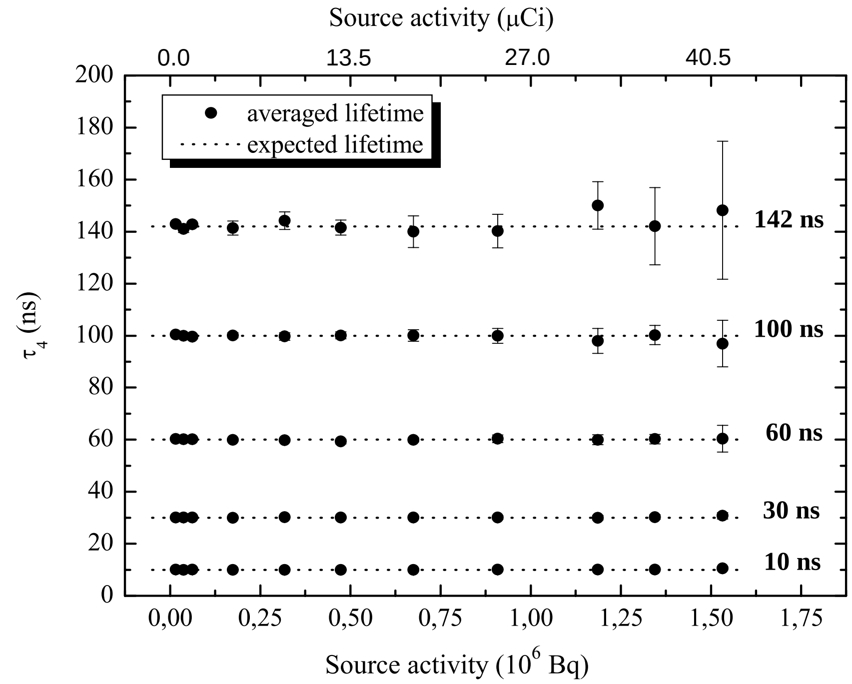

Fig.5.8. Overview of the dependence of the averaged *o*-Ps lifetime calculated for the different 5 simulated lifetimes (10…142 ns) on 11 different positron source activities.

Only for weak sources (<0.2 MBq ≈ 5 μCi) the individual results are close to the expected value, but for precise measurements even weaker sources or higher statistics are required. The scattering of the individual five results especially for long lifetimes is obvious, as to be seen in detail in Fig. 5.9 were I plotted also the single analysis of the simulations for $\tau_4 = 142$ ns.

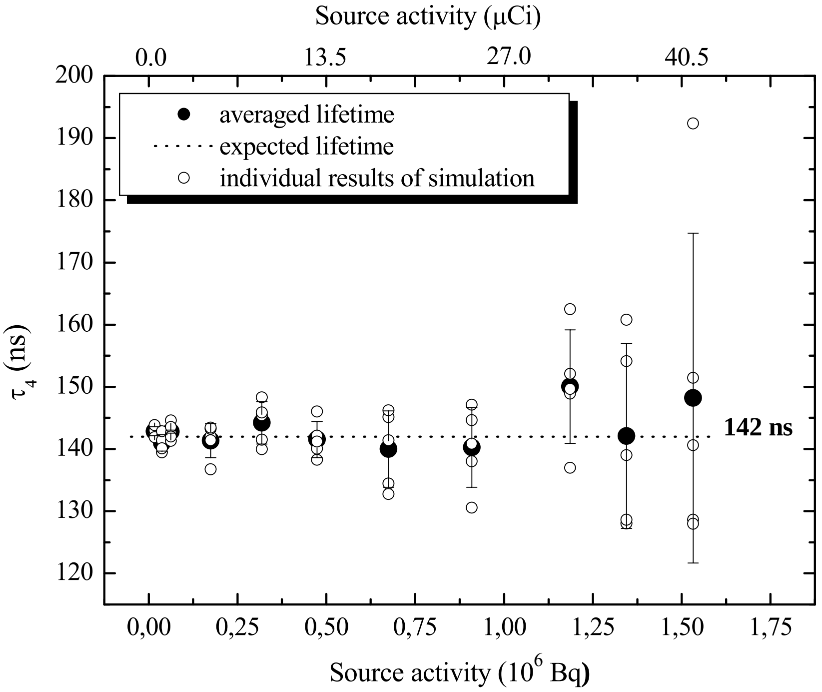

Fig.5.9. Detailed illustration of the simulations shown in Fig. 5.7 for a simulated lifetime of 142 ns displaying also the individual results of the five simulations. Average lifetime and the expected lifetime are in agreement with acceptable accuracy only for rather weak positron sources.

In Fig. 5.10 the resulting standard deviation for the averaged lifetime of the 5 individual simulations for all lifetimes using positron sources of different activity is plotted. The results show a strong increase of the statistical uncertainties with higher source activity. For example, a positron source activity of 1.5 MBq (~ 41 μCi) which is typical for investigations on semiconductors causes an uncertainty $\Delta\tau_4/\tau_4$ of 10 %.

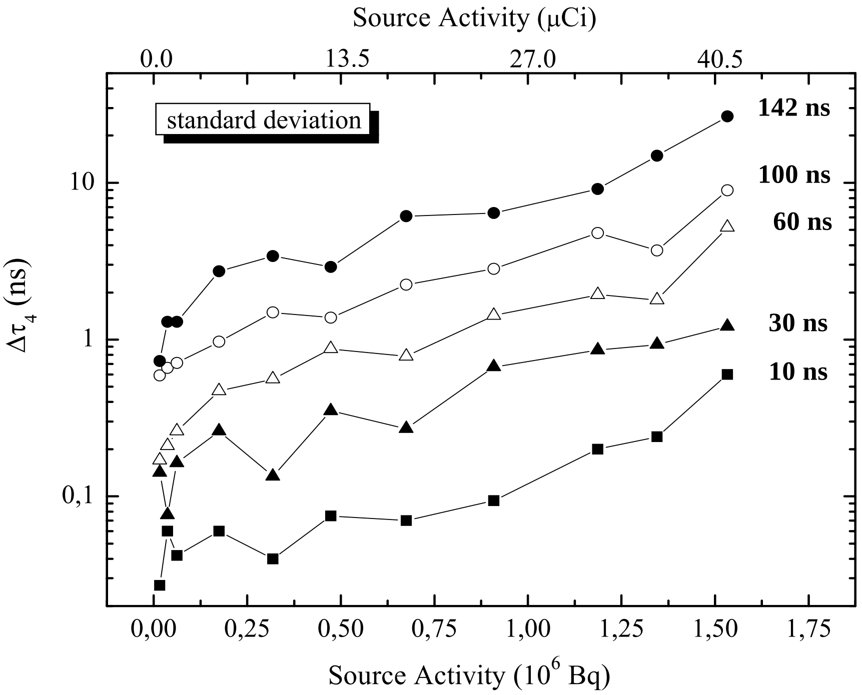

Fig.5.10.The standard deviation of the average lifetime dependence on the used positron source activity. A strong increase of the statistical uncertainties with higher source activity is obvious.

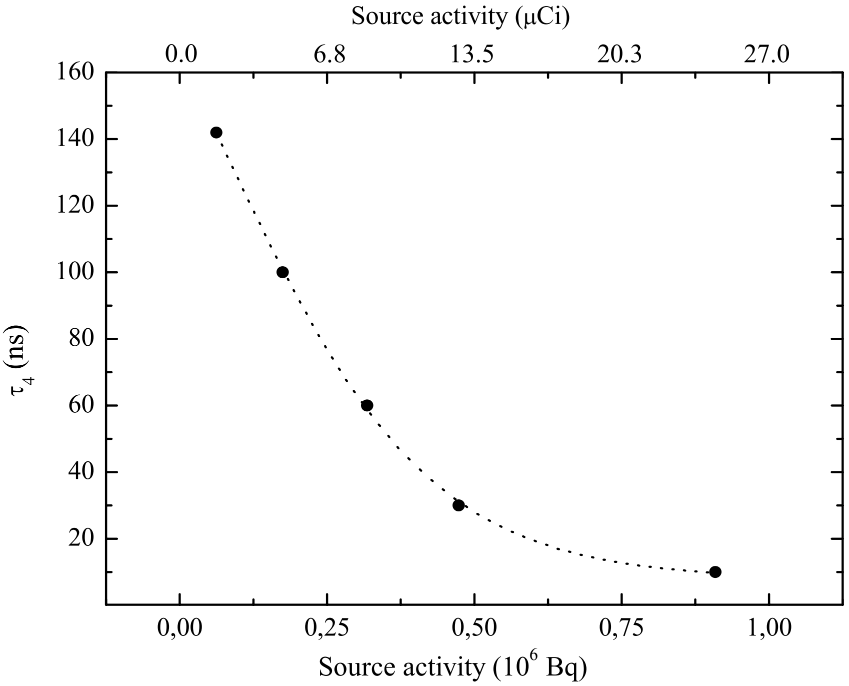

Fig.5.11. The dependence of the lifetime on the maximum source activity that still complies with $\Delta\tau_4/\tau_4 = 1$ %. This curve can be used as a recipe in choosing an adequate source activity for the expected lifetime.

Concluding the results one can find in Fig. 5.11 the maximum source activity that complies with $\Delta\tau_4/\tau_4 = 1$ % as a function of the lifetime τ_4. This curve should be understood as a recipe in choosing an applicable positron source activity for a PALS experiment on porous systems using a total count number of 4×10^6.

5.6. Temperature Dependence Measurements

Temperature dependent measurements are considered one of the important experimental methods to understand the annihilation with the material. In order to avoid capillary condensation a UHV-compatible cryostat was constructed with temperature controller and under a constant evacuation through a turbo pump. Furthermore, we carried out subsequent positron lifetime measurements at 50 K for the sample 5 nm as a check to the cryo-condensation effect. A slight reduction of the positronium lifetime τ_4 was only observed after repeated measurements over 3 days as shown in Fig.5.12, so that the effect of cryo-condensation of the residual gas can be ignored, where the sample is warmed after every measurement.

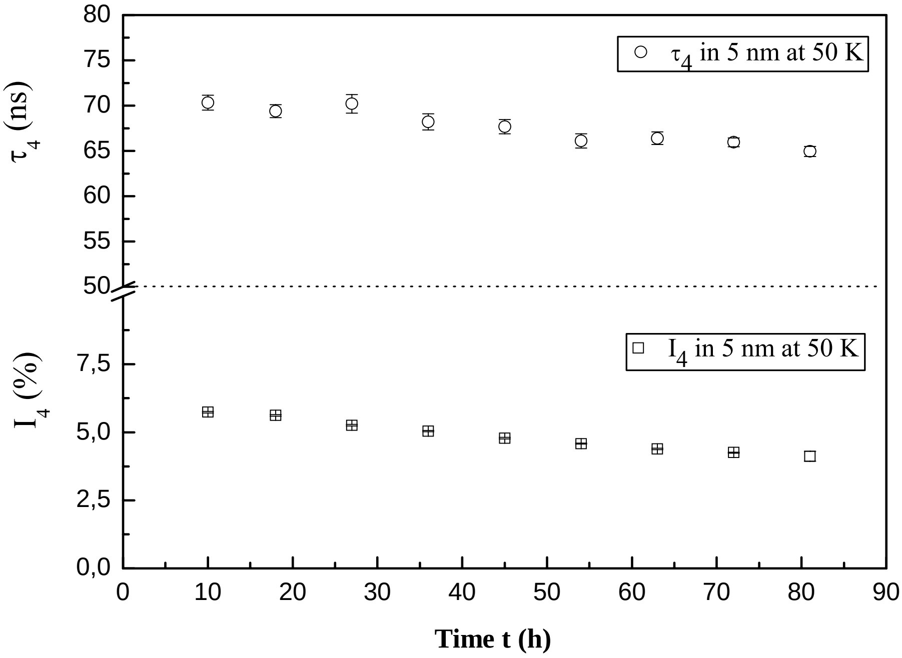

Fig.5.12. The *o*-Ps intensity and lifetime τ_4 in 5 nm CPG as a function of time t at 50 K.

Temperature dependent measurements of *o*-Ps lifetime spectra were carried out in the range 50-500 K with 50 K step for a set of CPG system. There were two goals behind these measurements, firstly was studying the T-dependence of the *o*-Ps lifetime in these materials, and hence the changes attached this behaviour with increasing the pore sizes. The second reason was verifying the RTE- [3] or the ETE-models [8] which have theoretically treated these studies.

Figure 5.13 shows the results for the CPGs samples of pore size between 1 and 2.5 nm. As we can observe there is a significant decrease in the long lifetime component τ_4 with increasing the temperature, which reveals the population process between the various energy states and tend to the long lifetime component with increasing the pore size. The behaviour of our T-dependence measurements for the two samples is in agreement with RTE-model [3] and with the experimental data was obtained before by Goworek. et al. [9] but in a disagreement with the theoretical calculations which have been done by RTE-model for cubed pore geometry with $\Delta R = 0.18$ nm. Which is contrary to the literature data available until now. The best fit for the data in Fig.5.13 has been done by the ETE- model (Eq. 3.8) [8] for cylinder pore geometry with $\Delta R = 0.19$ nm.

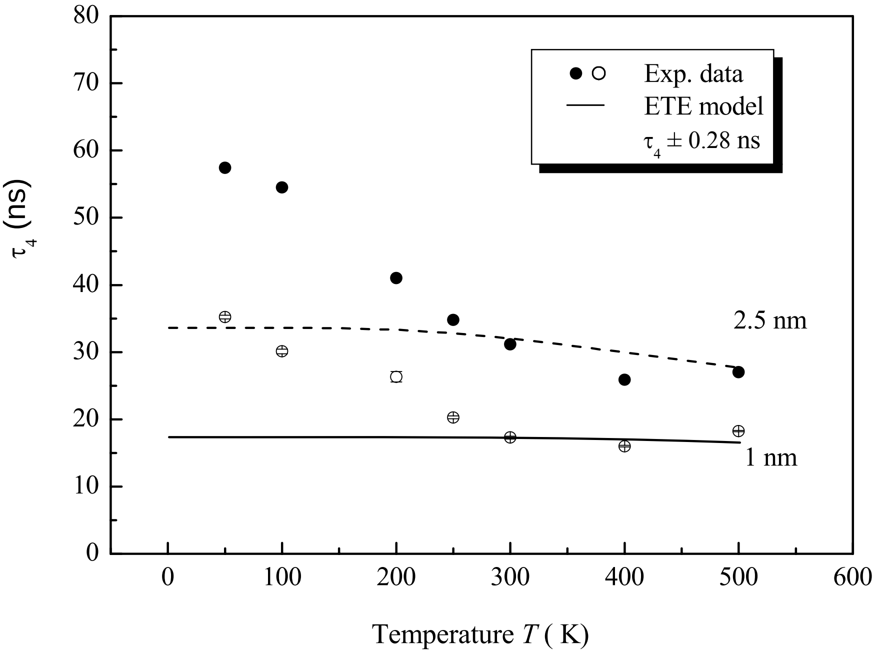

Fig.5.13. Temperature dependence of *o*-Ps lifetime τ_4 in CPG with pore sizes of 1 nm and 2.5 nm (from porosimetry). The solid and the dashed lines represents the result of calculation according to Eq.3.8 for $D = 1.618$ nm and 2.246 nm, as estimated from PALS.

The experimental measurements and the theoretical calculations for pores sizes of 3 nm and 4.5 nm are presented in Fig.5.14. However, we can observe a slight variation in the value of *o*-Ps lifetime for both samples, as well at intermediate pore size 4.5 nm, there is a significant agreement between the experimental and the theoretical treatment of the ETE-model [8].

I carried out some other lifetime measurements in the range of 50 K to 500 K with 25 K step and by using the new Hamamatsu PMTs. The measured T-dependence of the lifetime in comparison to the theoretical calculations for small pores (3 and 4.5 nm) is shown in Fig. 5.15. However, it is clear to observe that the experimental data for a pore size of $D = 4.5$ nm also agrees fairly to the ETE-model. Moreover, as well the experimental data and the theoretical fit for 2.5 nm become more close to each others especially above 200 K and deviated at low temperature.

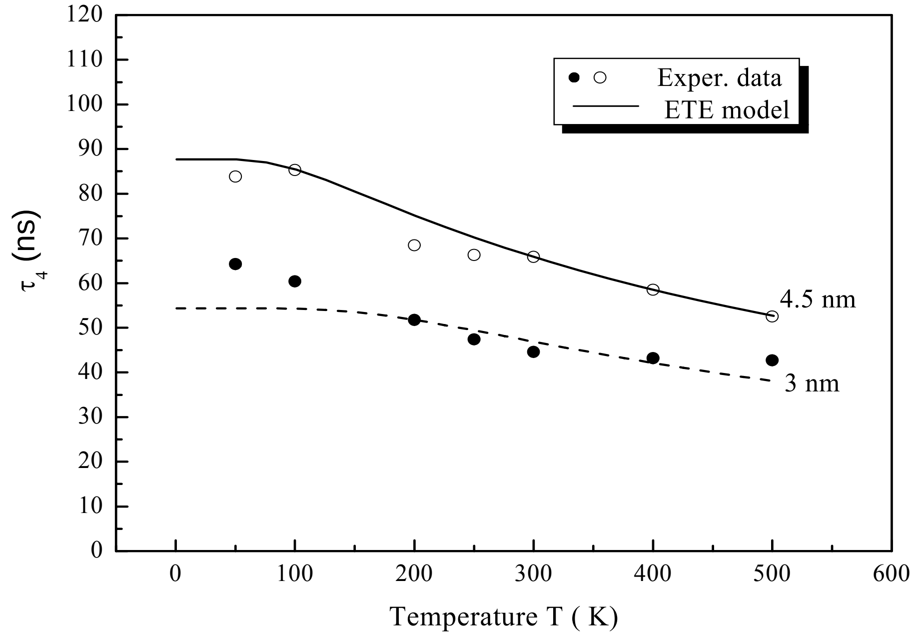

Fig.5.14. Temperature dependence of *o*-Ps lifetime τ_4 in pore sizes 3 nm and 4.5 nm (from porosimetry). The dashed and solid lines represent the result of calculation according to Eq.3.8 for D = 2.93 nm and 4.2 nm respectively.

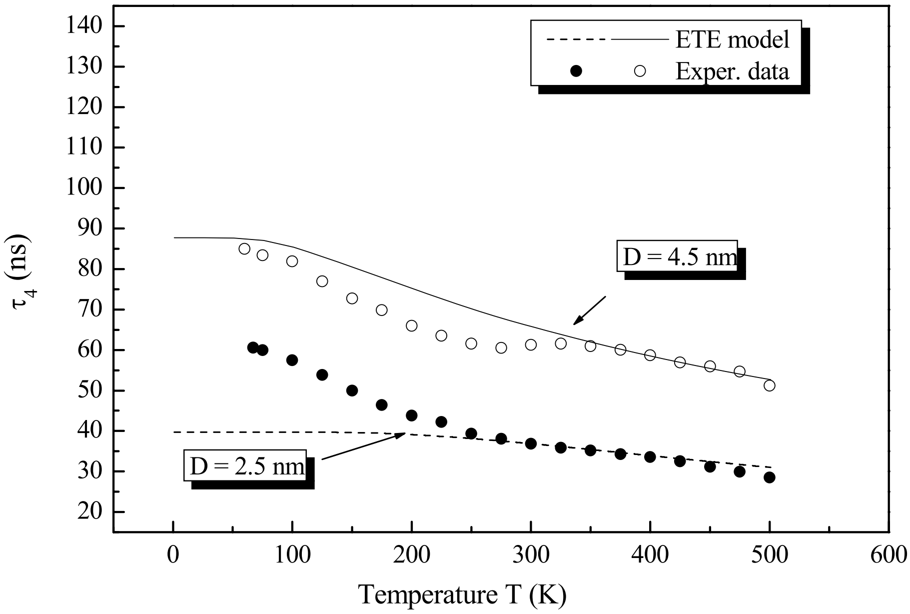

Fig.5.15. The *o*-Ps lifetime τ_4 vs temperature T for CPG with pore sizes 2.5 nm and 4.5 nm (from porosimetry). The dashed and solid lines represent the result of calculations according to Eq.3.8 for D = 2.46 nm and 4.2 nm, respectively.

I have already repeated the T-dependent measurements of 4.5 nm, just only to check the stability of the system with the new equipment and I found the same. The *o*-Ps lifetime T-dependence measurements of different pore sizes between 1 and 27 nm are shown in Fig.5.16. According to the experimental data for larger pores (6.9 nm and 27 nm) one can recognize a contrary temperature dependent behaviour in comparison to the small pores (< 5 nm) and expectations of the ETE-model below 300 K. The shortage in the long lifetime component compared to the calculations of ETE model in large pore sizes can be explained in the light of understanding the bonding effect of the *o*-Ps atom with molecular atoms at the wall of pores. This bonding effect is due to weaker forms of intermolecular attractions called Van der Waals dispersion forces. In large pore sizes, the *o*-Ps molecule has the ability to be excited between different energy states with a thermal energy $\frac{5}{2}K_B T$ and at low temperatures the *o*-Ps atoms slow down. Therefore, the attraction becomes large enough for the *o*-Ps molecules to stick at the wall of the pore and reducing the long lifetime component. While the increase of the *o*-Ps lifetime for small pores such as 1nm, 3nm and 4.5 nm at low temperatures may be ascribed to the deviation of the potential well from the suggested shape (cubed shape is suggested in RTE-model for pore size $D \geq 1$nm). This deviation leads to shifting the *o*-Ps energy levels in the potential well. I would like also to refer that the sample of pore sizes 16 nm and 13 nm were checked two times, and in all measurements we obtained approximately the same results.

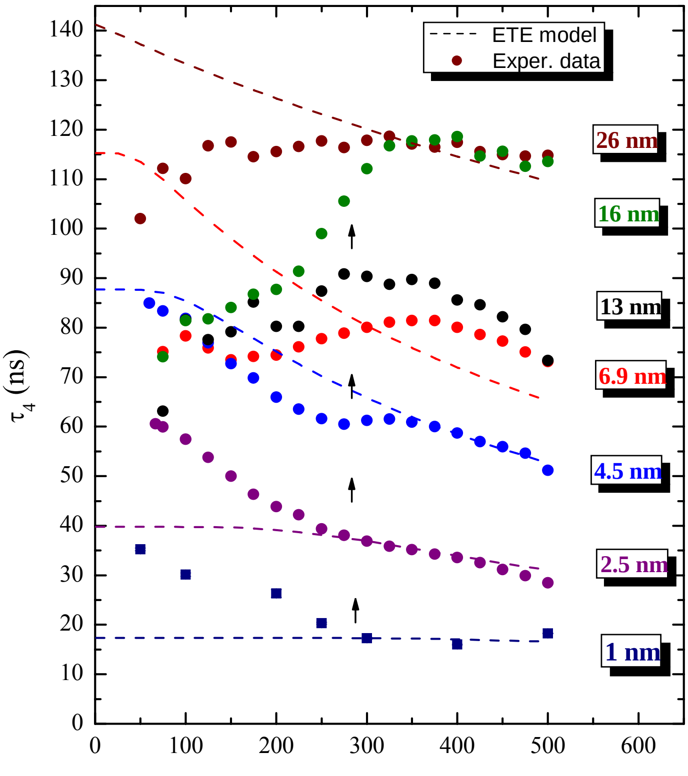

Fig.5.16. Temperature dependence of *o*-Ps lifetime τ_4 in CPG with various pore sizes. The dashed lines represents the results of calculations according to the ETE-model.

Figures (5.17-5.20) represent the *o*-Ps long lifetime component τ_4 as a function of the pore size D at different temperatures (50 K, 100 K, 200 K, and 500 K). The curves which have been calculated according to the ETE-model at these temperatures are added. At low temperatures of 50 K and 100 K the experimental data, which are shown in Fig. (5.17-5.18), reveal a disagreement to the theoretical calculations.

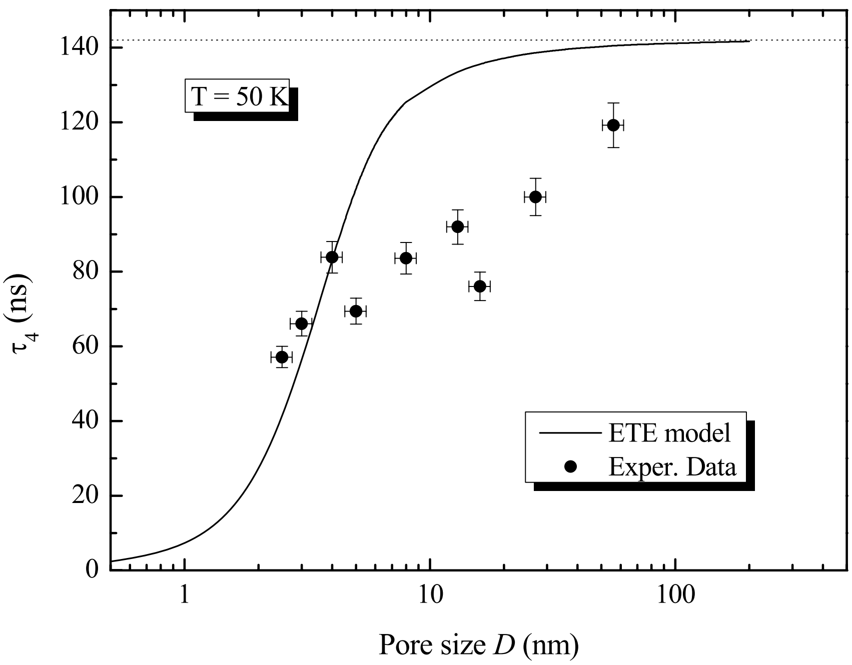

Fig. 5.17. The variation of *o*-Ps lifetime τ_4 as a function of the pore size *D* at 50K. The solid line represents the calculations according to the ETE model.

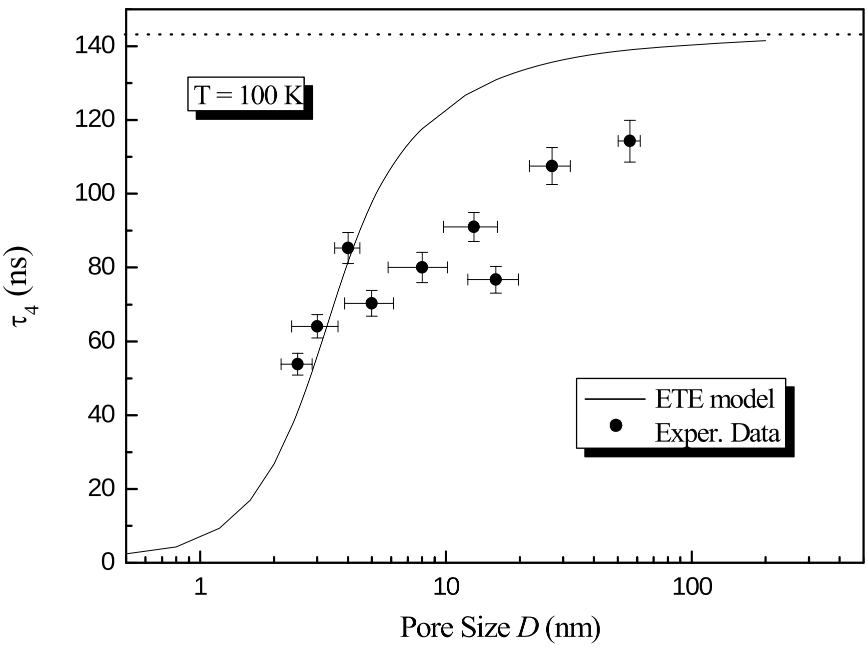

Fig. 5.18. The variation of o-Ps lifetime τ_4 as a function of the pore size *D* at 100 K. The solid line represents the calculations according to the ETE model.

For a temperature of T = 200 K the experimental data and the theoretical treatment become more closed in behaviour as shown in Fig. 5.19. As already mentioned an agreement to the model for smaller pores is only observed for T = 300 K (Fig. 5.5c). At higher temperature of T = 500 K we did not find a sufficient agreement to the ETE-model as shown in Fig. 5.20. The theoretical calculations of the dependence of the lifetime τ_4 on the temperature are shown in Fig.5.21, where the ETE-model [8] where used for the calculations.

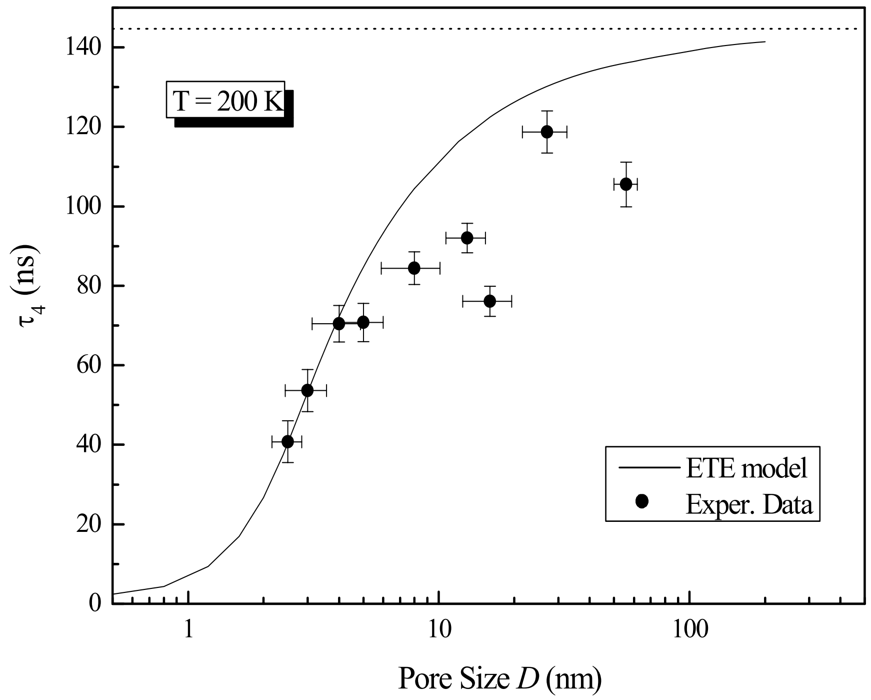

Fig. 5.19. The variation of *o*-Ps lifetime τ_4 as a function of the pore size D at 200 K. The solid line represents the calculations according to the ETE model.

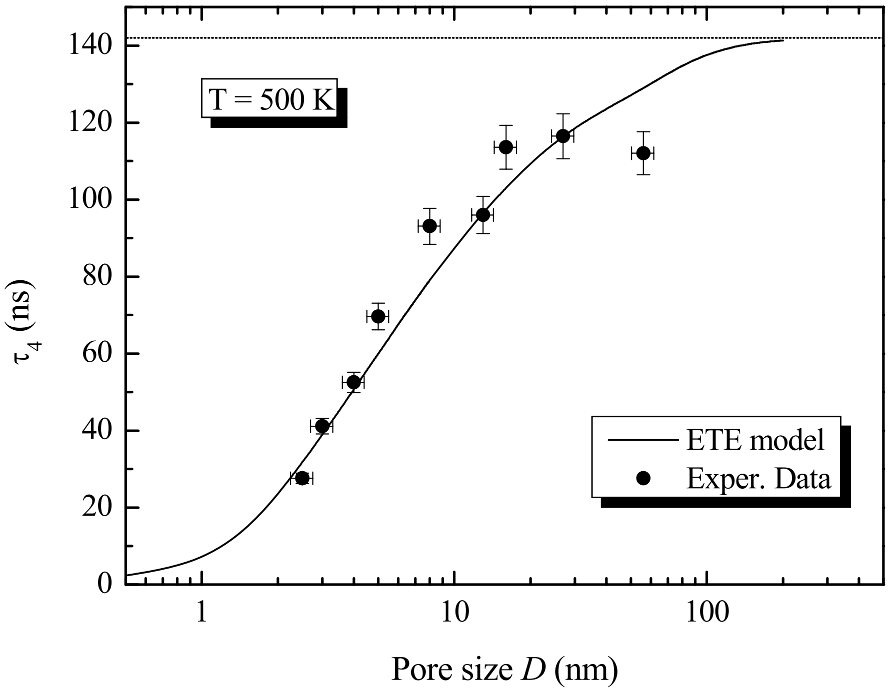

Fig. 5.20. The variation of *o*-Ps lifetime τ_4 as a function of the pore size D at 500 K. The solid line represents the calculations according to the ETE model.

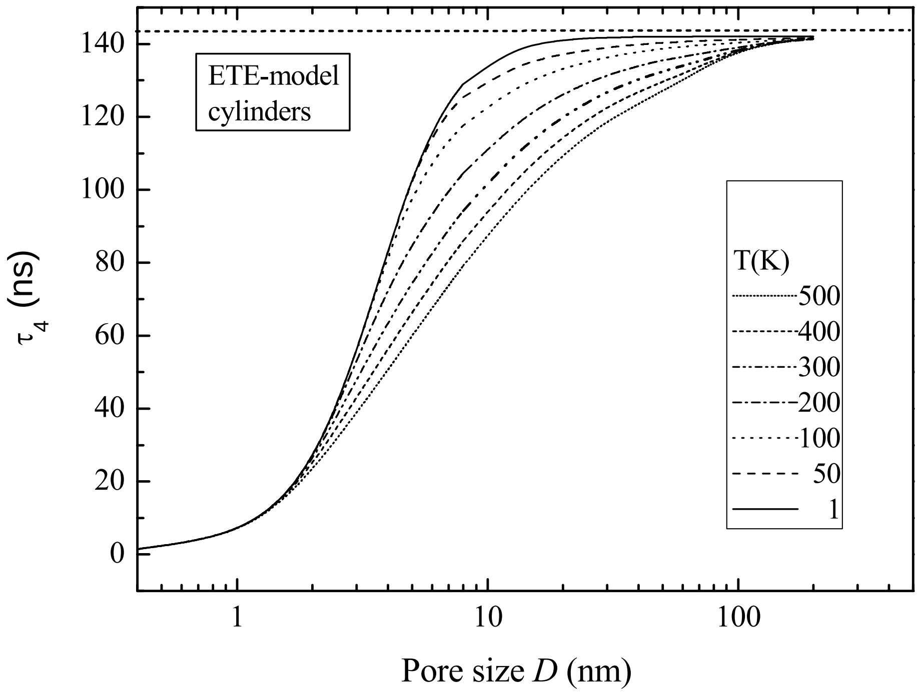

Fig.21. The variation of the *o*-Ps lifetime as a function of the pore size *D* at different temperatures T according to the ETE- model caculations.

5.7. Complex Pore Size Structures

Positron annihilation lifetime (PALS) is often used in investigation complex material structures. It was really interesting in this part to check the high sensitivity of the positron technique to different structures of CPGs with different pore sizes.

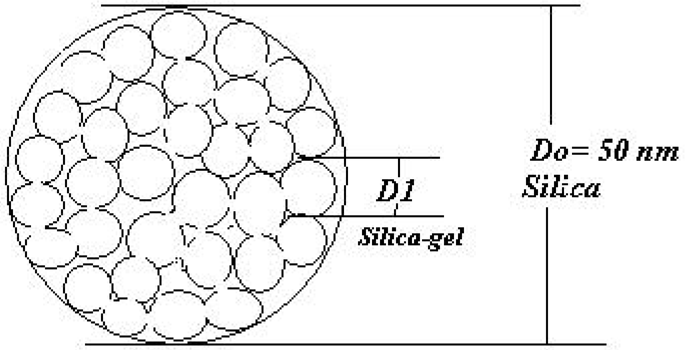

Fig.5.22. Schematic representation shows the complex structure of the main pore size (50 nm) and the well defined silica-gel (D_1).

The host structure under investigation consists of silica and have spherical shape structure with pore size D_o= 50 nm. These host samples contain smaller pores of silica-gel in the form of a net of channels with different pore sizes D_1 as shown in Fig. 5.22. Of course, there are open space cages isolated from the channels. As well known, the difference between silica glass and silica-gel is only in the shape of pores and the distribution of these pores inside the sample. It is important to refer that the pore size of silica-gel in the first sample has not been exactly supplied from institute of technical and macromolecules chemistry in Martin-Luther University but with an expectation to be between 1.4 nm and 2.7 nm.

The samples were studied at 300 K as a powder by two plastic scintillates detectors coupled to XP2020 PMTs. The positron lifetime spectra were registered in 4000 channels covering 500 ns from the TAC. The spectra were analysed by using LT program [2] as 4 lifetime components and with including 2 resolution functions (0.255 ns and 0.320 ns). The contribution of the longest resolving time component fixed to be 15 % from the total resolution function. In order to simplify the spectral analysis and to resolve the short lifetime component τ_1 (*p*-Ps) from the free annihilation one τ_2, the *o*-Ps component τ_3 in small bulk cavities and long lived component τ_4 were assumed as continuous lifetimes (including distributions). Thus the four lifetime components and their relative intensities were free in the LT analysis. The results of the analysis are shown in Tab.5.2. As we conclude from the data, the *p*-Ps lifetime component is successfully resolved from the whole spectra and from the free annihilation component.

D_1 (nm)	$\mathbf{D_0}$	τ_1 (ns)	I_1 (%)	τ_2 (ns)	I_2 (%)	τ_3 (ns)	I_3 (%)	τ_4 (*ns*)	I_4 (%)
1.4--2.7	**(50)**	0.124 ± 0.002	29.1 ±1.2	0.328 ± 0.013	2 9.0 ±1.4	0.994 ± 0.78	33.2 ± 1.8	35.54 ± 0.34	8.65 ± 0.28
2.7	**(50)**	0.130 ± 0.002	57.7 ± 1.3	0.375 ± 0.013	29.2 ± 1.3	0.970 ± 0.12	12.4 ± 1.3	36.62 ± 0.68	3.06 ± 0.10
4	**(50)**	0.132 ± 0.007	15.6 ± 1.6	0.392 ± 0.006	19.6 ± 2.6	0.862 ± 0.09	57.4 ± 2.9	69.2 0 ± 1.40	8.43 ± 0.52
4.5	**(50)**	0.125 ± 0.004	19.4 ± 2.5	0.327 ± 0.016	15.5 ± 2.4	0.830 ± 0.10	58.3 ± 3.1	81.2 0 ± 1.90	6.70 ± 0.45

Tab. 5.2. Positron lifetime data at room temperature obtained by LT analysis for CPG samples of different structures and pore sizes. The analyzed parameters are followed by their standard divisions.

It is interesting to learn from the long-lived component τ_4 that the positron is sensitive only to the small pore sizes (from 1.4 nm to 2.7, 2.7 nm, 4 nm and 4.5 nm) which indicates the distribution of these pores inside the larger one (50 nm). In the same time we could not have more data about the large pore size (host), but it is obviously that these host structures are completely filled with the small pore sizes such that we cannot see any open pore larger than the content samples. Furthermore, from comparing τ_4 and the remained lifetime parameters of the first and second sample, we can confirm that both of samples have the same pore size as well the same structure form.

5.8. Cryo-Condensation Effect

The adsorption isotherms of simple gases onto disordered mesoporous solids at low temperatures usually exhibit large hysteresis loops of type 2 according to the IUPAC classification [10]. This type of hysteresis shrinks with increasing temperature and eventually disappears at a hysteresis temperature T_h [11], which depends on the mean pore size but lies below the critical temperature T_c of the bulk fluid. T_h is not necessarily equal to the pore critical temperature T_{cp} at which a gas-liquid coexistence in pores vanishes [12-15].

PAS has already been used to study the capillary condensation of different gases in mesoporous glass [16, 17]. In vacuum the *o*-Ps annihilates via emission of 3γ-rays and has a lifetime of around 142 ns. The adsorption of high density gases into the pores will force *o*-Ps to annihilate via quenching in the gas and emission of 2γ-ray. A further increase in the contribution ratio of the 2γ component will be produced if a phase transition (gas-liquid) occurred inside the pores. Therefore, measuring such relative changes in the ratio of the (2γ/3γ) for the system can provide an interesting probe for the phase behaviour of fluids in confined geometries. Moreover, it will help in better understudying of the 'capillary condensation' effect in these systems.

I like to mention here that all the PAS studies to the 'capillary condensation' phenomenon were performed on a commercial 4 nm Vycro glass by using the Doppler-Broadening spectroscopy (DBS) (N(2γ/3γ) and *S*-parameters) [16]. We use for the first time lifetime technique to check this phase behaviour in our samples. We carried out many subsequent adsorption and desorption measurements with different pore sizes (8 nm, 16 nm, 20 nm, and 50 nm) in the form of membrane and powder with different gases (N_2 and CO_2). Furthermore, we checked the N- and S-parameters for most of these samples. The present CPG samples did not give any type of IUPAC hysteresis loops, in contrast to most of the conventional mesoporous materials studied until now [16, 17].

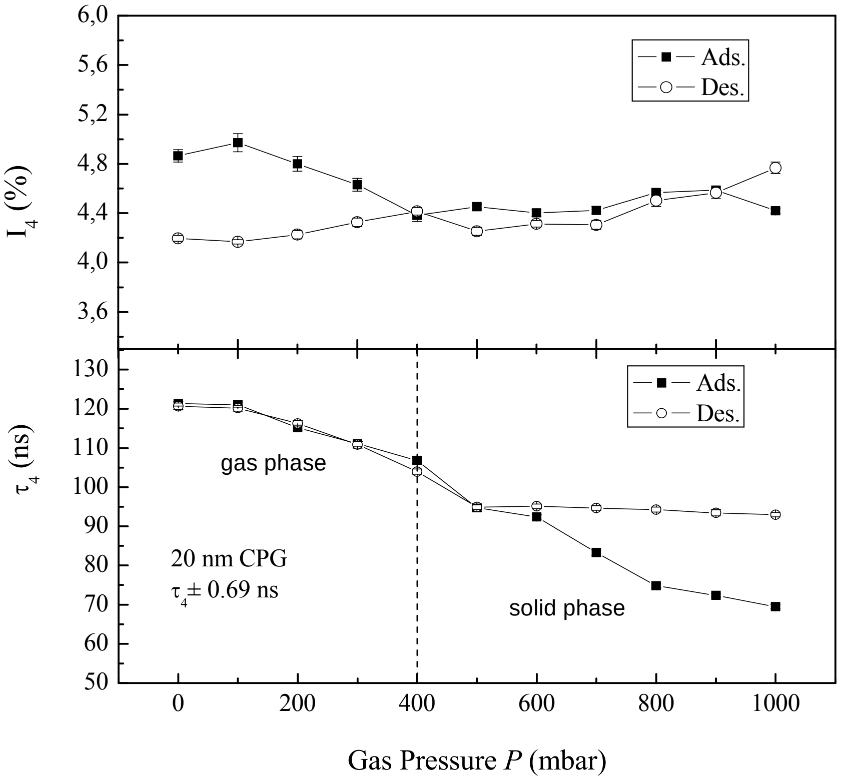

Fig.5.23. The *o*-Ps lifetime τ_4 and the intensity I_4 in 20 nm CPG as a function of increasing (open circle) and decreasing (solid cubic) pressure P of CO_2 at 180 K.

Figure 5.23 shows the adsorption-desorption isotherm of CO_2 onto the CPG of a pore size of 20 nm as a function of pressure. In Fig. 5.23 the adsorption curve (closed symbol) shows a significant decrease compared to the *o*-Ps lifetime τ_4 from the maximum value (120 ns) which was measured at 0 mbar to minimum one (69 ns) at 1000 mbar carbon-dioxide. These lifetimes of 120 ns and 69 ns correspond to a capillary pore size of 20 nm and 5 nm according to our calibration curve as shown above in Fig.5.5c. This reduction in the lifetime may only be ascribed as a partial pore filling with layer molecules of condensed CO_2 gas, hence decreasing the surface area of the pores. However, no complete filling is observed.

However, the intensity I_4 corresponding to the *o*-Ps annihilation in the pores for the same adsorption process decreases slightly from (4.97± 0.07) % to a stable value (4.58 ± 0.02) at the intermediate pressure 400 mbar. The more or less stable value of I_4 suggesting that the total number of partially filled pores does not distinctly change with increasing the gas pressure. Hence, this proves that there is a partial capillary condensation transition actually occurs within the interconnected pores of this sample.

In the same figure we can also observe from the behaviour of the desorption curve (open symbols), that the decrease of the gas pressure causes a slight increase in τ_4 which starts to increase slightly around of 400 mbar gas pressure. The adsorption and desorption branches become approximately more identical to each other below this gas pressure value. Moreover, there is no significant change in I_4 corresponding to the desorption curve. The difference between the two intensities above 400 mbar may be due to the difficulty in pumping the whole gas molecules outside the pores (where the gas is in solid phase as shown in Fig.5.24) or it is issue of time too.

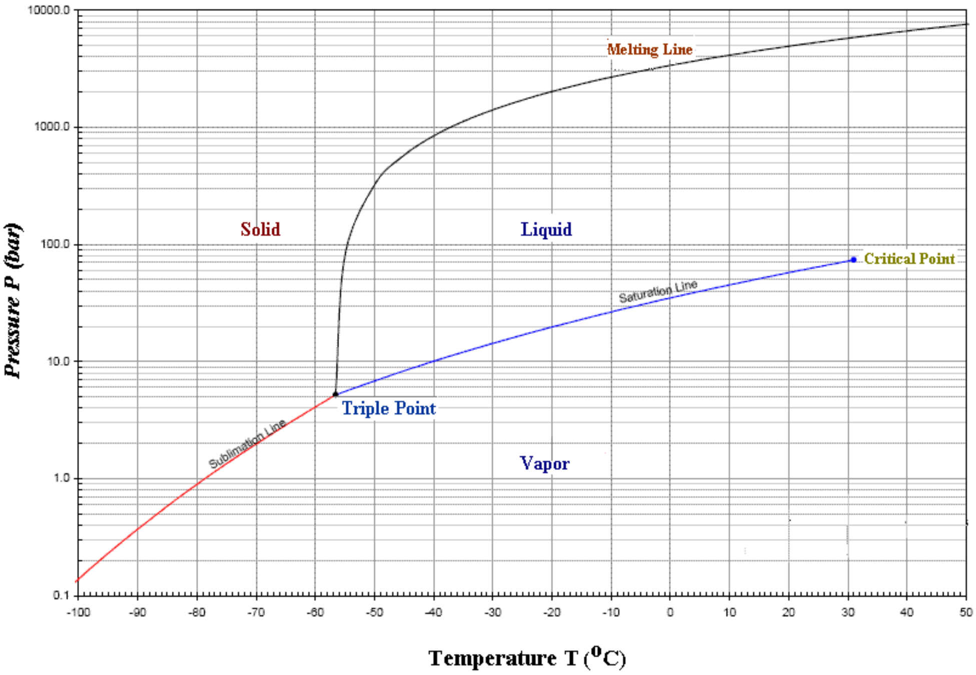

Fig.5.24. Shows the phase diagram of carbon dioxide (CO_2).

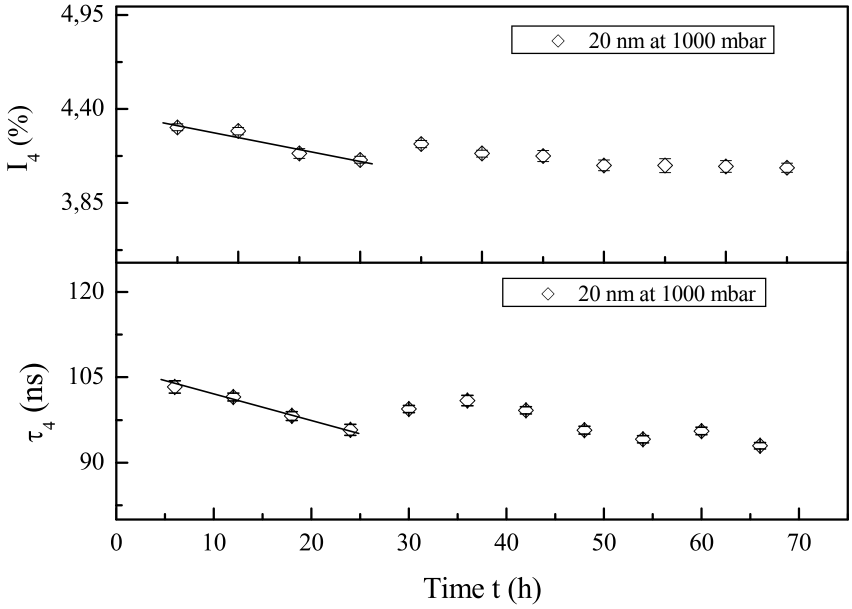

Fig.5. 25. The o-Ps lifetime τ_4 and the intensity I_4 as a function of time t (h) in 20 nm CPG at 180 K and 1000 mbar CO_2.

I studied also the time dependence of adsorption of the CO_2 in 20 nm CPG at 180 K and 1000 mbar. The goal of these experiments was to confirm that the lifetime adsorption measurement is not an issue of time. It could have been possible that the partially filled pores are completely filled after a long time. I heated the system above room temperature for 1 h to remove completely the absorbed gas of the pores. I exposed the 20 nm pores to a gas pressure of 1000 mbar after we had cooled it to 180 K. The Ps lifetime spectra were measured 11 times over 65 h. Figure 5.25 shows the long-lived component τ_4 as a function of time t (h).

It is clear from Fig.5.25 that there is a slight decrease in both of the *o*-Ps long lifetime component τ_4 and its related intensity I_4 of the adsorption experiment in the beginning. This decreasing can be considered as an indicator to the partial filling of the pores. The stability in τ_4 and I_4 over 20 hours measuring may be ascribed to blocking the pores by filling the necks of the network, hence, the pores become isolated in that case and the filling stops. The experimental data suggests to start the adsorption lifetime measurements after 25 hours from reaching the requested gas pressure, since the two parameters have a slightly stability over this time. The value of τ_4 and I_4 correspond according to the ETE-model to a capillary pore size of 7 nm. This volume obviously remains open inside the isolated pores. Thus, our open pore system becomes a closed one. The decrease in the lifetime confirms the partial decrease in the pore surface as well.

5.9. Characterization of Surface Area and Porosity by PALS

It is a well-known fact that the catalyst activity depends on the magnitude of its surface area. Solid catalysts have surface areas of about 5–1000 m^2/g in order to be effective. Therefore, solid catalysts must be porous media. The surface area is directly related to its porosity and thus it becomes evident the need to measure it. It has been demonstrated [2-9, 18-22] that porous oxides produce long life and high intensity *o*-Ps. Those porous materials are an adequate medium to study the formation and annihilation of positronium. The surface properties of such porous materials have been investigated by different analytical techniques such as the adsorption-desorption technique which is mostly based on the Brunauer-Emmett-Teller (BET) method [22], electron microscopy, small angle X-ray scattering (SAXS) [23] and angle neutron scattering (SANS) [24], etc. Each of these methods has inherent limitations due to the interactions between the probes and the system.

One of the most interesting areas of research in surface science is the search for an in situ surface technique where the probes approach surfaces internally. The most significant advantage of this is that it closely resembles practical systems, such as catalysts in fine powder forms. The characterization of surface properties by positron probes has been a new mainstream in the field of positron research. Therefore, PAS can be utilized as an in situ surface technique for routine analysis and applications related to catalysts. I therefore report here a systematic study by PALS on a set of CPG system, where the pore size, surface area and porosity is well defined.

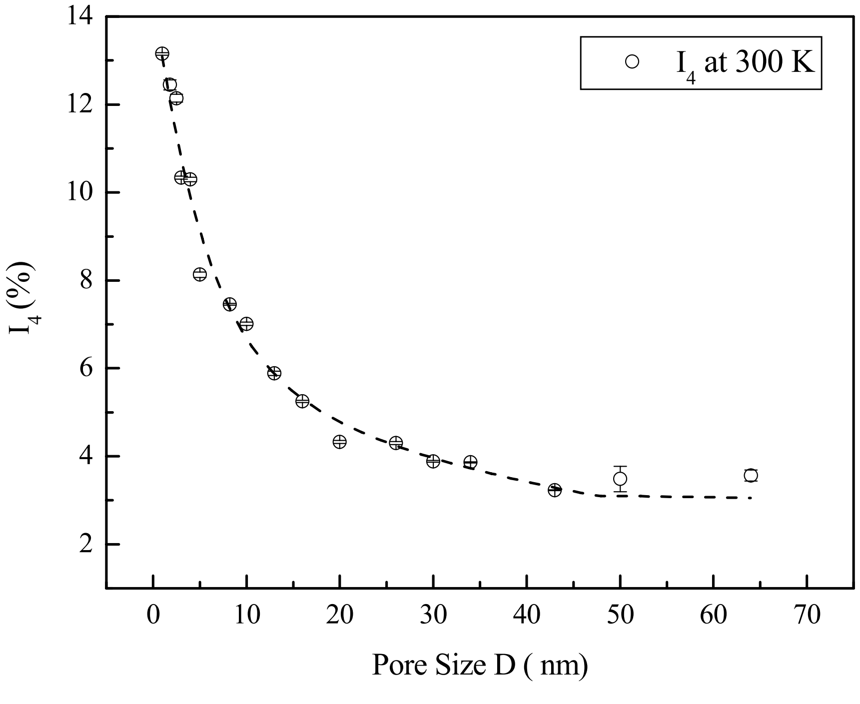

Fig.5.26. The Intensity I_4 of the o-Ps long-lived component as a function of the pore size D in a CPG system at 300 K.

Figure 5.26 represents the relation between the intensity of the *o*-Ps long-lived component and the pore size *D* for a system of CPG at room temperature. This distinct decreasing in I_4 means that the number of *o*-Ps annihilation events is decreasing as *D* increases. This is due to the fact that the inner surface area decreases. The pick off annihilation occurs at this surface. Thus the curve in Fig.5.26 can be used as a calibration curve to determine the surface Area A_{sp} of the pores at room temperature in terms of the intensity I_4 of the long-lived component. Therefore, the reduction in I_4 due to the increase in *D* will be correlated to.

In Fig. 2.27 I plot the correlations between the surface A_{sp} and the porosity ϕ (%) of a system of CPG with the intensity I_4 of the *o*-Ps respectively. It is obviously from the Fig.5.26 that the *o*-Ps intensity I_4 is related to the surface area of the CPG. This correlation can also be used as a calibration curves for the determination of the surface area for a certain pore size *D*. Therefore, since the pore size *D* and the surface area A_{sp} are known from the *o*-Ps lifetime τ_4 or its related intensity I_4 one can determine the porosity ϕ of the porous material.

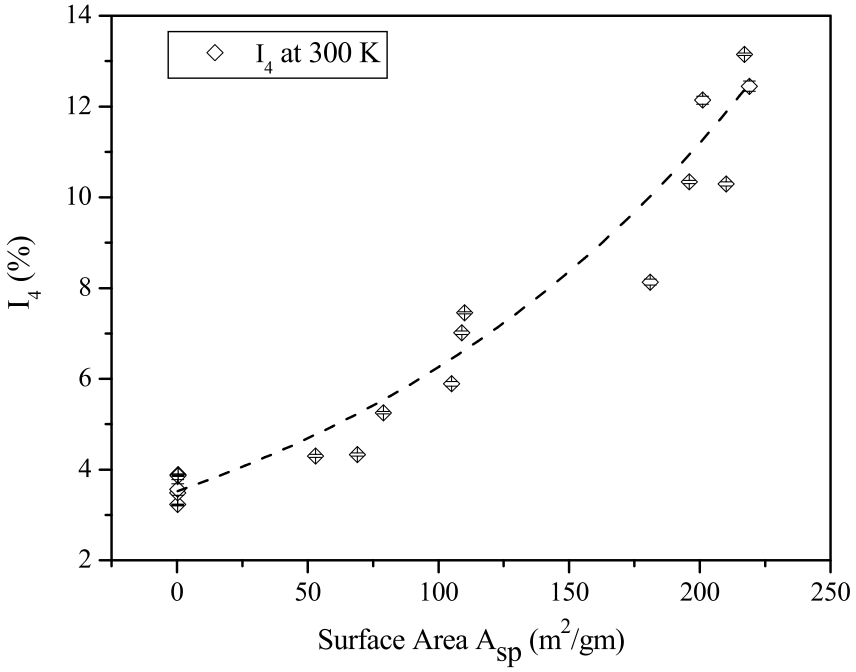

Fig.5.27. Correlation between the observed long-lived *o*-Ps intensity I_4 and the surface area A_{sp} in a CPG system at 300 K.

The porosity ϕ which is the pore volume fraction to the total system volume can be represented as [25];

$$\phi = \left(1-\mu^3\,\zeta\right)\exp\left[\frac{(1-\mu^3)\zeta}{(1-\mu^3\,\zeta)} - \frac{3(1-\mu)^2(2+\mu-3\mu^3\zeta)\mu^3\,\zeta}{2(1-\mu^3\,\zeta)^3}\right] \tag{5.1}$$

where μ is the degree of impenetrability factor such that $0 \le \mu \le 1$, and ζ is the reduced packing density and is given by

$$\zeta = \frac{\pi}{6}\,\rho D \tag{5.2}$$

where ρ is density of the bulk. For a system of totally impenetrable pores (μ =1), then we have

$$\phi = (1-\zeta) \tag{5.3}$$

And the specific surface area is simply given as

$$A_{sp} = (6\zeta / D) \tag{5.4}$$

In the case of fully penetrable pores (μ =0), one may find

$$\phi = \exp(-\zeta) \tag{5.5}$$

and

$$A_{sp} = (6\zeta / D)\exp(-\zeta) \tag{5.6}$$

Thus, it is easy to determine the porosity ϕ of a certain pore size *D* in terms of the surface area or vice versa if the intensity of the *o*-Ps component is known for that size. Hence, all the important factors (pore size, surface area, and porosity) of the pore system can be determined by a single lifetime measurements at room temperature. The correlation between the intensity I_4 of the long-lived component of the *o*-Ps and the porosity ϕ (%) of a CPG system has been plotted in Fig. 2.28.

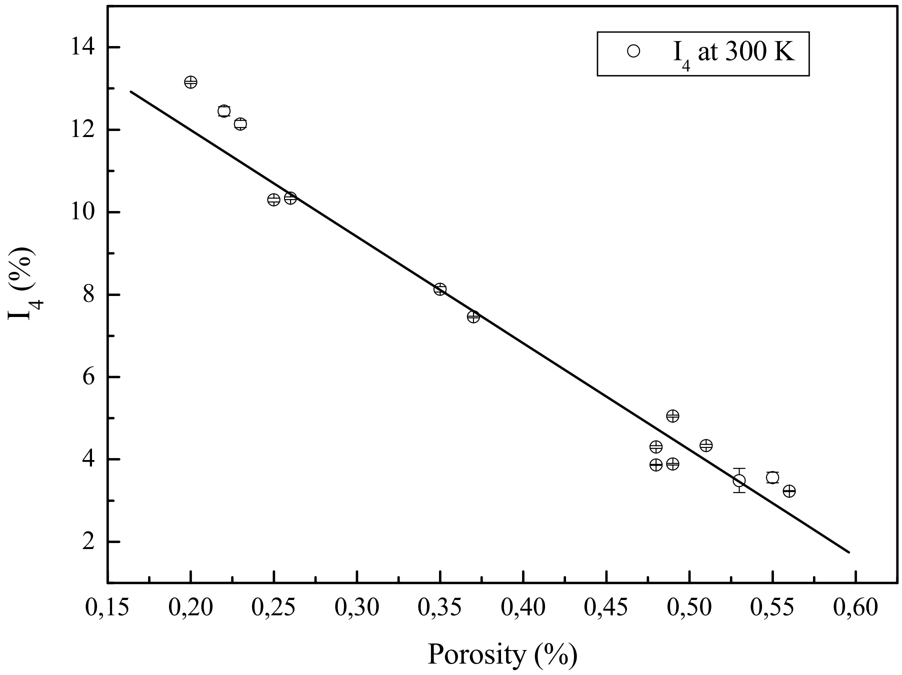

Fig.5.28. Correlation between the long-lived *o*-Ps intensity I_4 and the porosity in CPG system at 300 K. The line(-) is only guide the eyes.

Positron annihilation spectroscopy (PAS) being an in-situ and a non-invasive method involves minimal interaction with the molecular materials such as porous glasses, zeolites, and polymers. Positron annihilation lifetime spectroscopy (PALS) is probably the most widely used positron technique due to its simple experimental configuration, particularly for bulk systems as used in this thesis. PALS measures the time difference between the emission of a positron from a radioactive source and its annihilation with an electron from the material studied. In last three decades, it was already clear that the *o*-Ps has a long-lived lifetime component in these molecular materials. Positronium (Ps) spectroscopy has been used extensively as powerful tool in chemistry in probing the pore size, pore size distribution, pore connectivity and surface properties of various molecular materials such as porous media. In our studies we used porous materials in the form of powders and membranes.

To get proper results when measuring porous systems one has to take into account the strength of the used positron source, because the long lifetime component is relatively weak. When a too strong source is used, the long lifetime component is completely overlapped with the background and an acceptable analysis of the spectra is not possible. This gave us the motivation to simulate the relation between the positron lifetime and the source activity. The simulation of the PALS spectra was done using a Monte-Carlo simulation program. From the results of simulations it could be shown that a total count number of 4×10^6 is a good compromise between required measuring time and the precision of the PALS measurement. Furthermore, the effect of the positron source strength on the analysed annihilation lifetime τ_4 could be revealed. Finally a calibration curve between the *o*-Ps long-lived component and the source activity has been determined. This curve should be understood as a recipe in choosing an applicable positron source activity for a PALS experiment on porous systems.

Positron annihilation is a tool that permits, with some limitations, the determination of the average pore sizes of porous materials. In the simplest way by using a calibration curve which has been measured on a CPG system with known pore sizes (from 1 nm to 64 nm) at 300 K. The calibration curve which has been determined in this study by using the PALS is in agreement with the suggested positron models i.e RTE-model (pore cubed geometry with overlapping parameter of $\Delta R=0.18$ nm) and ETE-model (pore cylinder geometry with overlapping parameter of $\Delta R=0.19$ nm) in porous media. In the above mentioned models, the theortical calculations of the ETE-model are in better harmony with our experimental results. However, the method has its limitation in porous glass that the *o*-Ps long-lived component is strongly dependent on the pore size in the range of 1-10 nm.

I carried out temperature dependent measurements of *o*-Ps lifetime spectra in the range 50-500 K with 50 K steps for a set of CPG samples (from 1 nm to 26 nm). The *o*-Ps lifetime increases slightly with decreasing the temperature in CPG at a pore sizes less than 5 nm. The experimental results are in a fair agreement with the ETE-model only at a pore size 4.5 nm. Nevertheless, the model has not explained this increase in the *o*-Ps lifetime. We ascribed this increase in the *o*-Ps lifetime at low temperature to the deviation of the potential well from the suggested cylinder shape by the ETE-model and cubed shape by RTE-model. The result of this deviation causes a shifting of the *o*-Ps energy levels in the potential well. For pore sizes larger than 5 nm our experimental data have a contrary behaviour to the ETE- and RTE-model. The decrease in the *o*-Ps lifetime in large pore sizes at low temperatures compared to the small pores at the same temperatures may be a result of sticking the *o*-Ps atom to the atoms at the molecular wall of the pore. This bonding effect can be understood in the light of the Van der Waals force. Moreover, the ETE-model could be verified only for temperatures higher than room temperature (300 K).

Complex systems of CPG were investigated by using PALS. The hostage structures consist of silica with large pore size D_o= 50 nm. These silica samples contain well defined silica-gel in the form of a net of channels with different pore sizes D_1 (1.4…2.7, 2.7 nm, 4 nm and 4.5 nm). The *o*-Ps lifetime shows a high sensitivity to the small pore sizes without any information about the large pore size. The lifetime results have not show any open pores larger than the content samples. This really confirms that the large pores (50 nm) are completely filled with the small pores.

During our study of the capillary condensation effect in CPG with different pore sizes and different gases (such as N_2 and CO_2) by using the PALS we did not see any abrupt phase transitions. Furthermore, the later mentioned measurements just show a partial filling for the pores with CO_2. We concluded that the PALS is a standard method for the investigation of pores that are partially or completely filled with gas adsorption or even those are not accessible to gas adsorption (isolated pores), which is rather difficult if not impossible with other tools such as the adsorption-desorption or mercury intrusion methods.

By using the positron lifetime technique I was able to determine a correlation between the *o*-Ps intensity I_4, the pore size *D*, the surface area A_{sp} and porosity ϕ. These correlations can be used as calibration curves to determine the most important factors of the pore system by simple lifetime measurements at room temperature.

As a conclusion of this thesis it should be noted that despite the different measurements in this work on CPG, the potential use of positron techniques in material science research should be emphasised. In combination with other standard techniques such as SEM, SAXS, or SANS, positrons provide very valuable qualitative and quantitative information to elucidate characteristics such as surface area and the porosity of this type of molecular materials.

Chapter-1:

[1] J. W. M. Dumond, D.A. Lind and B. B. Watson; *Phys. Rev.* 75, **1949**, 1226.

[2] S. de. Bendett and H. I. Roiching; *Phys. Rev.* 85, **1952**, 377.

[3] I. K. McKenzie, T. L. Khoo, A. B. McDonald and T. A. McKee; *Phys. Rev. Lett.*19, **1967**, 945.

[4] Positron Annihilation (Proc. 9th Int. Conf. on Positron Annihilation, Szombathely, Hungary, 1991), edited by Z. Kajcsos and C. Szeles (Trans Tech Publ., Aedermannsdorf, 1992); *Mater. Sci. Forum* 105-110, **1992**.

[5] Positron Annihilation (Proc. 10th Int. Conf. on Positron Annihilation, Beijing, China, 1994), edited by Y. J. He, B. S. Cao, and Y. C. Jean (Trans Tech Publ., Aedermannsdorf, 1995); *Mater. Sci. Forum* 175-178, **1995**.

[6] Positron Annihilation (Proc. 11th Int. Conf. on Positron Annihilation, Kansas City, USA, 1997), edited by Y. C. Jean, M. Eldrup, D. M. Schrader and R. N. West (Trans Tech Publ., Aedermannsdorf, 1997); *Mater. Sci. Forum* 255-257, **1997**.

[7] Positron Annihilation (Proc. 12th Int. Conf. on Positron Annihilation, Munich, Germany, 2000) edited by W. Triftshäuser, G. Kögel, and P. Sperr (Trans Tech Publ., Uetikon-Zürich, 2001); *Mater. Sci. Forum* 363-365, **2001**.

[8] Positron Annihilation (Proc. 13th Int. Conf. on Positron Annihilation, Kyoto, Japan, 2003), edited by T. Hyodo, Y. Kobayashi, Y. Nagashima and H. Saito (Trans Tech Publ., Uetikon-Zürich, 2004); *Mater. Sci. Forum* 445-446, **2004**.

[9] C. D. Anderson; *Science* 76, **1932**, 238.

[10] C. D. Anderson; *Phys. Rev.* 43, **1933**, 491.

[11] C. Dauwe, Mdorkens, L. Dorikenes-Vanpraet, D. Segers; *Appl.Phys.* 5, **1974**, 117.

[12] S. Mohorovicic; *Astron. Nachr.* 253, **1934**, 94.

[13] A. E. Ruark; *Phys. Rev.* 68, **1945**, 278.

[14] M. Deutsch; *Phys. Rev.* 82, **1951**, 455.

[15] V. B. Beretetskii, E. M. Lifshitz, and L.P. Pitaevski; "Relativistic Quantum Theory": Pergamon Press, Oxford, **1971**.

[16] P. J. Schultz, K.G. Lynn*; Rev. Mod. Phys.* 60, **1988**, 701.

[17] P. G. Coleman (ed.); "Positron Beams and their applications": World Scientific Publishing Co., Singapore, **2000**.

[18] R. N. West; "Positron in Studies of Condensed Matter"; Taylor and Francies LTD, London, **1973**.

[19] I. Procházka; *Materials Structure* 8, **2001**, 534.

[20] G. E. Lee-Whihting; *Phys. Rev.* 97, **1955**,1557.

[21] S. de. Bendetti, H. I. Roiching; *Phys. Rev.*85, **1952**, 377.

[22] W. Brant; *Scientific American* 233, **1975**, 34; P. Houtojarvi (ed.) "Positron in Solids": Springer-Verlag, Heidelberg, **1979**.

[23] R. Krause-Rehberg, H. Leipner; "Positron Annihilation in Semiconductors": Springer-Verlag, Berlin, **1999**.

Chapter-2:

[1] R. Schnable, P. Langer; *J. Chromator*137, **1991**, 544.

[2] Lev D. Gelb, K. E.Gubbins; *Langmuir* 14, **1998**, 2097.

[3] W. Haller; *Nature* 206, **1965**, 693.

[4] W. Haller; *J. Chem. Phys.* 42, **1965**, 686.

[5] F. Janowski, and W. Heyer; Poröse Gläser, Herstellung, Eigenschaften und Anwendung, Deutscher Verlag für Grundstoffindustrie, Leipzig, **1982**, 274.

[6] F. Janowski, *Maschinenmarkt* 99, **1993**, 28.

[7] D. Enke, F. Janoswski, W. Schwieger; *Micro. and Mesoporous Material* 60, **2003**, 19.

[8] J. W. Cahn, J.E. Hilliard; *J. Chem. Phys.* 31, **1959**, 688.

[9] J. W. Cahn; *J. Chem. Phys.* 42, **1965**, 93.

[10] T. Yazawa, K. Kuraoka, W.D. Du; *J. Phys. Chem. B* 103, **1999**, 9841.

[11] P. Levitz, G. Ehret, S. K. Sinha, J. M. Drak; *J. Chem. Phys.*95, **1991**, 66151.

[12] J. Werner, K. Otto, D. Enke, G. Pelzl, F. Janowski, H. Kresse; *Liquid Cryst.* 27, **2000**, 1295.

[13] V. Reshetnyak, L. Shanski, O. Yaroshchuk, A. Tereshchenko, J. Lindau, G. Pelzl, F. Janowski, K. Otto; *Mol. Cryst. Liquid Cryst.* 329, **1999**, 447.

[14] K. Otto, F. Janowski, D. Enke, W. Heyer; Verfahren zur Herstellung von Ultradünnen Porösen Glasmembranen, DE 19848377 A1, **2000**.

[15] E. Hempel, S. Vieweg, A. Huwe, K. Otto, C. Schick, E. Donth; *J. Phys.*10, **2000**, Pr7/79 (Pr7, International Workshop on Dynamics in Confinement, **2000**).

[16] D. Enke, F. Friedel, F. Janowski, T. Hahn, W. Gille, R. Müller, H. Kaden; Characterisation of Porous Solids IV, Studies in Surface Science and Catalysis 144, Elsevier, Amsterdam, **2002**, 347.

[17] R. Neffati, J. Rault; *Eur. Phys. J. B* 21, **2001**, 205.

[18] K. Ciesielski, A. L. Dawidowisz, J. Goworek, B. Jasinska, J. Wawryszczuk; *Chem. Phys. Lett.* 289, **1998**, 41.

[19] J. Goworek, K. Ciesielski, B. Jasinska, J. Wawryszczuk: *Rad. Phys. And. Chem.* 58, **2000**, 719.

[20] B. Jasińska, A. L. Dawidowisz; *Mater. Sci. Forum* 363–365, **2001**, 371.

[21] T. Goworek, B. Jasińska, T. Suzuki. *Mater. Sci. Forum* 363–365, **2001**, 316.

[22] T. L. Dull, W. E. Frieze, and D. W. Gidley; *J. Phys. Chem. B* 105, **2001**, 4657.

[23] B. Jasińska, J. Wawryszczuk, R. Zaleski; *Acta Physica Polonica* A107, **2005**, 821.

[24] G. Walter, R. Kranold, U. Lembke; *J. Appl. Cryst.* 30, **1997**, 1048.

[25] A. F. Novikov; *Opt. Appl.* 30, **2000**, 569.

[26] S. Pikus, A. L. Dawidowicz, E. Kobylas, D. Wianowska; Proc. SPIE-Int. *Soc. Opt. Eng.*81, **2000**, 4240.

[27] S. Pikus, A. L. Dawidowicz, E. Kobylas, D. Wianowska; *Mater. Chem. Phys.* 70, **2001**, 181.

[28] D. Enke, K. Otto, F. Janowski, W. Heyer, W. Schwieger, W. Gille; *J. Mater. Sci.* 36, **2001**, 2349.

[29] D. Enke, F. Janowski, W. Gille, W. Schwieger; Colloids Surfaces A: *Physicochem Eng. Aspects* 187–188, **2001**, 131.

[30] W. Gille, D. Enke, F. Janowski; *J. Porous Mater.* 8, **2001**, 111.

[31] W. Gille, D. Enke, F. Janowski; *J. Porous Mater.* 8, **2001**, 179.

[32] E. S. Kikkinides, M. E. Kainourgiakis, K. L. Stefanopoulos, A.Ch. Mitropoulos, A. K. Stubos, N. K. Kanellopoulos; *J. Chem. Phys.* 112, **2000**, 9881.

[33] M. Hermann, U. Gottschalk; *Bioforum* 3, **2000**, 172.

[34] K. Beltsios, E. Soterakou, N. Kanellopoulus, G. Tsangaris; *Mater. Sci. Eng. C* 15, **2001**, 257.

[35] D. Heindl; *Lab.* 9, **1999**, 26.

[36] F. Janowski, D. Enke; in: Handbook of Porous Solids: F. Schüth, K.S.W. Sing, J. Weitkamp (Editors), Porous Glasses Volume 3, Wiley-VCH, Weinheim, **2002**, 1432.

[37] T. Takahashi, Y. Yanagimoto, T. Matsuoka, T. Kai; *Microporous Mater.* 6, **1996**, 189.

[38] T. Takahashi, S. Iwaishi, Y. Yanagimoto, T. Kai, Korean; *J. Chem. Eng.* 14, **1997**, 459.

[39] M. P. Xavier, B. Vallejo, M. D. Marazuela, M. C. Moreno-Bondi, F. Baldini, A. Falai, *Biosensors Bio electron.* 14, **2000**, 895.

[40] S. J. Greg, K. S. W. Sing; "Adsorption Surface Area and Porosity": 2nd Edition, Academic Press, London, **1991**.

[41] IUPAC Manual of Symbol and Terminology; *Pure Appl. Chem.* 31, **1972**, 578.

[42] S. Brunauer; "Characterisation of Porous Solids", Proc. Int. Symp. **1969** (eds. D. H. Everett and R. H. Ottewill), Butterworths, London, **1979**, p.90.

[43] M. M. Dubinin; "Characterisation of Porous Solids", Proc. Int. Symp. **1978** (eds. S. J. Gergg, K. S. W. Sing and H. F. Stoeckli); *Soc. Chem. Ind., London* **1979,** p.1.

[44] Brunauer, Emmet, Teller; *J. Amer. Chem. Soc.* 60, **1938**, 309.

[45] F. A. L. Dullien; "Fluid Transport and Pore Structure": 2nd Edition, Academic Press, San Diego, **1992**.

[46] E. J. Garboczi; "Mercury Porosimetry and Effective Networks for Permeability Calculations in Porous Materials"; *Powder Tech.* 67, **1991,** 121.

[47] J. Gowork; "Characterization of Silica-gel by Physical Methods": [in] Encyclopaedia of Colliods and Interfaces, Marcel-Dekker, **2003**, p.954.

[48] B. C. Lippens, B. G.Linsen., J. H. de Boer; *J. catalysis* 3, **1964,** 32.

[49] W. D. Harkins, G. Jura; J. Am. Chem. Soc.66, **1944**, 1366.

[50] E.W. Washburn; "A Method of Determining the Distribution of Pore Sizes in a Porous Material". *Nat. Acad. Sci.* 7, **1921**, 115.

Chapter-3:

[1] M. B. Prekal, W. B. Walters; *J. Chem.* 53, **1970**, 190.

[2] S. J. Tao; *Chem. Phys.* 56, **1972**, 5499.

[3] M. Eldrup, D. Lightbody, J. N. Sherwood; *Chem. Phys.* 63, **1981,** 51.

[4] A. P. Mills; *J. Phys. Rev. Lett.*46, **1981**, 717.

[5] H. Nakanishi, Y. Ujihira; *J. Phys.Chem.* **86**, **1982**, 4446.

[6] K. Venkateswaran, K. L. Cheng, Y. C. Jean; J. Phys. Chem. 89, **1985**, 3001.

[7] G. Dlubek, K. Saarinen, H. M. Fretwell; *J. Poly. Sci.* B 36, **1998**,1513. G. Dlubek, J. Stejny , M. A Alam; *Macromolecules* E 31, **1998**, 4574. G. Dlubek, C. Hübner, S. Eichler; *Physica Status Solidi* A172, **1999**, 303. G. Dlubek, T. Lupke, J. Stejny, M.A Alam, M. Arnold; *Macromol.* A 33, **2000,** 990. G. Dlubek, , F. Redmann, R. Krause-Rehberg; *J. Appl. Poly. Sci.* A 84, **2002**, 244. G. Dlubek, J. Stejny, T. Lüpke, D. Bamford, K. Petters , C. Hübner, M. A. Alam, M .J. Hill; *J. Poly. Sci.* B 40, **2002**, 65.

[8] B. Nagasaka, T. Eguchi, H. Nakamaya, N. Nakamaya, Y. Ito; *Radiat. Phys. Chem.* 58, **2000**, 709.

[9] Z. Gao, X. Yang, J. Cui, Y. Wang; *Zeolites* 11, **1991**, 607.

[10] I. Kenji, H. Nakanishi, and Y. Ujihira; *J. Phys. Chem.* B 103, **1999,** 4555.

[11] D. W. Gidley, W. E. Frieze, T. L. Dull, A. F.Yee, E. T. Ryan, H.-M. Ho; *Phys. Rev.* B 60, **1999**, R5157.

[12] D. W. Gidley, W. E. Frieze, T. L.Dull, A. F.Yee, C. V. Nguyen, D. Y. Yoon; *Appl. Phys. Lett.* 76, **2000**, 1282.

[13] D. W. Gidley, W. E. Frieze, T. L. Dull, J. Sun, A. F. Yee; *J. Phys. Chem.* B.105, **2001**, 4657.

[14] J.-N., Sun, W. E. Gidley, D. W. Dull, T. L. Frieze, A. F. Yee, C. V.Nguyen; R.Todd; *J. Appl. Phys.* 89, **2001**, 5138.

[15] B. Jasińska, A. E. Koziol, T. Goworek; *J. Radio. Nucl. Chem.* 210, **1996**, 617.

[16] T. Goworek, K. Ciesielski, B. Jasińska, J. Wawryszczuk; *Chem. Phys. Lett.* 272, **1997**, 91.

[17] T. Goworek, K. Ciesielski, B. Jasińska; J. Wawryszczuk; *Chem. Phys.* 230, **1998**, 305.

[18] T. Goworek, K. Ciesielski, B. Jasińska, J. Wawryszczuk; *Rad. Phys. Chem.*58, **2000**, 719.

[19] K. Ciesielski, K. A. L. Dawidowicz, T. Goworek, B. Jasińska, J. Wawryszczuk; *Chem. Phys. Lett.* 289, **1998**, 41.

[20] D. M. Schrader and Y. C. Jean; "Positron and Positronium Chemistry"; ed. Y. C. Jean, Elsevier, New York, **1988**.

[21] O. E. Mogensen; "Positron Annihilation in Chemistry": Springer-Verlag, Berlin, Heidelberg, **1995**.

[22] Y. C. Jean, P.E. Mallon, D. M. Schrader; " Principles and Applications of Positron and Positronium Chemistry"; ed. Y. C. Jean, World Scientific, Singapore, **2002**.

[23] Y. Io, T. Takano, M. Hasegwa; *Appl. Phys.* A 45, **1988**, 193.

[24] Y. Ito, T. Yamashina, M. Nagasaka; *Appl. Phys.* 6, **1975**, 323.

[25] S. Y. Chuang, S. J. Tao; *J. Chem. Phys.* 54, **1971**, 4904.

[26] F. H. Hsu, M. M. Yang, C. C. Yang; *Appl. Phys.* 15, **1978**, 85.

[27] W. Brandt, R. Paulin; *J. Phys. Rev. Lett.* 2, **1968** 193.

[28] K. Venkateswaran, K. L. Cheng, Y. C. Jean; *J. Phys. Chem.*88, **1984**, 2465.

Chapter-4:

[1] E. A. Lorch; Proc. of the 5th Int. conf. on Pos. Ann., (ed. R. Hastguta) 403 (Sendai, **1979**).

[2] E. Brown et al.; “Table of isotopes” (ed. C. M. Lederer and V. S. Shirley, eds.): Wiely New York, **1978,** pp.36, 170,196, 216.

[3] Emad A. Badawi; Ph.D thesis El-Minia University, Egypt, **1994**.

[4] A. Bohr, Ben R. Mottelson; *Nuclear Structure, volume 1*: World Scientific Publishing Co. Ltd **1998**.

[5] A. C. Nisbet; Characterisation and Lifetime Measurements with BaF_2 Detectors*;* Physics Dept., School of Electronics & Physical Sciences, University of Surrey **2006**.

[6] G. f. knoll; Radiation Detection and Measuremen*t*; 3 edition, John Wiley & Sons, Inc **2000**.

[7] Burcham and Jobes; "Nuclear and Particle Physics": Longman Group Limited, **1995**.

[8] W. Umrath; "Fundamentals of Vacuum Technology": Leybold Vacuum, **2000**.

Chapter-5:

[1] R. Krause-Rehberg, H. Leipner; "Positron Annihilation in Semiconductors": Springer-Verlag, Berlin **1999**.

[2] J. Kansey; Microcomputer Programme for Analysis of Positron Annihilation Lifetime Spectra: *Nucl. Instr. Meth.* A 374, **1996**, 235. J. Kansy, Katowice; Poland, **2002**.

[3] D. W.Gidley, W. E.Frieze, T. L.Dull, J. Sun, A. F.Yee; *J. Phys. Chem.* B.105, **2001**, 4657.

[4] S. Thraenert , E. M. Hassan, R. Krause-Rehberg; *Nucl. Instr. and Meth.* B 248, **2006**, 336.

[5] Routine calcRTE; V. Bondarenko, S. Tränert, E. M. Hassan; Institute of Physics, University of Halle, **2007**, unpublished.

[6] M. Eldrup, D. Lightbody, J. N. Sherwood; *Chem. Phys.* 63, **1981**, 51.

[7] Routine EELViS; R. Zaleski, Department of Nuclear Methods, Maria Curie-Sklodowska University, Lublin, Poland, June **2007**.

[8] K. Ciesielski, A. L. Dawidowicz, T. Goworek, B. Jasińka, J. Wawryszczuk; *Chem. Phys. Lett.* 289, **1998**, 41

[9] T. Goworek, K. Ciesielski, B. Jasińka, J. Wawryszczuk; *Rad. Phys. Chem.*58, **2000**, 719.

[10] K. S. W. Sing, D. H. Everett, R. A. W.Haul, L. Moscou, R. A. Pierotti, J. Rouquerol, T. Siemieniewska; *Pure Appl. Chem. 57*, **1985**, 603.

[11] C. G. V. Burgess, D. H. Everett, S. Nuttall; *Pure Appl. Chem. 61*, **1989**, 1845.

[12] P. I. Ravikovitch, S. C. O. Domhnail, A. V.Neimark, F. Schuth, K. K. Unger: *Langmui*r 11, **1995**, 4765.

[13] K. Morishige, M. Shikimi; *J. Chem. Phys*. 108, **1998**, 7821.

[14] C. G. Sonwane, S. K. Bhatia; *Langmuir 15*, **1999**, 5347.

[15] W. D. Machin; *Phys. Chem. Chem. Phys. 5*, **2003**, 203.

[16] N. J. Wilkinson, M. A. Alam, J. M. Clayton, R. Evans, H. M. Fretwell, S. G. Usmar; *Phys.Rev. Lett. 69*, **1992**, 3535. J. A. Duffy, N. J. Wilkinson, H. M. Fretwell, M. A. Alam; *J. Phys.*: *Condens. Matter. 7*, **1995**, L27. N. J. Wilkinson, J. A. Duffy, H. M. Fretwell, M. A. Alam; *Phys. Lett. A 204,* **1995**, 285. M. A. Alam, H. M. Fretwell, J. A. Duffy, A. P. Clarke, S. B.Dugdale; *J. Radioanal. Nucl. Chem. 210*, **1996**, 255. A. P.Clarke, M. A. Alam, H. M. Fretwell, J. A. Duffy; J. A. *J.Radioanal. Nucl. Chem. 211*, **1996**, 165. M. A. Alam, A. P. Clarke, and J. A. Duffy; *Langmuir 16*, **2000**, 7551. J. A. Duffy and M. A. Alam; *Langmuir* **2000,** *16,* 9513.

[17] G. J. Daniel and M. F. Helen; *Langmuir 19,* **2003,** 9018

[18] S. J. Toa; *Chem. Phys.* 56, **1972**, 5499.

[19] D. W. Gidley, K. A. Marko, A. Rich; *Phys. Rev. Lett.*36, **1972**, 395.

[20] H. Nakanishi, Y. Ujihira; *J. Phys.Chem.* 86, 1982, 4446.

[21] T. Goworek, K. Ciesielski, B. Jasińka, J. Wawryszczuk; *Chem. Phys.* 230, **1998**, 305.

[22] S. Lowell, J. E. Shields; "Powder Surface Area and Porosity": Springer-Verlag, Berlin, **1991**. S. Lowell, J. E. Shields, M. A. Thomas, M. Thommes; "Characterization of Porous Solids and Powders: Surface Area, Pore Size and Density": Springer-Verlag, Berlin, **2004**.

[23] A. J. Hurd, D. W. Schaefer, D. M. Smith and S. B. Ross, A. Le Méhauté, S. Spooner; *Phys. Rev.* B 39, **1989**, 9742. G. Walter, R. Kranold, D. Enke and G. Goerigk; *J. Appl. Cryst.* 36, **2003**. 592.

[24] J. D. F. Ramsay; *Pure and Appl. Chem.* 65, **1993**, 2169.

[25] S.-H. Suh, W.-Ki Min, J. M. D. MacElroy; *Bull. Korean Chem. Soc.* 20, **1999**, 1521.

a, b, c	side lengths of rectangular potential well
A_{sp}	specific surface area
b	fit parameter
c	velocity of light
CFD	constant fraction discriminator
CPG	control porous glass
d_L	the density of the liquid adsorbate
D	mean pore size
ΔE	Doppler shift
e^+	positron
e^-	electron
E	energy
E. C.	electron capture
E_{B}	binding energy of electron positron pair
E_{R}	the energy resolution of detector
E_{int}	the eeffecincy of detector
FWHM	full width half maximum
g_i	statistical weight of a level in Boltzmann distribution
γ	γ-quantum
$\hbar$	Planck's constant
I_i	intensity of component i (with lifetime τ_{i}) in the lifetime spectrum
IUPAC	international union of pure and applied chemistry
$J_l(\mathrm{r})$	spherical Bessel function
$J_m(\mathrm{r})$	cylindrical Bessel function
K	Boltzmann's constant
κ_{Ps}	positronium formation rate
$\lambda_{2\gamma}$	2 γ-quanta annihilation rate of Ps
$\lambda_{3\gamma}$	3 γ-quanta annihilation rate of Ps
λ	decay rate of component i
λ_{a}	annihilation rate in bulk material
$\lambda_{o\mathrm{Ps}}$	annihilation rate of *o*-Ps (triplet)
$\lambda_{p\mathrm{Ps}}$	annihilation rate of *p*-Ps (singlet)
λ_{vac}	annihilation rate of Ps in vacuum
MCA	multi-channel analyzer
m_{e}	electron mass (= positron mass)
M	the molecular weight
m^{s}	the mass of the adsorbent (solid)
μ	the degree of impenetrability factor
$\mathrm{N_A}$	Avogadro's number
n^{a}	the amount of gas adsorbed
nm	nanometers
ns	nanoseconds
ν	neutrino
Φ	component of wave function
ϕ	porosity of porous material
Ψ	wave function
P	the gas pressure
P_0	the saturation vapour pressure of gas
$P/P\mathrm{o}$	gas relative pressure
Ps	positronium atom

o-Ps	ortho-positronium
p-Ps	para-positronium
ps	picoseconds
PSD	pore size distribution
PVG	porous Vycor glass
p_x	x-component of the annihilation electron positron pair (parallel to detector axis)
p_z	z-component of the annihilation electron positron pair (perpendicular to detector axis)
r	radius (variable)
R	radius of potential well with infinite rectangular potentials
ΔR	broadening of the infinite potential well by an electron layer
R_0	$R_0 = R + \Delta R$
R_a	fit parameter in Tokyo model
TAC	time to amplitude converter
τ_i	average lifetime of component i in lifetime spectra
τ_{oPs}	average lifetime of o-Ps (triplet)
τ_{pPs}	average lifetime of p-Ps (singlet)
τ_{sci}	the decay time of the scintillator
$\Delta\theta$	angular deviation of the two coinciding signals from detector-detector axis
σ_n	cross-section area of a single nitrogen molecule
S	ratio of central area to total area of a Doppler broadened annihilation signal
s	magnetic spin
UHV	ultrahigh vacuum
UV	ultravoilet radiation
V_p	specific pore volume
V_a	the volume of gas adsorbed on one square centimetre of the surface at pressure P
V_m	the volume of gas adsorbed when the entire surface is covered with a complete monomolecular layer
x, y, z	directions of a, b, and c lengths
X_{nl}	nodes of the J_l Bessel functions in the spherical pore shape
X_{nm}	nodes of the J_m Bessel functions in the cylindrical pore shape
ζ	the reduced packing density

Pore Size D (nm)	Lifetime τ_4 (ns)	Powder	Membrane	Porosity ϕ (%)		Surface Area A_{sp} (m^2/g)	
				Powder	Membrane	Powder	Membrane
1		-------	-------	0.20		217	
1-2	21.07	-------		0.22		219	
2.2	27.41	-------					
2-3	32.04	-------		0.23		201	
3	46.87	-------		0.26		196	
4.5	65.85	-------		0.25		210	
5	68.42	-------		0.35		181	
6	80.04	-------					
8	91.27	-------		0.37	0.49	110	
10	102.9	-------	-------	0.51		109	220
13	108.94	-------		0.51		105	
16	113.20	-------		0.49	0.62	79	
20	118.94	-------	-------	0.51		69	107
25	120.12	-------		0.46		53	
30	124.5	-------		0.49		47	
34	128	-------		0.48		39	
50	130.2	-------		0.53	0.49	27	
56	131	-------	-------				
64	133.92	-------		0.55		26	
		-------					28

Acknowledgement of Statement

First and foremost, I express my honest gratitude to God (**Allah**) whose guidance and the power has given me believed, forth and patience to finish this work.

This work is a result of considerable amount of sustainable support, advice, assistance, guidance, and encouragement, without which it would not have seen the light of the day. I would like to extend my authentic gratefulness to the following individuals and institutions for their help with this project.

A great deep impassioned thank goes to ***Prof. Dr. Reinhard Krause-Rebherg*** for his supervision, support, enthusiasm, guidance, and reviewing this work. The institutional trust and freedom he gave me throughout the course of the research created comfortable and fruitful atmosphere for the work. Beside the regular discussions he held with me. His door was always open even when he had piles of work. We worked together with ease and enjoyment. Especially appreciated is the extra effort he put in to ensure work was progressing even during personal crises for both of us.

I wish to express my sincere gratitude to ***Prof. Dr. Günter Dlubek*** for his invaluable guidance, beneficial discussions, encouragement, constructive criticism, and careful review of the draft of this thesis. That are some of the many contributions that he has made during the course of this research even on the personal scale, he was always so close. I owe him a lot of my knowledge and experience.

I am deeply grateful to ***Dr. habil. D. Enke***, for his participating in suggestion the research program of this thesis, his preparation to the samples of my research, his helpful discussions, and his wonderful cooperation.

I would passionately like to show appreciation to the German Academic Exchange Service (***DAAD***) for the generous funding that made this research possible.

I would also like to extend my gratitude to ***Prof. Dr. Mamdouh A. Abedel Rahaman*** *and* ***Prof. Dr. Emad Badawi*** for their encouragement, moral support and devices.

This research was also benefited from discussions with fellow colleagues within the workgroup of positron annihilation at the Martin Luther University Halle-Wittenberg, they offered helpful cooperation; are to mention **Mr**. **Stefen Thränert**, **Mr. Mohamed El Sayed**, **Mr. Mario Penzler**, **Mr. Anrold Krille**, **Mr. Frank Süßkraut**, **Mr. Marco Jungmann**. As well, I would like to express my deepest thanks to the Physics administration and to the workstation at Friedmann Bach Platz 6 for their helpful and kind cooperation.

Finally, I would also like to express my genuine thanks to my family in Egypt for her moral support. They believe in me and stood always behind me encouraging and pushing forward to bring this work in its final form.

Declaration

I hereby, undertake that I have written the work independently and had not used forbidden learning aids or unquoted works and have indicated references. I have also acknowledged the contributions of all the scientists concerned.

Halle, 5.10.2007

´Sayd Ahmed`, Essmat